

**SYNTHESIS AND CHARACTERIZATION OF
MAGNETIC METAL OXIDE (Fe_3O_4 , Gd_2O_3)
NANOPARTICLES AND THEIR THERANOSTIC
APPLICATIONS**

VIVEKA KALIDASAN

(B.TECH., TAMILNADU AGRICULTURAL UNIVERSITY, INDIA

M.TECH., SASTRA UNIVERSITY, INDIA)

A THESIS SUBMITTED

FOR THE DEGREE OF DOCTOR OF PHILOSOPHY

DEPARTMENT OF MATERIALS SCIENCE AND ENGINEERING



2016

Declaration

I hereby declare that this thesis is my original work and it has been written by me in its entirety.

I have duly acknowledged all the sources of information which have been used in the thesis.

This thesis has also not been submitted for any degree in any university previously.

A handwritten signature in black ink, appearing to read 'K.V. Ka', written on a light-colored rectangular piece of paper.

Viveka Kalidasan
8/17/2016

Acknowledgements

Firstly, I would like to express my sincere gratitude to my supervisor Prof. Jun Ding of the Department of Materials Science and Engineering (MSE), National University of Singapore (NUS), for his guidance and encouragement throughout my PhD study. His immense patience, zeal, in-depth knowledge and motivating research ideas was a guiding light in my research career path and thesis.

I greatly appreciate the kind assistance from Dr. Xiaoli Liu, Dr. Yong Yang, Dr. Fang Jie and Dr. Aihong Liu at various stages of my research. I would also like to acknowledge all my past and current research group members: Dr. Tun Seng Herng, Dr. Weimin Li, Dr. Yang Yang, Dr. Erwin, Dr. Olga Chichvarina, Dr. Xiaoliang Hong, Dr. Yunbo Lv, Dr. Ming Zhen, Mr. Ragavendran Sundaram Nagarajan, Mr. Wen Xiao, Ms. Nina Bao, Ms. Xiangxia Wei, Mr. Shuai Chang, Mr. Zhe Chen, Mr. Jean Willy Habimana and Ms. Pon Janani Sugumaran,

A special mention and my sincere thanks to the lab officers of the Department of Materials Science and Engineering for their technical support in sample characterization; teaching assistants and administrative officers of the Department of Materials Science and Engineering for their support with official matters.

I would also extend my heartfelt gratitude to Dr. Sreedharan Sajikumar and his group from the Department of Physiology, NUS Yong Loo Lin School of Medicine for his collaboration and support.

I would like to thank my incredible friends who made Singapore my home away from home.

I cannot thank enough my husband, Mr. Hemanand Moorthy for being the wonderful man he is; for his immutable love and support for more than a decade now and the decades to come.

Every single moment of my life, forever is a gratitude by itself to my parents, Dr. Kalidasan Natarajan and Dr. Thilagavathy Balasubramaniam, for being the best parents; for letting us dream and perpetually supporting us to pursue the same and for all that they are to us that cannot be expressed and confined within the walls of any language; and my sister Ms. Adhvaidha Kalidasan for being my entirety and purpose of life.

List of Publications

Viveka Kalidasan, Xiao Li Liu, Aihong Liu, Yong Yang, Sreedharan Sajikumar, Jun Ding, “Effects of Physiological Components on Magnetic Hyperthermia: Insights into Ions and Heat Dissipation under radio-frequency AC magnetic field”, (2016 submitted).

Viveka Kalidasan, Jun Ding, “Globulin conjugated Fe_3O_4 nanoparticles for magnetic hyperthermia”, conference proceedings of ICBP2016 (World Scientific Publishing company)

Viveka Kalidasan, Xiao Li Liu, Ananya Dasgupta, Sreedharan Sajikumar, Jun Ding, “A combinatorial approach to enhance the biocompatibility and heating efficiency of magnetic hyperthermia- Serum Albumin conjugated ferrimagnetic magnetite nanoparticles”, MRS Advances, 1(3), 247-254, 2016.

Viveka Kalidasan, Xiao Li Liu, Tun Seng Herng, Yong Yang, Jun Ding, “Bovine Serum Albumin conjugated ferrimagnetic iron oxide nanoparticles to enhance the biocompatibility and magnetic hyperthermia performance”, Nano-Micro Letters, 8(1), 80-93, 2016.

Awards

2014: “International symposium on Functional Materials (ISFM) 2014, Singapore, “Best Poster Award”

Table of Contents

| | |
|--|------|
| Declaration | I |
| Acknowledgements | II |
| List of Publications | III |
| Table of Contents | IV |
| Summary | VII |
| List of Figures | XI |
| List of Tables | XVII |
| CHAPTER- 1: Introduction, Overview and Research Motivation..... | 1 |
| 1.1 Magnetic materials and their applications..... | 2 |
| 1.2 Biomedical applications of magnetic materials..... | 5 |
| 1.3 Magnetic Hyperthermia..... | 10 |
| 1.4 Magnetic Resonance Imaging..... | 21 |
| 1.5 Research Motivation..... | 26 |
| CHAPTER- 2: Synthesis, Phase Transfer and Characterization Techniques.. | 30 |
| 2.1 Synthesis of hydrophobic magnetic metal oxide nanoparticles..... | 31 |
| 2.1.1 Synthesis of Fe_3O_4 nanostructures..... | 35 |
| 2.1.2 Synthesis of Metal Fe_2O_4 (MFe_2O_4) nanoparticles..... | 38 |
| 2.1.3 Synthesis of ultra-small Gd_2O_3 nanoparticles..... | 38 |
| 2.2 Hydrophilic and biocompatible phase transfer of magnetic metal oxide nanoparticles..... | 39 |
| 2.2.1 Surfactant coating..... | 40 |
| 2.2.2 Ligand exchange reaction..... | 42 |
| 2.2.3 <i>In situ</i> polymerization reaction..... | 46 |
| 2.2.4 Biocompatible phase transfer..... | 47 |
| 2.3 Characterization techniques..... | 48 |
| 2.3.1 Transmission electron microscopy (TEM) and Selected Area Electron Diffraction (SAED) | 50 |
| 2.3.2 X-Ray diffraction (XRD) | 52 |
| 2.3.3 Vibrating sample magnetometer (VSM) | 53 |

| | |
|--|-----|
| 2.3.4 Superconducting Quantum Interface Device (SQUID)..... | 54 |
| 2.3.5 Fourier Transform Infrared Spectroscopy (FTIR)..... | 56 |
| 2.3.6 Dynamic light scattering (DLS) | 58 |
| 2.3.7 UV/Vis spectroscopy..... | 59 |
| 2.3.8 Confocal microscopy..... | 60 |
| 2.3.9 Flow cytometry..... | 61 |
| 2.3. 10 Heat Induction..... | 62 |
| 2.3.11 Magnetic Resonance Imaging (MRI) | 64 |
| CHAPTER- 3: Fe ₃ O ₄ Nanoparticles for Magnetic Hyperthermia Applications | 66 |
| 3.1 Introduction..... | 67 |
| 3.2 Method..... | 71 |
| 3.3 Results and Discussion..... | 75 |
| 3.3.1 Fe ₃ O ₄ nanoparticles of different sizes..... | 75 |
| 3.3.2 Fe ₃ O ₄ nanoparticles of different shapes..... | 84 |
| 3.3.3 Fe ₃ O ₄ nanoparticles of different composition- MetalFe ₂ O ₄ (CoFe ₂ O ₄ , NiFe ₂ O ₄) nanoparticles..... | 88 |
| 3.3.4 Combinatorial approach to enhance the biocompatibility and magnetic hyperthermia performance..... | 93 |
| 3.4 Conclusion..... | 105 |
| CHAPTER- 4: Effects of Physiological Components and AC Magnetic Field on Magnetic Hyperthermia..... | 108 |
| 4.1 Introduction..... | 109 |
| 4.2 Methods..... | 111 |
| 4.3 Results and Discussion..... | 114 |
| 4.4 Conclusion..... | 139 |
| CHAPTER 5: Gd ₂ O ₃ Nanoparticles as MRI contrast agents..... | 140 |
| 5.1 Introduction..... | 141 |
| 5.2 Methods..... | 143 |
| 5.3 Results and Discussion..... | 146 |
| 5.3.1 Comparison between thioglycolic acid and BSA conjugated Gd ₂ O ₃ Nanoparticles..... | 147 |
| 5.3.2 <i>In-situ</i> Photodegraded Poly Vinyl Pyrrolidone coated Gd ₂ O ₃ nanoparticles..... | 151 |

| | |
|--|-----|
| 5.4 Conclusion..... | 155 |
| CHAPTER 6: Fe ₃ O ₄ -Gd ₂ O ₃ Nanoclusters for Magnetic Hyperthermia and MRI Applications..... | 157 |
| 6.1 Introduction..... | 158 |
| 6.2 Methods..... | 161 |
| 6.3 Results and Discussion..... | 165 |
| 6.4 Conclusion..... | 173 |
| CHAPTER 7: Conclusions and Future works..... | 174 |
| 7.1 Conclusions..... | 175 |
| 7.2 Future works..... | 179 |
| References..... | 181 |

Summary

This thesis discusses the fabrication of magnetic metal oxide (Fe_3O_4 , Gd_2O_3) nanoparticles for theranostic applications, viz, Fe_3O_4 nanoparticles for cancer therapy as in magnetic hyperthermia and Fe_3O_4 , Gd_2O_3 nanoparticles for diagnostic applications as in magnetic resonance imaging (MRI). The other applications of magnetic metal oxide (Fe_3O_4 , Gd_2O_3) nanoparticles are beyond the scope of this thesis. This thesis also discusses the influence of physiological components like proteins and ions under the applied alternating current magnetic field, on the efficiency of magnetic hyperthermia.

- 1) Hydrophilic Fe_3O_4 nanoparticles of different size, shape, composition and surface modification were fabricated. Among the 10 nm superparamagnetic iron oxide nanoparticles (SPIONs) and 30 nm ferrimagnetic iron oxide nanoparticles (FIONs), FIONs have higher magnetic saturation and hence show higher SAR value irrespective of the surface modifying agent used. Different surface modifying agents were used to convert the as-synthesized oleic acid capped, hydrophobic Fe_3O_4 nanoparticles to hydrophilic phase. Among the surface modifying agents used, (3-Aminopropyl) trimethoxysilane (APTMS) capping showed better stability when compared to Cetyl Trimethyl Ammonium Bromide (CTAB) or Polyethyleneimine (PEI) coating. Hence APTMS was further used in our hydrophilic phase transfer experiments. Both 10 nm and 30 nm Fe_3O_4 nanoparticles show very high cell viability. We had fabricated hydrophilic

nanospheres, nanohexagons and nanotetragons of 20 nm size. Nanotetragons were found to show polydispersity and also exhibited high magnetic hyperthermia efficiency. Composition of the Fe_3O_4 nanoparticles were modified by doping with divalent ions like cobalt and nickel. CoFe_2O_4 nanoparticles of size 15 nm show higher coercivity and hence higher SAR value when compared to 15 nm Fe_3O_4 nanoparticles and 150 nm NiFe_2O_4 nanoparticles. Discussion about the manipulation of size, shape and composition of Fe_3O_4 nanoparticles gives preliminary insights into use of Fe_3O_4 nanoparticles for magnetic hyperthermia applications. Hydrophilic phase transfer improves the colloidal stability of magnetic metal oxide (Fe_3O_4 , Gd_2O_3) nanoparticles in de-ionised water. But improving the biocompatibility enhances the potential chance of the magnetic metal oxide (Fe_3O_4 , Gd_2O_3) nanoparticles for biomedical applications. Therefore we have discussed the fabrication of albumin conjugated 30 nm Fe_3O_4 nanoparticles. Fe_3O_4 nanoparticles of size 30 nm were chosen as the core magnetic material, for better magnetic properties, as discussed earlier. Bovine Serum Albumin (BSA) conjugation has found to enhance both the biocompatibility and the heating efficiency of the Fe_3O_4 nanoparticles. We have conjugated BSA over surface modified Fe_3O_4 nanoparticles by physical adsorption method using CTAB and covalent amide bond formation by APTMS. Albumin is the most abundant protein present in blood plasma and hence it offers better stealth characteristics. This is proved by haemolytic studies and cell viability studies using BHK cell lines for BSA conjugated 30 nm Fe_3O_4 nanoparticles. BSA conjugation also renders better stability and prevents

aggregation of Fe_3O_4 nanoparticles in water, thus enhancing the heating efficiency of 30 nm Fe_3O_4 nanoparticles. Thus we have proposed a single combinatorial approach for improved biocompatibility and enhanced magnetic hyperthermia performance.

- 2) Various physical and chemical parameters like size, shape, anisotropy, composition, applied magnetic field etc., influence the magnetic hyperthermia efficiency of magnetic nanoparticles. It is plausible that the physiology of any biosystem will also impact the efficiency of magnetic hyperthermia system since the odyssey of the injected magnetic nanoparticles involves passage through blood to tumor site. Thus we have attempted to explore the basic properties of Fe_3O_4 nanoparticles once inside a biosystem. Physiological components like ions and proteins have found to influence the performance of 10 nm Fe_3O_4 nanoparticles inside biosystem. While physiological ions enhance the heating efficiency of 10 nm Fe_3O_4 nanoparticles due to their motility, the physiological proteins and cells present in blood plasma, restrict the mobility of the ions, thereby retarding the heating efficiency of the 10 nm Fe_3O_4 nanoparticles. Thus acting as biosafety agents. Therefore the adverse effects of magnetic nanoparticles on a biosystem is under check. We have also found that AC magnetic field at therapeutic range does not cause damage to the tissue, thus confirming that magnetic hyperthermia effect is brought about by 10 nm Fe_3O_4 nanoparticles under the influence AC magnetic field. This study throws basic insights into the fundamentals of magnetic hyperthermia inside physiology.

3) Gd_2O_3 nanoparticles with various surface modifications to enhance the relaxivity and biocompatibility of the same were fabricated. Organic protein (albumin) conjugated Gd_2O_3 nanoparticles with very good biocompatibility and relaxivity were fabricated. We have also fabricated inorganic, *in-situ* photodegraded, short chain polyvinyl pyrrolidone (PVP) coated Gd_2O_3 nanoparticles. PVP coated Gd_2O_3 nanoparticles show excellent relaxivity in water and comparable biocompatibility with BSA conjugated Gd_2O_3 nanoparticles.

4) We have fabricated iron oxide-gadolinium oxide (Io-Go) nanoclusters which can be used as a multifunctional platform for cancer theranostics in magnetic hyperthermia for cancer therapy and dual mode MR image contrast agents. This gives the nanoclusters a theranostic potential. The Polydopamine (PDA) coated Io-Go nanoclusters show effective magnetic hyperthermia efficiency without compromising on the cell viability. It also shows significant tumor necrosis. Thus, making it a very good magnetic hyperthermia agent. The PDA coated Io-Go nanoclusters are also found to act as good T1 and T2 dual contrast agents for MRI applications.

List of Figures

Figure 1.1 Schematic overview of B as a function of H for various materials

Figure 1.2 Schematic overview of biomedical applications of magnetic nanomaterials

Figure 1.3 Schematic representation of magnetic hyperthermia. Magnetic nanoparticles accumulate in tumors, targeting the cancer cells. When exposed to an alternating magnetic field, the nanoparticles tend to align with the applied field absorbing energy. MNPs oscillation transform this electromagnetic energy into heat, increasing the temperature at this region

Figure 1.4 Magnetic coercivity (H_c) vs. particles size

Figure 1.5 A 2.5 nm particle showing surface spin disorder;

Figure 1.6 Illustration of Néel and Brownian relaxation of magnetic nanoparticles exposed in external magnetic field;

Figure 1.7 Schematic overview of the macroscopic magnetization vector generated by magnetic resonance excitation.

Figure 2.1 Schematic representation of thermal decomposition method.

Figure 2.2 Schematic representation of ferrofluid. The fluid consists of small magnetic particles dispersed in a liquid (left). Each particle consists of a single domain iron oxide core grafted with surfactant (right).

Figure 2.3 Schematic overview of CTAB coating over metal oxide (Fe_3O_4 , Gd_2O_3) nanoparticles.

Figure 2.4 Schematic overview of PEI coating over metal oxide (Fe_3O_4 , Gd_2O_3) nanoparticles.

Figure 2.5 Schematic overview of APTMS capping over metal oxide (Fe_3O_4 , Gd_2O_3) nanoparticles.

Figure 2.6 Schematic overview of TA capping over metal oxide (Fe_3O_4 , Gd_2O_3) nanoparticles.

Figure 2.7 Schematic overview of PVP capping over metal oxide (Fe_3O_4 , Gd_2O_3) nanoparticles.

Figure 2.8 Schematic overview of *in situ* polymerization of dopamine over metal oxide (Fe_3O_4 , Gd_2O_3) nanoparticles.

Figure 2.9 Schematic overview of albumin conjugation over metal oxide (Fe_3O_4 , Gd_2O_3) nanoparticles.

Figure 2.10 Schematic illustration of working principle of Transmission Electron Microscope.

Figure 2.11 Schematic illustration of working principle of X-Ray Diffractometer.

Figure 2.12 Schematic illustration of working principle of Vibrating Sample magnetometer.

Figure 2.13 Schematic illustration of working principle of Superconducting Quantum Interface Device.

Figure 2.14 Schematic illustration of principle of Fourier Transform Infrared Spectroscopy.

Figure 2.15 Schematic illustration of principle of Dynamic Light Scattering.

Figure 2.16 Schematic illustration of principle of UV-Visible Spectroscopy.

Figure 2.17 Schematic illustration of principle of confocal microscopy.

Figure 2.18 Schematic illustration of principle of Flow Cytometry.

Figure 2.19 Schematic illustration of Magnetic hyperthermia set-up.

Figure 2.20 Schematic illustration of principle of MRI.

Figure 3.1 Characterization of as-synthesized Fe_3O_4 nanoparticles (a-i) TEM image of 10 nm SPIONs (a-ii) TEM image of 30 nm FIONs (b-i) SAED pattern of Fe_3O_4 nanoparticles (b-ii) XRD plots of Fe_3O_4 nanoparticles (c-i) saturation magnetization (M_s) of Fe_3O_4 nanoparticles. Inset image shows the coercivity of 30 nm FIONs (c-ii) magnetization hysteresis loops of 30 nm FIONs at different temperatures (c-iii) Verwey transition temperature (T_v) of 30 nm FIONs.

Figure 3.2 Hydrophilic phase transfer of Fe_3O_4 nanoparticle (a-i) FTIR plot for CTAB coated Fe_3O_4 nanoparticles (a-ii) FTIR plot for APTMS capped Fe_3O_4 nanoparticles (a-iii) FTIR plot for PEI coated Fe_3O_4 nanoparticles (b-i) Average hydrodynamic radius of CTAB, APTMS and PEI coated 10 nm SPIONs (b-ii) Average hydrodynamic radius of CTAB, APTMS and PEI coated 30 nm FIONs. Inset shows the 30 nm FIONs individually coated with APTMS and the stable APTMS-FIONs solution (b-iii) stability of hydrophilic Fe_3O_4 nanoparticles over a period of 1 month.

Figure 3.3 Cell viability studies of Fe_3O_4 nanoparticles of different sizes a) 10 nm SPIONs- 99.4% viability b) 30 nm FIONs- 98% viability.

Figure 3.4 SAR value comparison between hydrophilic Fe_3O_4 nanoparticles. Inset image shows the temperature raise comparison between 10 nm and 30 nm Fe_3O_4 nanoparticles for 3 minutes at 600 Oe.

Figure 3.5 Characterization of as-synthesized 20 nm Fe_3O_4 nanoparticles of different shapes (a-i) TEM image of nanospheres (a-ii) TEM image of nanohexagons (a-iii) TEM image of nanotetragons (a-ii) TEM image of nanohexagons (b) saturation magnetization (M_s) of Fe_3O_4 nanoparticles of different shapes (b) XRD plots of 20 nm Fe_3O_4 nanoparticles.

Figure 3.6 Average hydrodynamic radius of Fe_3O_4 nanoparticles of different shapes.

Figure 3.7 SAR value of Fe_3O_4 nanoparticles of different shapes.

Figure 3.8 Characterization of as-synthesized Metal Fe_2O_4 nanoparticles of different compositions (a-i) TEM image of 15 nm Fe_3O_4 nanoparticles (a-ii) SAED pattern of Fe_3O_4 nanoparticles (b-i) TEM image of 15 nm CoFe_2O_4 nanoparticles (b-ii) SAED pattern of CoFe_2O_4 nanoparticles (c-i) TEM image of 150 nm NiFe_2O_4 nanoparticles (c-ii) SAED pattern of NiFe_2O_4 nanoparticles (b) saturation magnetization (M_s) of Metal Fe_2O_4 nanoparticles of different compositions.

Figure 3.9 Average hydrodynamic radius of hydrophilic Metal Fe_2O_4 nanoparticles of different compositions.

Figure 3.10 SAR value of MFe_2O_4 nanoparticles of different composition. Inset figure shows the temperature raise of the same.

Figure 3.11 Biocompatible Fe_3O_4 nanoparticles (a) UV-Visible spectrum of (i) CTAB- Fe_3O_4 nanoparticles (ii) APTMS- Fe_3O_4 nanoparticles (iii) characteristic peak of BSA at 280 nm (iv) blue-shift due to BSA-CTAB- Fe_3O_4 nanoparticles (v) blue-shift due to BSA-APTMS- Fe_3O_4 nanoparticles (b) Zeta potential comparison of hydrophilic and biocompatible Fe_3O_4 nanoparticles (c) Average hydrodynamic radius of BSA conjugated CTAB/APTMS coated SPIONs/FIONs. Inset shows the 30 nm FIONs individually conjugated with BSA and the stable BSA-APTMS-FIONs solution (d) stability of biocompatible Fe_3O_4 nanoparticles over a period of 1 month.

Figure 3.12 Haemolytic studies. Haemolytic effect of test samples (a) as-synthesized Fe_3O_4 nanoparticles (b) CTAB- Fe_3O_4 nanoparticles (c) BSA-CTAB- Fe_3O_4 nanoparticles (d) APTMS- Fe_3O_4 nanoparticles (e) BSA-APTMS- Fe_3O_4 nanoparticles (f) Mechanism of haemolysis (g) Haemolytic index of the BSA conjugated CTAB- Fe_3O_4 nanoparticles (h) Haemolytic index of the BSA conjugated CTAB- Fe_3O_4 nanoparticles.

Figure 3.13 Cell viability studies (a) The BSA conjugated APTMS-FIONs exhibit higher percentage of cell viability than the non-conjugated FIONs (b) APTMS-FIONs are 98 % viable (c) BSA-APTMS-FIONs are almost 99.5 %. Inset figures shows the confocal images of the same.

Figure 3.14 Heating characteristics a) Temperature raise comparison between BSA-CTAB-Fe₃O₄ nanoparticles and CTAB- Fe₃O₄ nanoparticles b) SAR value comparison between BSA-CTAB- Fe₃O₄ nanoparticles and CTAB- Fe₃O₄ nanoparticles c) Temperature raise comparison between BSA-APTMS- Fe₃O₄ nanoparticles and APTMS- Fe₃O₄ nanoparticles d) SAR value comparison between BSA-APTMS-Fe₃O₄ nanoparticles and APTMS- Fe₃O₄ nanoparticles.

Figure 3.15 Schematic overview of the BSA-FIONs to improve biocompatibility and heating efficiency.

Figure 3.16 Magnetic hyperthermia treatment on liver tissue (a) liver tissue before magnetic hyperthermia treatment (b) liver tissue after magnetic hyperthermia treatment with 0.1 mg/mL BSA-APTMS-FIONs and 600 Oe AC magnetic field to raise the temperature upto 45 °C.

Figure 4.1 (a) TEM image of the as-synthesized SPIONs. Inset image is the high resolution TEM micrograph showing lattice; (b) TEM selected area electron diffraction image (SAED) of the SPIONs (c) XRD plot (d) Magnetization of the SPIONs (e) Average hydrodynamic radius of SPIONs in water.

Figure 4.2 Time dependent temperature raise (ΔT) of 0.1mg/ SPIONs in water, 1xPBS and blood under 600 Oe at 360 kHz. Inset images are representational pictures of the samples.

Figure 4.3 Effect of concentration of PBS on temperature raise (ΔT). As the concentration of 1x PBS increases, ΔT increases, indicating that concentration of ions to ΔT .

Figure 4.4 Contribution of applied magnetic field towards temperature raise (ΔT) of 1x PBS

Figure 4.5 Temperature raise (after 3 minutes under 600 Oe at 360 kHz) of individual salts that constitute 1xPBS.

Figure 4.6 Contribution of individual ions (a) sodium salts (b) chloride salts to temperature raise (ΔT)

Figure 4.7 Contribution due to acids to temperature raise (ΔT). The temperature raise (ΔT) is proportional to the dissociation constant (k_a) of the acids.

Figure 4.8 Temperature raise in dependence of time for 1xPBS and 1xPBS with 50 mg/ML agarose under AC magnetic field of 600 Oe at 360 kHz.

Figure 4.9 Temperature raise due to physiological protein albumin (a) Temperature raise (ΔT) as a function of albumin concentration in 1xPBS under 600 Oe at 360 kHz for 3 minutes with and without SPIONs (b) Hyperthermia effect on cells suspended in 1xPBS without SPIONs under an

applied AC magnetic field–MCF-7 cells are alive as indicated by the green cells in the corresponding confocal image; Hyperthermia effect on cells suspended in 1xPBS with SPION under an applied AC magnetic field- MCF-7 cells are dead as indicated by the red nuclei in the corresponding confocal image.

Figure 4.10 Mechanism of action of physiological components towards magnetic hyperthermia. Salt solution comprising of cations (C^+) and anions (A^-) under an applied electric field move towards cathode and anode respectively increasing the temperature raise (ΔT). Whereas the addition of protein with surface charges due to cationic amino (NH_2^+) groups and anionic carboxyl (COO^-) groups trap A^- and C^+ respectively and retard their mobility thus decreasing the temperature raise (ΔT).

Figure 4.11 Impedance of (a) de-ionised water (b) 50 mg/mL albumin in de-ionised water (c) comparison between real parts of de-ionised water and 50 mg/mL albumin in de-ionised water (d) comparison between 0.1 M NaCl in de-ionised water and solution of 0.1 M NaCl-50 mg/mL albumin in de-ionised water.

Figure 4.12 Magnetic hyperthermia effect on liver tissue (a) Healthy liver tissue/tissue after exposure to AC magnetic field of 600 Oe without SPIONs has live cells (b) liver tissue after magnetic hyperthermia treatment under AC magnetic field and 0.1 mg/mL SPIONs causes tissue necrosis and apoptotic cells (c) Healthy kidney tissue/ tissue after application of AC magnetic field alone without SPIONs has live cells (d) liver tissue after magnetic hyperthermia treatment under AC magnetic field and 0.1 mg/mL SPIONs causes tissue necrosis as apoptotic cells.

Figure 4.13 Temperature effect on liver tissue (a) healthy liver tissue with live cells (b) temperature raise (ΔT) of upto 42°C causes apoptotic (c) temperature raise (ΔT) of upto 45°C causes complete necrosis.

Figure 5.1 As-synthesized hydrophobic, oleic acid capped Gd_2O_3 nanoparticles a) TEM image of Gd_2O_3 nanoparticles b) SAED pattern of Gd_2O_3 nanoparticles.

Figure 5.2 Average hydrodynamic radius of BSA conjugated Gd_2O_3 nanoparticles. Inset image shows the TEM image of BSA conjugated Gd_2O_3 nanoparticles.

Figure 5.3 Biocompatibility of BSA conjugated Gd_2O_3 nanoparticles a) Haemolytic study comparison between oleic acid (OA) capped, thioglycolic acid (TA) capped and BSA conjugated Gd_2O_3 nanoparticles. Inset image shows the haemolysed blood sample b) Cell viability of TA capped Gd_2O_3 nanoparticles- 98.4% c) Cell viability of BSA capped Gd_2O_3 nanoparticles- 99.6%.

Figure 5.4 Relaxivity measurements a) TA capped Gd_2O_3 nanoparticles b) BSA conjugated Gd_2O_3 nanoparticles.

Figure 5.5 Hydrophilic phase transfer of photodegraded PVP coated Gd_2O_3 nanoparticles a) FTIR plot of photodegraded PVP coated Gd_2O_3 nanoparticles b) average hydrodynamic radius of photodegraded PVP coated Gd_2O_3 nanoparticles.

Figure 5.6 Biocompatibility of photodegraded PVP coated Gd_2O_3 nanoparticles, showing cell viability of 99 % and haemolysis of 1.2%.

Figure 5.7 Relaxivity measurements of *in-situ* photodegraded PVP coated Gd_2O_3 nanoparticles.

Figure 6.1 Schematic overview of the PDA coated Io-Go nanoclusters as multifunctional platform for magnetic hyperthermia and MRI applications.

Figure 6.2 Characterization of as-synthesized Io-Go nanoclusters (a-i) TEM image of 20 nm Fe_3O_4 nanoparticles. Inset image is the SAED pattern (a-ii) TEM image of 3 nm Gd_2O_3 nanoparticles. Inset image is the SAED pattern (a-iii) TEM image of Io-Go nanoclusters. Inset image is the SAED pattern (b) saturation magnetization (M_s) of Io-Go nanoclusters. Inset image shows the coercivity of 20 nm Fe_3O_4 nanoparticles.

Figure 6.3 Hydrophilic phase transfer of Fe_3O_4 nanoparticle (a) TEM image of PDA coated Io-Go nanoclusters shows that the Gd_2O_3 nanoparticles are decorated over Fe_3O_4 nanoparticles and coated with PDA (b) SAED pattern of Io-Go nanoclusters (c) EDAX spectrum of Io-Go nanoclusters (d) Average hydrodynamic radius of PDA coated Io-Go nanoclusters (e) UV-Vis spectrum of PDA coated Io-Go nanoclusters.

Figure 6.4 Cell viability studies of (a) Io-Go nanoclusters-97 % (b) PDA coated Io-Go nanoclusters- 98 %.

Figure 6.5 Temperature raise comparison between PDA coated Fe_3O_4 nanoparticles and PDA coated Io-Go nanoclusters. Inset figure is the SAR value comparison of the same.

Figure 6.6 Magnetic hyperthermia treatment on SEM leukemia cell line using PDA coated Io-Go nanoclusters a) Cell line before treatment- 97.8% viability b) Cell line after treatment- 74% viability.

Figure 6.7 Plots of $1/T_1$ and $1/T_2$ as a function of Gd and Fe concentration. Inset images shows the the corresponding phantom images of Io-Go nanoclusters corresponding to Gd+Fe concentration in mM.

List of Tables

Table 2.1 Comparison between four of the most commonly used chemical synthesis methods

Table 2.2 Make and Model of instruments used in this thesis.

Table 4.1 Physiological concentration of physiological electrolytes as present in 1xPBS.

CHAPTER 1: Introduction, Overview and Research Motivation

1.1 Magnetic materials and their applications

Overview

Magnetism is the phenomenon by which some materials attract or repel other materials from a distance. Magnetic materials include iron, lodestone and some steels. Generally, magnetic forces are generated by moving charged particles which generate magnetic field [1]. When a magnetic material is placed in an external magnetic field, the atoms in the material possess an atomic moment. Magnetic dipoles exist in magnetic materials which can respond to the external magnetic field. Magnetic induction is given by the equation 1.1,

$$B = \mu_0 (H + M) \quad (1.1)$$

where μ_0 is the permeability of free space (its magnitude is 1.257×10^{-6} H/m); M is the magnetic moment m per unit volume of the material; H is magnetic field strength. Magnetic susceptibility is given by the equation 1.2,

$$M = \chi H \quad (1.2)$$

The magnetic response to external magnetic field results in materials being classified as diamagnetic, paramagnetic or ferromagnetic. Diamagnetism is when the response to external magnetic field is very weak and not permanent; it is due to the change in the orbital motion of electrons due to the external field, the direction of the induced magnetic moment is opposite to the field. In paramagnetism, because of incomplete cancellation of its electron magnetic

moments, each atom has a permanent dipole moment. When an external field is applied, the atomic dipoles align with the field. Diamagnetic and paramagnetic materials exhibit magnetization in the presence of an external field; They have low susceptibility implying that their magnetic induction is very weak. Ferromagnetism occurs, for example, in body centred cubic (b.c.c.) iron, cobalt, nickel, and in many alloy compositions based on Fe, Co and Ni. Ferromagnetic materials show permanent magnetic moments even in the absence of an external field. They have high susceptibility values up to 10^6 . The magnetic moments in such materials arise from atomic spin magnetic moments [2]. Fig. 1.1 gives a schematic overview of different categories of magnetic materials.

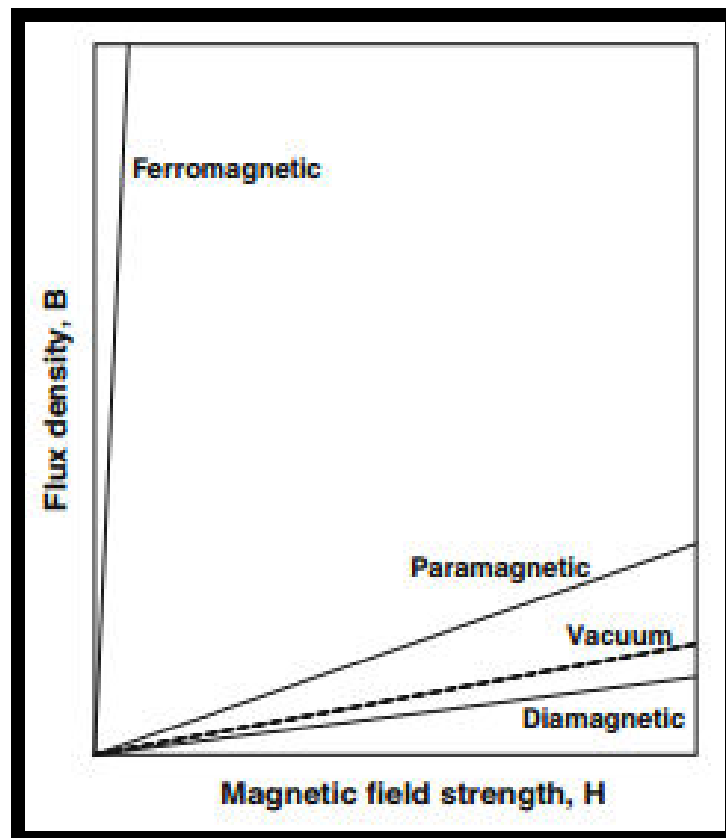


Fig. 1.1: Schematic overview of B as a function of H for various materials ^[1].

Based on B-H loop magnetic materials can be classified soft and hard magnetic materials. For hard magnetic materials, the area under the B-H loop is much larger than that of soft magnetic material with a large coercivity. Examples of magnetically soft materials are commercial iron ingot, oriented silicon-iron and Ferroxcube A (48% MnFe_2O_4 –52% ZnFe_2O_4) and that of hard are Cunife (60% Cu-20% Ni-20% Fe), sintered ferrite 3 (BaO -6 Fe_2O_3) [3].

Applications of magnetic materials

Magnetic materials find a myriad of applications in information storage, biomedicine [4] and magnetic energy storage [5]. Permanent magnets supply larger magnetic energy in even smaller volumes to be used in applications like transportation components, consumer products, clean energy technologies, military hardware and hybrid vehicle regenerative motors. Rare-earth “supermagnets,” made of iron, cobalt, and rare-earth elements such as Neodymium, Samarium etc., have accounted for the majority of high-energy product permanent magnets for hi-tech applications [6-8]. Magnetic materials are also used to improve the magnetic storage capacity of devices like magnetic tapes, and computer hard discs etc., [9]. Soft magnetic material widely used in motors, compressors and other rotating devices [10]. For inductor applications, powder magnetic material cores which give ease in manipulation of shape, size, winding etc., are being popularly used [11]. Magnetic nanoparticles form a very important class of magnetic materials.

Owing to their finite size, they have a high surface-to-volume ratio and different crystal structures. This gives magnetic nanoparticles their interesting magnetic properties when compared to their bulk counterparts [12]. Magnetic nanoparticles are used as giant magneto-resistance (GMR) sensors, Spintronic sensors, Spin Dependent Tunneling (SDT) sensors, etc., in order to detect and quantify labels [13]. Integrated magnetic/spintronic device microarrays have also shown to have a great potential in both biomedical research and practices [14]. Magnetic nanoparticles find their major application as contrast agents for imaging, cell separation, site-specific drug delivery agents, cancer therapeutics, water treatment etc., [15-17].

1.2 Biomedical applications of magnetic materials

This section focuses in-depth about the biomedical applications, as they are the prime focus of this thesis. The common biomedical applications of various magnetic materials especially magnetic metal oxide (Fe_3O_4 , Gd_2O_3) nanoparticles giving more emphasis on cancer theranostics is discussed. Though magnetic hyperthermia and magnetic resonance imaging (MRI) are discussed in this section, they are described more detailed in the subsequent sections. The earliest known biomedical use of naturally occurring magnetic materials is the use of magnetite (Fe_3O_4) or lodestone by the Indian surgeon Sushruta around 2,600 years ago. Current areas in medicine to which magnetite can be used include molecular and cell biology, cardiology, neurosurgery, oncology and radiology. Magnetic nanoparticles for biomedical applications should meet special criteria with respect to size, dispersity,

surface charge, biodegradability and specificity. To meet out these criteria, many pathways have been developed to synthesize magnetic nanoparticles and manipulate their functionalities through surface functionalization, coating and encapsulation strategies [18, 19]. Fig. 1.2 gives a overview of the various biomedical applications of magnetic nanomaterials.

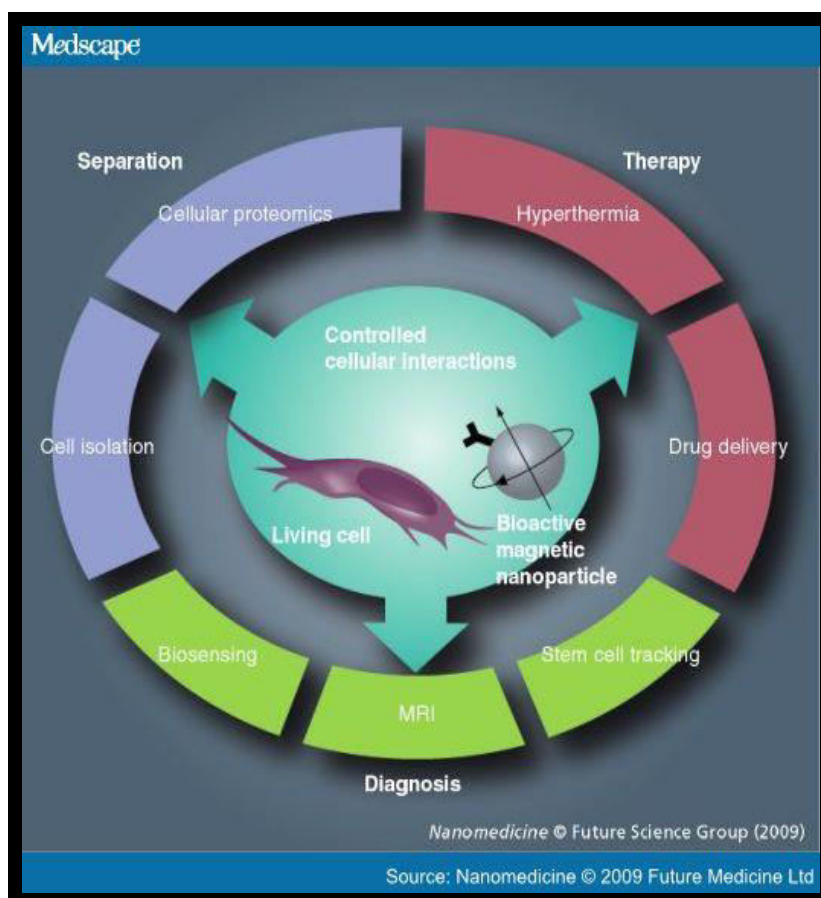


Fig. 1.2: Schematic overview of biomedical applications of magnetic nanomaterials^[19].

Magnetic Separation

Magnetic particles can be used to separate entities from their surroundings so as to purify or concentrate the surrounding entities [20]. This application is based on the difference in the susceptibility between the magnetically labelled entity and the surrounding medium. Examples of the use of this principle are magnetic cell sorting for cellular therapy and immunoassay. The first step is to label the entities like bacteria or cellular vesicles with the particles followed by the separation of the labelled entities by magnetic separation.

Drug and Gene Delivery

Most chemotherapy methods are relatively non-specific and hence are “wasted” by being distributed to areas where they are not required, leading to undesirable side effects. Drug delivery vehicles can carry the drugs to the target site and can also be fine-tuned to control the release of the drug. Much of the work which has been performed so far relates to targeting cancerous tumors. The optimum size of drug delivery vehicles is 5–100 nm size range. Typically, magnetite particle, or noble metals such as gold and silver is used for this application. Surface modified magnetic particles can be further manipulated and functionalized by attaching moieties like carboxyl groups, biotin, *etc.* [21, 22] which serve to couple various therapeutic drugs or target antibodies to the surface modified magnetic particles complex. Later these magnetic carriers are used to target specific sites or organs in the body for tumour therapy or gene

delivery [23, 24]. Radionuclides (e.g., β -emitters, β is the symbol used to denote an electron) can also be attached to the magnetic particles to be used as targeting agents. Since the radionuclide does not have to be released in the same way as the drug, control drug release is absent [25]. This technique is also called magnetofection, as it involves the use of magnetic particles to increase the efficiency of gene transfection (introduction of foreign DNA into a host cell) and expression [26]. The gene is carried inside a viral vector coated on the surface of the magnetic particle. This particle can then be held at the target area by applying a magnetic field. The virus is thus in contact with the tissue for increased duration which improves the transfection efficiency.

Artificial Muscle

Hydrogels, which are cross-linked polymer networks swollen with water, can be used to make soft actuators. Since most gels are relatively homogenous materials which shrink or swell uniformly, there is a need to improve the response of gels. Hence, magnetic field sensitive gels where magnetic particles of colloidal size are dispersed and incorporated into the gels are developed. These ferrogels combine the magnetic properties of magnetic fillers and the elastic properties of hydrogel. Iron oxide particles fused Polyvinyl alcohol (PVA) gel has been used for this application because of its mechanical

Hyperthermia

The idea that a localized raise in temperature of upto 42-45°C can be used to selectively destroy malignant tumor cells by magnetic particles which can be heated by an applied alternating current magnetic field.

Image Contrast Agents

So far, we have only considered magnetic properties associated with the electrons in the material. However, protons also have a magnetic moment, and this can be utilized in the powerful imaging technique of magnetic resonance imaging (MRI).

Cancer theranostics

The motivation of our thesis is primarily focused on magnetic materials for cancer theranostics. Iron oxide nanoparticle-based cancer therapy represents an important alternative to conventional chemotherapy, radiation, or surgery. Iron oxide (Fe_3O_4) nanoparticles are composed of 3 integral parts- iron core, a polymer coating, and functional moieties [28]. In spite of the extensive researches in nanomedicine, there are still unmet medical demands in cancer diagnosis and therapy. Advanced multimodal imaging facilitates the early stage diagnosis and real-time monitoring of diseases, especially cancer [29]. Nanomedicine for cancer treatment however, will have the greatest impact on

society when administered in combination with traditional therapies. Combination chemotherapy is a primary cancer treatment regimen to reduce cancer drug resistance [30]. Cancer theranostic approaches in pancreatic and brain cancers, increase the use of magnetic nanoparticles due to difficulty in positioning the tumor near sensitive organs, delivering treatment to the targeted organs and also extensive adverse reactions to conventional treatments techniques [31].

1.3 Magnetic Hyperthermia

Magnetic hyperthermia uses magnetic nanoparticles as heat sources [32] to raise the tissue temperature to ~42-46 °C. At this temperature, tumour cells are known to be more sensitive to heat than healthy cells [33]. Magnetic hyperthermia has synergistic effects when combined with other conventional treatment strategies like chemotherapy or radiotherapy. Low oxygen and nutrients concentration coupled with low pH make tumor cells more heat sensitive. Extensive research has been done to fabricate magnetic nanomaterials used for magnetic hyperthermia, manipulate the alternating current magnetic field strengths, alternating field frequencies and exposure times, etc., [34]. The successful clinical trials demonstrated the feasibility of this technique. Among the first clinical studies of magnetic hyperthermia is the treatment of brain tumours like glioblastoma multiforme through a combination of radiotherapy and magnetic hyperthermia. Here, magnetic resonance imaging was used in choosing the injection site and CT imaging was used in the follow up [35]. More complete evaluation of the clinical

outcomes is to be assessed with a larger group of patients and with different types of cancer [36, 37]. The prospect of combining magnetic hyperthermia with drug delivery is also next potential step in this field. Fig. 1.3 gives an overview of magnetic hyperthermia strategy.

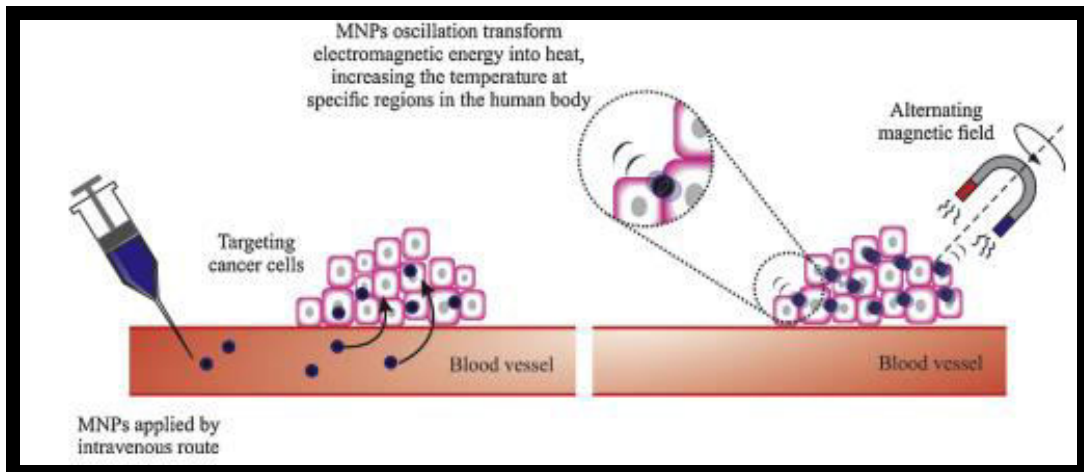


Fig. 1.3: Schematic representation of magnetic hyperthermia. Magnetic nanoparticles accumulate in tumors, targeting the cancer cells. When exposed to an alternating magnetic field, the nanoparticles tend to align with the applied field absorbing energy. MNPs oscillation transform this electromagnetic energy into heat, increasing the temperature at this region^[28]

Basel et al. have synthesized superparamagnetic iron/iron oxide nanoparticles and injected the same into RAW264.7 cells (mouse monocyte/macrophage-like cells). It was observed from the results that these nanoparticles selectively infiltrate pancreatic tumors when injected intraperitoneally without affecting healthy tissue [38]. Huang et al used magnetic nanoparticle in a subcutaneous squamous cell carcinoma mouse model. At a well-tolerated intravenous dose of 1.9 mg Fe/g tumor and application of an external magnetic field, tumors were heated to 60 °C in 2 min suffering ablation [39]. Peptide coated magnetic nanoparticles like aminosilane coated iron oxide nanoparticles was reported by Tsiapa et al [40] A high specificity, targeting glioblastoma tumors was observed.

All these reports throw a positive light on the potential application of suggest that this hyperthermia system using magnetic nanoparticles can cause tumor specific heating

Iron Oxide (Fe_3O_4) Nanoparticles

In recent years magnetic metal oxide nanoparticles have attracted considerable attention due to the ease and rapid progress in fabrication and processing. Among them, Fe_3O_4 nanoparticles are widely used in magnetic hyperthermia applications. Their magnetic properties are highly influenced by the variations in size, shape, composition and surface modification [41, 42]. Domain evolution is a very important criterion with regards to size and shape. Below a critical size, the Fe_3O_4 nanoparticles become single domain. Decrease in the size below 10 nm results in superparamagnetism with exciting magnetic properties. Fe_3O_4 nanoparticles of size 30-50 nm have higher magnetic saturation and are ferrimagnetic in nature [43, 44]. Similarly, shape also plays an important role in the determination of domain structure. In order to minimize energy, different shapes have distinct magnetic domain structures, which leads to significant change in both static and dynamic magnetic behaviors. Thus Fe_3O_4 nanoparticles of different shapes and sizes are find a plethora of applications especially in biomedicine [45, 46]. Increasing the magnetic anisotropy by partially replacing the ferrous ions by more anisotropic divalent ions like cobalt and nickel enhances the magnetic properties of the Fe_3O_4 nanoparticles, even at superparamagnetic size regime

[47, 48]. To further improve the biological application, Fe_3O_4 nanoparticles have to be made hydrophilic and biocompatible. Therefore, the surface modified size, shape, composition dependent magnetic properties of Fe_3O_4 nanoparticles are of great interest in biomedical field.

As mentioned earlier, the size, shape and composition are crucial for both the static and dynamic behaviors of Fe_3O_4 nanoparticles. Fig. 1.4 illustrates the evolution of magnetic domain and size dependent coercivity (H_c). As shown in the figure, when the particles size is above single domain critical size (D_c), multi-domain (MD) prevails.

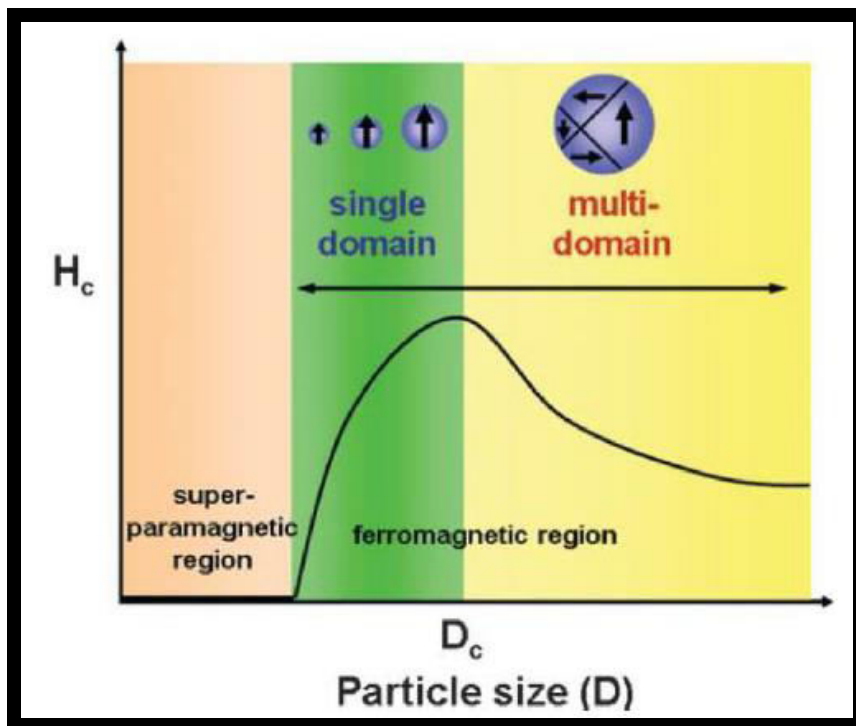


Fig. 1.4: Magnetic coercivity (H_c) vs. particles size ^[49].

Because of the small size of super paramagnetic iron oxide nanoparticles, large fractions of the total atoms in a super paramagnetic iron oxide nanoparticles are surface atoms [50]. As the particle size decreases, coercivity increases and reaches a maximum at D_c , thus aligning all the spins in nanoparticles parallel. Further decrease in particle size results in drop of the H_c due to superparamagnetism phenomenon. This phenomenon prevails when the measurement time is much larger than the Neel relaxation time given by equation 1.3,

$$\tau_N = \tau_0 \exp \frac{KV}{K_B T} \quad (1.3)$$

where, τ_0 - a relaxation time ($\sim 10^{-9}$ s); K_B - Boltzmann constant; T- temperature; K-the anisotropy constant; V-volume of nanoparticle, respectively.

It can be seen from the equation that τ_N decreases with the decreasing size. Superparamagnetism is the unique property of ultrasmall magnetic metal oxide nanoparticles. It is extremely useful for biomedical application. The size of superparamagnetic metal oxide nanoparticle is so small that agglomeration due to gravitation forces can be avoided [51] and also the weak interaction is advantageous for the stability of the magnetic fluid [52, 53]. Due these advantages, superparamagnetic nanoparticle are commonly employed for the ferrofluids and biomedical applications. Superparamagnetic metal oxide nanoparticles suffer from surface effect due to high surface to volume ratio, resulting in decrease of M_s because of serious surface spin disorder [54]. So

far, there are many reasons responsible for the spin disorder at the surface of magnetic metal oxide nanoparticles. One of the reasons is the broken exchange bonds between surface spins and reduced coordination, as shown in Fig. 1.5.

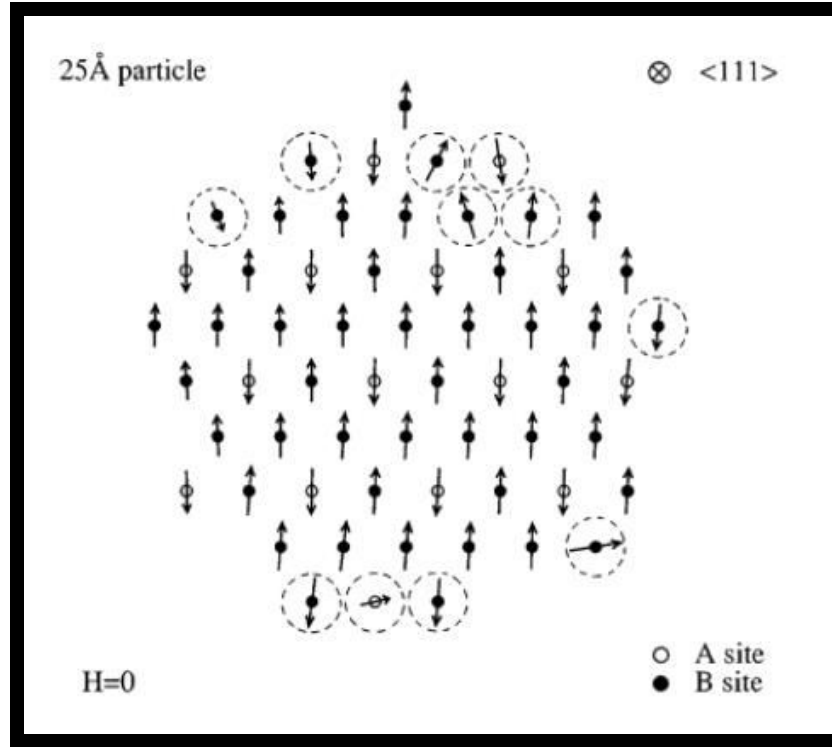


Fig. 1.5: A 2.5 nm particle showing surface spin disorder ^[55].

The effective anisotropy (K_{eff}) of a spherical nanoparticle is the sum of the surface anisotropy (K_v) and volume anisotropy (K_s), given by the equation 1.4,

$$K_{\text{eff}} = K_v + 6 K_s / d \quad (1.4)$$

where, d -the diameter of the particles [56]. The contribution of surface anisotropy is negligible for large particles.

Our thesis also discusses the use of ferrimagnetic Fe_3O_4 nanoparticles for enhanced heating efficiency for magnetic hyperthermia. Ferrimagnetic Fe_3O_4 nanoparticles have different atoms residing on different lattice sites with antiparallel magnetic moments but still their magnetic moments do not cancel out as they are of different magnitudes resulting in a net spontaneous magnetic moment. Despite wide research on the magnetic properties of these ferrimagnetic Fe_3O_4 nanoparticles, their magnetic behavior is not well established [57-59]. Studies suggest the occurrence of surface structure defects on ferrimagnetic Fe_3O_4 nanoparticles leading to magnetic disorder extending into the core of a given thickness. As discussed by Kodama *et al*, the exchange coupling between the core and surface gives rise to a variety of spin distributions within the ferrimagnetic Fe_3O_4 nanoparticles [60, 61].

Magnetic hyperthermia Mechanism

Relaxation loss and hysteresis loss, are the two main mechanisms responsible for the heat dissipation of superparamagnetic Fe_3O_4 nanoparticles subjected to the applied alternating current magnetic field. The Brownian relaxation is the rotation of nanoparticle due to the torque under applied alternating current magnetic field, while the Neel relaxation is the rotation of magnetic moment, while the nanoparticle is stationary as illustrated in Fig. 1.6.

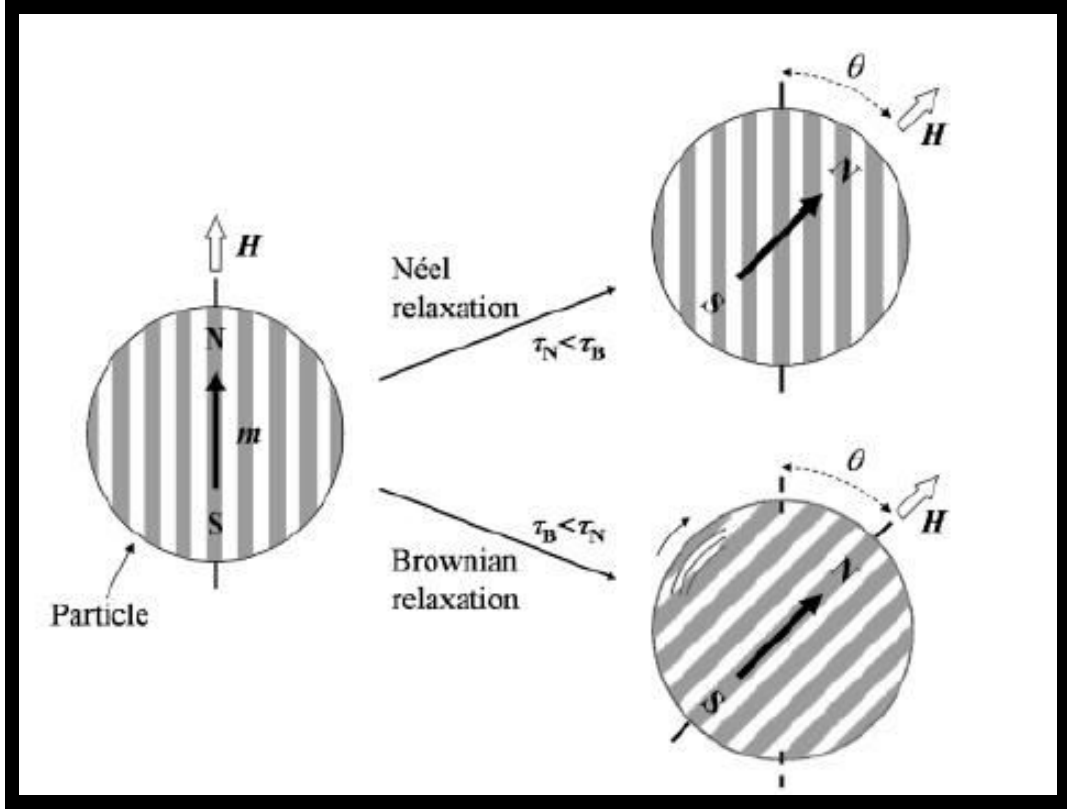


Fig. 1.6: Illustration of Néel and Brownian relaxation of magnetic nanoparticles exposed in external magnetic field ^[62].

The Néel and Brownian magnetic relaxation times of a particle are given by the following equations 1.5, 1.6, 1.7,

$$\tau_B = 3\eta V_h / KT \quad (1.5)$$

$$\tau_N = \tau_0 \exp KV_m / K_B T \quad (1.6)$$

$$\tau = \tau_B \tau_N / \tau_B + \tau_N \quad (1.7)$$

Where, τ_N is the Néel relaxation time; τ_B is the Brown relaxation time; τ is the effective relaxation time; τ_0 is about 10^{-9} s; K is the magnetic anisotropy constant; V_h is the Hydrodynamic volume of nanoparticle (the volume of a hypothetical hard sphere that diffuses in the same fashion as that of the particle

being measured); V_m is the nanoparticle volume, K_B is the Boltzmann constant; T is the temperature, η is the viscosity of the base liquid (water 8.94×10^{-4} Pas). Specific absorption rate (SAR) estimates the heating performance of the thermal seed given by the equation 1.8,

$$\text{SAR} = P/\rho \quad (1.8)$$

It should be noted that the Brownian-Néel relaxation loss is the main resource of heat generation in the superparamagnetic regime. When the size of magnetic nanoparticle is increased into the ferrimagnetic or ferromagnetic regime, hysteresis loss dominates relaxation loss. The hysteresis loss originates from the hysteresis behavior of ferrimagnetic or ferromagnetic magnetic Fe_3O_4 nanoparticles when exposed to a time varying magnetic field. The amount of heat generated per volume is given by equation 1.9,

$$P = \mu_0 f \oint H dM \quad (1.9)$$

The calculation of the hysteresis loss is more complicated when compared to the relaxation loss. Different methods are applicable in different particle size regimes. For instance, a linear response theory is valid for the superparamagnetic Fe_3O_4 nanoparticles [63]. Whereas for the coherent rotation of ferri or ferromagnetic Fe_3O_4 nanoparticles, the Stoner–Wohlfarth model based theories are applicable [64]. Also numerical methods were also developed to calculate the hysteresis loss for the single domain nanoparticles

[65]. However, the theoretical methods mentioned are suitable only for the single domain particles. After knowing the mechanisms of magnetic hyperthermia, a lot of work has been devoted for optimization of the heating seed to achieve the maximum heat dissipation ability/ SAR value.

Generally, the optimization was mainly focused on three aspects, namely size, shapes, compositions and surface modification to prevent agglomeration. Hergt proposed that maximum heat generation is expected by Fe_3O_4 particle suspensions with narrow size distribution with a mean diameter corresponding to the maximum coercivity in the single domain [66]. The sizes under study are 10 nm superparamagnetic Fe_3O_4 nanoparticles and 30 nm Fe_3O_4 nanoparticles. Vallejo-Fernandez et al. pointed out that a slight change in shape distribution would result in significant change in hysteresis loss for the hyperthermia system where the shape anisotropy dominates [67]. Ma et al. reported that the magnetite nanoplates exhibited high SAR values [68]. Cubic nanoparticles are demonstrated to exhibit higher power absorption values than the spherical [69]. Different shapes with varying anisotropy like, nanospheres, nanocubes, nanotetragons, nanohexagons, nanooctahedron etc., were synthesized. Since composition also determines the M_s and K values, which influence the hyperthermia performance, CoFe_2O_4 and NiFe_2O_4 nanoparticles with high magnetization superior to the ferrite were intensively studied as heating seeds for hyperthermia [70, 71]. Preventing agglomeration also significantly increases the SAR value, thus different surface modifying strategies are also discussed in this thesis [72]. Surface modification also render hydrophilicity and biocompatibility [73]. It can be known from above

discussions that magnetic hyperthermia is very sensitive to parameters of the heating seed, such as size and size distribution, shape and shape distribution, and composition and surface modification.

Just as any treatment strategy influences and affects the bio-system, the bio-system also unequivocally affects the efficiency of the treatment strategy. Our paper attempts to study the influence of biological system over the heating efficiency of a good magnetic hyperthermia system. Blood is the first and foremost influential biological parameter that would possibly influence the heating efficiency since Fe_3O_4 nanoparticles are injected into the blood stream. Blood flow plays a significant role in determining the heat dissipation in normal and tumor vasculature. The total volume of blood flowing in a tumor region is limited when compared to that in normal region. Therefore the heat dissipated by blood flow in tumor site is slower, which implies that the temperature raise in the tumor region is actually higher [74, 75]. Though it might seem to be a positive factor for magnetic hyperthermia system, it is actually not achieved everytime as the relative perfusion of blood in tumor site remains greater than that in the healthy tissue [76, 77]. Thermotolerance is an unavoidable side effect of any hyperthermia therapy as a resistance to heat is subsequently developed by the tumor cells [78, 79]. This could be seen as a factor that would influence the efficiency of the magnetic hyperthermia system. Surpassing all this, the odyssey of the injected Fe_3O_4 nanoparticles into the blood stream towards the tumor site, places a very important role. The injected Fe_3O_4 nanoparticles are dispersed into the blood stream and only a

tiny fraction of the same reaches the actual tumor site, of which an even lesser fraction diffuses into the tumor cells [80, 81].

The irregular angiogenesis in the tumor site also further mitigates the destiny of the Fe_3O_4 nanoparticles into the tumor region [82]. Thus if the Fe_3O_4 nanoparticles should have to encounter so many obstacles before reaching the targeted tumor site, the efficiency of a Fe_3O_4 nanoparticles based magnetic hyperthermia system is definitely subjected to a plethora of factors that tend to influence the results obtained in a lab.

1.4 Magnetic Resonance Imaging

Magnetic metal oxide nanoparticle made of the elements iron (Fe), gadolinium (Gd) or manganese (Mn) are widely used in many diagnostic applications performed under magnetic resonance imaging (MRI). MRI scanners reconstruct images from the electromagnetic signals generated by the stimulation, and relaxation, of the large pool of hydrogen (^1H) protons found in biological tissues. By atomic and molecular level interactions, magnetic metal oxide (Fe_3O_4 , Gd_2O_3) nanoparticles influence the relaxation time of hydrogen protons contained in small molecules like water. Thereby, magnetic metal oxide (Fe_3O_4 , Gd_2O_3) nanoparticles induce contrast enhancement effects on the reconstructed MR images. MRI is the most reliable, high resolution (75 – 300 μs), and multifunction imaging modalities of modern medicine. It allows the acquisition of in-depth, whole-body images, from the mouse model

to the humans when compared to optical imaging and echography. Unlike compute tomography

(CT), it does not rely on ionizing radiation. Moreover MRI also enables the tracking of cells, molecules, and drug delivery vehicles inside the biosystem. MRI has a relatively poor sensitivity compared to the other techniques. To fully exploit the potency of MRI in molecular and cellular imaging applications, it is necessary to design contrast agents which have the capacity to very efficiently interact with hydrogen protons. Most clinically approved contrast agents are based on small molecules that sequester the paramagnetic Gd^{3+} [83, 84]. Gadolinium has 7 unpaired electrons in the 4f orbital giving it a very large magnetic moment, a relatively slow electronic relaxation rate and enhanced proton relaxation properties [85]. Fe_3O_4 nanoparticles can also be used as MRI contrast agents. The strength of the magnetic field in common MRI scanners range from 1 to 3 Tesla. When a patient is introduced in the gantry of MRI machine, 1H in the body align their spins along the direction of the magnetic field (B_0), as shown in Fig. 1.7 (a). The sum the magnetic moments of these spins represent the “macroscopic magnetization vector” of biological tissue. This vector orients along the main magnetic field of the scanner. In their initial state, the spins “precess” at a certain frequency called Larmor frequency and are not coherent in phase. Later a radiofrequency (RF) wave tuned at Larmor conditions using a transmitter coil, is applied to the biological tissue. This causes the excitation of 1H spins causing spins lose their preferential orientation along the main magnetic field (Fig. 1.7 (b)). At this moment, the oscillation motion along the x-y plane is detected by a receiver

coil and is recorded. This represents the “MRI signal”. Then, the “x-y” phase coherence (M_{xy}) is gradually lost as neighboring ^1H protons exert a mutual influence on each other

as shown in Fig. 1.7 (c). As shown in Fig. 1.7(d), the time constant that quantifies this loss of phase coherence is the transversal relaxation time (T_2). As shown in Fig. 1.7(c), the excited spins gradually release their energy and recover their initial orientation along the main magnetic field of the scanner (M_z recovery). This return to the initial macroscopic magnetization state occurs within longitudinal relaxation time, T_1 as represented by Fig. 1.7(d). It is to be noted that T_1 and T_2 are intrinsic properties of any biological tissue.

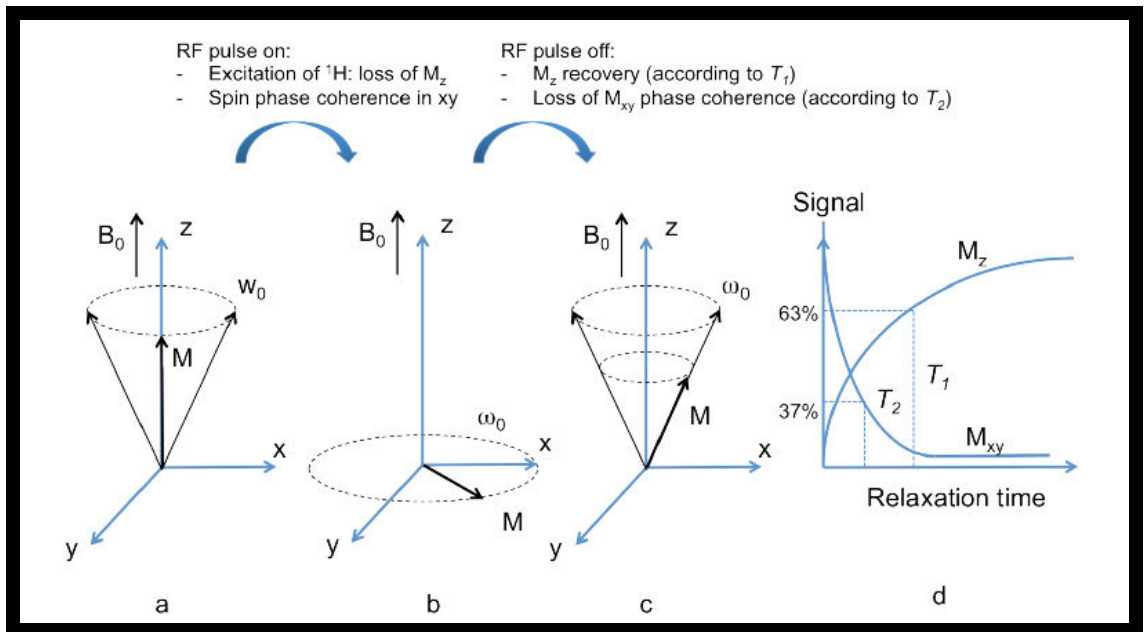


Fig. 1.7: Schematic overview of the macroscopic magnetization vector generated by magnetic resonance excitation ^[85].

The signal recorded for a given tissue (S), using a basic spin-echo sequence, is given by equation 1.10,

$$S = \rho(1 - e^{(-TR/T_1)}) (e^{-TE/T_2}) \quad (1.10)$$

Where, TR and TE are the repetition and the echo times (parameters in the spin-echo sequence [86]. The impact of contrast agents on the relaxation rate of protons, measured in constant conditions of magnetic strength and temperature, is given by the equation 1.11,

$$R_i = 1/T_i = 1/T_{i0} + r_i C \quad (1.11)$$

where $R_i = 1, 2$ is the relaxation rate of the aqueous solution, T_{i0} is the relaxation time of the aqueous media in the absence of the contrast agents, $r_i = 1, 2$ is the relaxivity (usually at $T = 20$ or 37°C , $\text{pH} = 7$, and $B_0 = 1.5$ or 3.0 Tesla), and C is the contrast agents concentration (in mM of Gd, Fe, or Mn). The relaxometric performance of MRI contrast agents is assessed by measuring their relaxation rates ($1/T_1$ and $1/T_2$). Though magnetic metal oxide (Fe_3O_4 , Gd_2O_3) nanoparticles have other applications, we have tried to focus only on the theranostic application of the same. Thus, the scope of this thesis limits to therapeutic application as in magnetic hyperthermia and diagnostic application as in MRI.

Gadolinium oxide (Gd_2O_3) nanoparticles

Gadolinium oxide (Gd_2O_3) nanoparticles are primarily used as MRI contrast agents. Gd^{3+} has seven unpaired electrons whose spin perturbs the proton relaxation in water resulting in an efficient shortening of longitudinal relaxation time (T_1) and increase the magnetic resonance signal intensity. They are the most commonly used contrast agents in MRI, especially for fine vasculature in MR angiography and brain tumor enhancement [87]. Gd(III) chelates are popular for no other ion has seven unpaired electrons. Inorganic crystalline gadolinium based compound nanoparticles provide a rigid crystal environment that effectively prevents the release of free Gd^{3+} and hence are considered as a new generation of T_1 contrast agents [88, 89]. A polymer coated Gd(III) chelate will stay in the blood to allow for thorough MRI examinations. It can then be degraded and cleared from the body [90]. Though the advantages of Gd chelates seem to be evident, the obvious disadvantage is that, the surface atoms are not exposed. It is widely accepted that only the gadolinium on the surface contributes to the contrast effect. Hence, the preparation of monodispersed ultra-small nanoparticles with uniform size and large surface area is very important. Several methods have been developed to synthesize small sized Gd_2O_3 nanoparticles for the application in MRI contrast agents. Preparation from gadolinium precursors in the presence of stabilizers such as polyethylene glycol or its derivatives results in stable Gd_2O_3 colloidal solutions with particle size ranging from 2 to 15 nm [91, 92].

1.5 Research Motivation

- 1) Magnetic hyperthermia is a non-invasive and non-toxic cancer treatment strategy. The existing cancer treatment strategies like surgery, radiotherapy and chemotherapy have considerable side effects like damaging the healthy tissue, often without success in case of metastatic cancer. In this juncture, magnetic hyperthermia poses very important advantages over the traditional ones- (i) the small particle size allows the magnetic nanoparticles to pass through the biological barrier (ii) injection of magnetic nanoparticles for magnetic hyperthermia is less invasive; (iii) Magnetic nanoparticles can be manipulated to target the tumor site, thus enhancing specificity; (iv) magnetic nanoparticles used for hyperthermia can be also used as a diagnostic agent for MRI. Therefore magnetic hyperthermia treatment strategy forms the prime motivation of this thesis.

- 2) As discussed earlier, the magnetic hyperthermia properties Fe_3O_4 nanoparticles are of prime interest of this thesis, due to the effect of size, shape anisotropy, composition and surface modification and is discussed in chapter 3. Increasing the size, increases the magnetic saturation leading to improved heating characteristics. Therefore we have synthesized 10 nm superparamagnetic iron oxide nanoparticles (SPIONs) and 30 nm ferrimagnetic nanoparticles (FIONs). Different shapes of Fe_3O_4 nanoparticles could result in distinct magnetic domain structures and hysteresis losses, which influence the heat dissipation of non-

superparamagnetic nanostructures. We have thus synthesized 20 nm nanospheres, nanotetragons and nanohexagons. Changing the composition of Fe_3O_4 nanoparticles by doping with divalent ions like cobalt and nickel to form CoFe_2O_4 and NiFe_2O_4 nanoparticles has significant effect on the magnetic hyperthermia properties. Surface modification of Fe_3O_4 nanoparticles improves the colloidal stability of the ferrofluid. Improved stability improves the heating efficiency of the ferrofluid system. This thesis also focuses on the improvement of colloidal stability using biocompatible surface modifying agents like proteins and thereby increasing the heating efficiency of the nanoparticles. Thus the effect of size, shape, composition and surface modification of Fe_3O_4 nanoparticles on magnetic hyperthermia are discussed in the chapter 3 of the thesis.

3) Magnetic metal oxides are intravenously injected into the bloodstream for theranostic applications like magnetic hyperthermia and MRI. Just like various physical and chemical parameters of the nanoparticles have significant effect on the biosystem, the biosystem also conversely influences the efficiency of the magnetic hyperthermia system. Though extensive research is done on the safety of magnetic nanoparticles and also magnetic hyperthermia, a detailed scientific report on the effect of AC magnetic field on the healthy and tumor tissue is not available. In chapter 4, we have attempted to make the first detailed scientific study on the same. We have found that the application of AC magnetic field influences the physiological ions in the biosystem. This in-turn causes enhanced temperature raise which contributes to the heating efficiency of magnetic

nanoparticles inside the biosystem. If this is the case, there is much possibility that this will affect the viability of the healthy tissue. But as well discussed in many research papers, magnetic hyperthermia is not supposed to damage the healthy tissue. Though Enhanced Permeation and Retention capacity of tumor morphology leads to tumor cell necrosis and apoptosis, the reason for less or no damage to healthy tissue even under the influence of magnetic field and magnetic particles spans beyond it. We have found that physiological proteins shield effect of physiological ions and impose a shielding effect on the healthy tissue. Thus physiological proteins act as biosafety agents. Thus the influence of AC magnetic field and physiological components like ions and proteins on the heating efficiency of SPIONs is discussed in chapter 4.

- 4) Synthesis of Gd_2O_3 nanoparticles as a T_1 contrast agent for diagnostic application, MR imaging is explored in chapter 5. A comparison between bare thioglycolic acid capped Gd_2O_3 nanoparticles and organic BSA conjugated Gd_2O_3 nanoparticles is discussed. In the later section of this chapter, *in-situ* photodegraded inorganic polyvinyl pyrrolidone coated Gd_2O_3 nanoparticles is discussed.

- 5) Chapter 6 of thesis explores the fabrication of multifunctional iron oxide-gadolinium oxide nanoclusters which could be used as a single potential candidate for cancer theranostics. Hydrophilic iron oxide- gadolinium oxide (Io-Go) nanoclusters were fabricated. While Fe_3O_4 nanoparticles serve as potential magnetic hyperthermia and T_2 magnetic resonance image contrast agents, the Gd_2O_3 nanoparticles of the Io-Go nanoclusters serve as potent T_1 image contrast agents for magnetic resonance imaging.

CHAPTER 2: Synthesis, Phase Transfer and Characterization Techniques

Chapter 2 focuses on the synthesis of magnetic metal oxide (Fe_3O_4 , Gd_2O_3 , CoFe_2O_4 , NiFe_2O_4) nanoparticles and their hydrophilic phase transfer. The characterization of the fabricated particles and the experimental set-ups for their applications.

2.1 Synthesis of hydrophobic magnetic metal oxide nanoparticles

Recent advancements in nanomaterials fabrication, employ physical and chemical methods to synthesize magnetic metal oxide (Fe_3O_4 , Gd_2O_3) nanoparticles. The physical methods of fabrication, include pulsed laser deposition (PLD) [93], molecular beam epitaxy (MBE) [94] and magnetron sputtering, which are used for the thin film deposition. For biomedical applications, chemical and electrochemical synthesis of magnetic nanoparticles are used [95]. Chemical method are of high efficiency and low equipment cost. Since chemical synthesis can also produce various nanostructures (like nanocubes, nanospheres, nanoring, nanotube, nanorod, nanohexagon and nanodisc, etc.), it is widely adopted for the fabrication of different nanostructures. There are a number of chemical methods like co-precipitation, thermal decomposition, micelle synthesis and hydrothermal synthesis that have developed.

Table 2.1: Comparison between four of the most commonly used chemical synthesis methods

| Synthetic method | Synthesis | Reaction temp. [°C] | Reaction period | Solvent | Surface-capping agents | Size distribution | Shape control | Yield |
|------------------------|---------------------------------|---------------------|-----------------|------------------|--|-------------------|---------------|----------------|
| co-precipitation | very simple, ambient conditions | 20–90 | minutes | water | needed, added during or after reaction | relatively narrow | not good | high/ scalable |
| thermal decomposition | complicated, inert atmosphere | 100–320 | hours–days | organic compound | needed, added during reaction | very narrow | very good | high/ scalable |
| microemulsion | complicated, ambient conditions | 20–50 | hours | organic compound | needed, added during reaction | relatively narrow | good | low |
| hydrothermal synthesis | simple, high pressure | 220 | hours–ca. days | water-ethanol | needed, added during reaction | very narrow | very good | medium |

As shown in the above table, the co-precipitation is a facile way to synthesize Fe_3O_4 nanoparticles from aqueous Fe^{3+} salt solutions by the addition of an alkali under an inert atmosphere at room temperature or at elevated temperature ($<90^\circ\text{C}$). Though the yield is highly scalable, the size distribution and shape control are a constraint. In contrast, the thermal decomposition method, based on the decomposition of organometallic precursors at high temperature ($<320^\circ\text{C}$), could achieve very narrow size distribution and very good shape control. This makes this method is a standard chemical method for the synthesis of monodisperse magnetic metal oxide (Fe_3O_4 , Gd_2O_3) nanoparticles. The microemulsion approach relies on the phenomenon that “water-in-oil” microemulsion can be formed when immiscible water is dispersed in a hydrocarbon based continuous phase. The few nanometers big water core could offers a suitable environment for controlled nucleation and growth of magnetic metal oxide (Fe_3O_4 , Gd_2O_3) nanoparticles [96].

Though shape can be tuned through selective adsorption of molecules on to facets of the nanocrystal the size distribution of the final product is not as good as the thermal decomposition method. Furthermore, the yield is also quite low. Hydrothermal method renders high quality products with good size dispersion and shape control. But it is time consuming when compared to thermal decomposition method. In this thesis, we have fabricated magnetic metal oxide (Fe_3O_4 , Gd_2O_3) nanoparticles by thermal decomposition method.

Sun et al have reported a decomposition approach for the fabrication of size-controlled monodispersed magnetite nanoparticles based on reaction between iron acetylacetonate and phenyl ether in the presence of oleic acid, and oleylamine. With the smaller magnetite nanoparticles as seeds, larger monodispersed magnetite nanoparticles of 20 nm in diameter were produced. This process does not require a size-selection procedure and is scalable [97]. The thermal decomposition of iron pentacarbonyl also produces iron nanoparticles. For instance, Hyeon et al have reported a synthesis of highly crystalline and monodispersed iron by the thermal decomposition of iron pentacarbonyl in the presence of oleic acid at 100°C [98]. Particle size and shape can be varied by controlling the experimental parameters. Decomposition of gadolinium acetate encapsulated in single wall carbon nanotubes produces Gd_2O_3 nanoparticles with a ultrasmall particle size of 2.3 nm [99]. For the synthesis of ultra-small Gd_2O_3 , the thermal decomposition route has been proved to be effective in terms of particle quality with a controlled size and narrow distribution [100, 101].

Though efforts have been made to transfer these as-synthesized nanoparticles from hydrophobic into hydrophilic phase for bio-applications [102, 103], most works still maintain oleic acid on the surface as it keeps the water molecules away from the Gd_2O_3 core, and thus contributes to the magnetic influence of Gd^{3+} to the relaxation of protons.

For all the above mentioned reasons, we have used thermal decomposition for synthesis of our magnetic metal oxide (Fe_3O_4 , Gd_2O_3) nanoparticles using iron/gadolinium acetylacetonate, oleic acid, oleylamine and benzyl ether. The oleic acid capped hydrophobic surface of the as-synthesized particles, offer a wide choice for surface manipulation for further biomedical applications.

In this thesis, magnetic metal oxide (Fe_3O_4 , Gd_2O_3 , CoFe_2O_4 , NiFe_2O_4) nanostructures were synthesized by the conventional thermal decomposition method for investigation. A simple schematic representation of the same is shown in Fig. 2.1. The potential application of these nanostructures were in magnetic hyperthermia and MRI. Therefore our aim was to fabricate magnetic metal oxide nanostructures which give high SAR value and relaxivity. The size and shape of products were controlled by adjusting reaction conditions, which will be elaborated in detail the following sections.

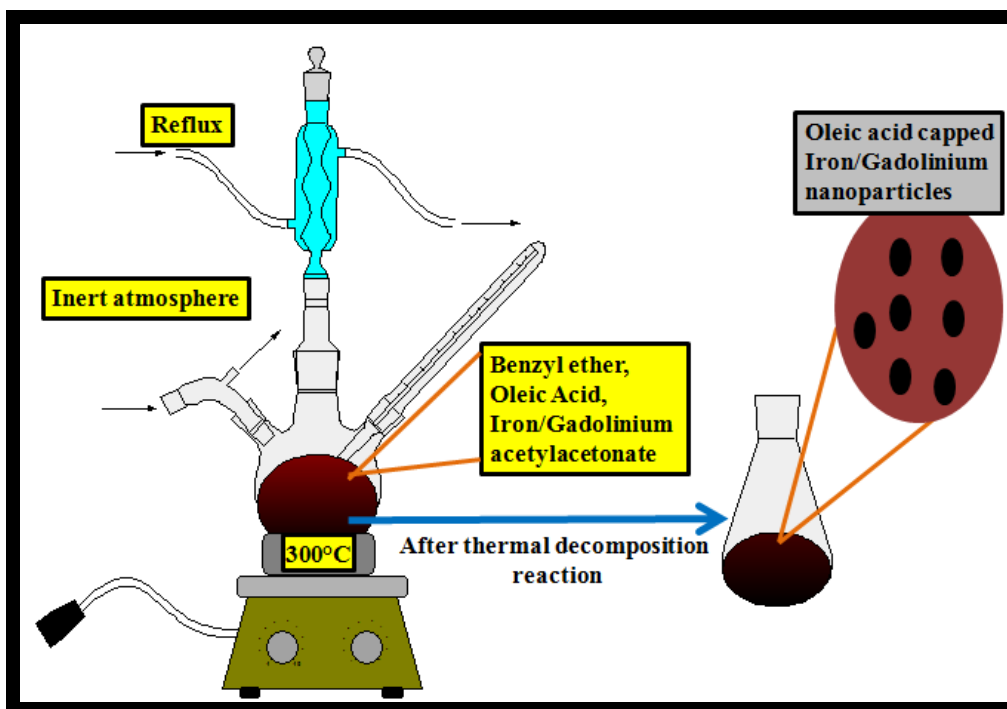


Fig. 2.1: Schematic representation of thermal decomposition method.

2.1.1 Synthesis of Fe_3O_4 nanostructures

The Fe_3O_4 nanoparticles of different sizes and shapes were chemically synthesized by the thermal decomposition method as described elsewhere [104, 105]. This is a highly preferred method for producing Fe_3O_4 nanoparticles of uniform size, shape and monodispersity. The chemical composition and physical parameters were modified as per the requirements.

Octahedral Fe_3O_4 nanoparticles

Octahedral Fe_3O_4 nanoparticles of 10 nm size were synthesized. Fe_3O_4 nanoparticles of size ≤ 10 nm are considered to be superparamagnetic and hence we call them as superparamagnetic iron oxide nanoparticles (SPIONs).

Briefly, 6 M iron (III) acetylacetonate was added to 6 mM oleic acid and 20 ml benzyl ether and heated under nitrogen purging to 110°C in order to remove moisture and maintained at the temperature for 1 hour. The temperature was later increased to 160°C and kept there for 30 minutes to initiate nucleation. The reaction was maintained at 280°C with reflux for upto 30 minutes, to promote growth of the Fe₃O₄ nanoparticles. The size of the Fe₃O₄ nanoparticles depends on the duration the reaction is maintained at 280°C. Increased duration increases the size of the particles. The particles were centrifuged by adding ethanol and hexane thrice. The product was later dispersed and stored in chloroform.

Spherical Fe₃O₄ nanoparticles

Spherical Fe₃O₄ nanoparticles of 20 nm size were synthesized. Briefly, 2 g of iron (III) acetylacetonate was added to 10 mL of oleic acid and 10 ml Oleylamine and heated under nitrogen purging to 200°C in order to remove moisture and initiate nucleation. The reaction was maintained at 200°C for 15 minutes. The temperature was later increased to 320°C with reflux for upto 1 hour, to promote growth of the spherical Fe₃O₄ nanoparticles.

Hexagonal Fe₃O₄ nanoparticles

Hexagonal Fe₃O₄ nanoparticles of 20 nm size were synthesized. Briefly, 0.3 mM of iron (III) acetylacetonate and 0.3 mM of 1,2 hexadecanediol were added to 6mM of oleic acid and 10 mL of benzyl ether heated under nitrogen

purging to 200°C in order to remove moisture and initiate nucleation. The reaction was maintained at 200°C for 15 minutes. The temperature was later increased to 320°C with reflux for up to 1 hour, to promote growth of the hexagonal Fe₃O₄ nanoparticles.

Tetragonal Fe₃O₄ nanoparticles

Hexagonal Fe₃O₄ nanoparticles of 20 nm size were synthesized. Briefly, 1.2 g of iron (III) acetylacetonate and 0.4 g of 1,2 hexadecanediol were added to 5 mL of oleic acid, 10 mL oleylamine and 10 mL of benzyl ether heated under nitrogen purging to 200°C in order to remove moisture and initiate nucleation. The reaction was maintained at 200°C for 15 minutes. The temperature was later increased to 320°C with reflux for up to 1 hour, to promote growth of the tetragonal Fe₃O₄ nanoparticles.

Cubical Fe₃O₄ nanoparticles

Cube shaped Fe₃O₄ nanoparticles of 20 nm size were synthesized. Briefly, 2 mM of iron (III) acetylacetonate and 8 mM decanoic acid were added to 50 mL diphenyl ether. The reaction mixture was heated under nitrogen purging to 200°C in order to remove moisture and initiate nucleation. The reaction was maintained at 200°C for 15 minutes. The temperature was later increased to 320°C with reflux for up to 1 hour, to promote growth of the cubic Fe₃O₄ nanoparticles.

2.1.2 Synthesis of MetalFe₂O₄ (MFe₂O₄) nanoparticles

CoFe₂O₄ nanoparticles

Cobalt Fe₂O₄ (CoFe₂O₄) were synthesized by thermal decomposition method. Briefly, 1mM of cobalt (II) acetylacetonate and iron (III) acetylacetonate was added to 2mM oleic acid, 0.64 mL oleylamine, 0.67 g 1, 2 hexadecanediol and 30 mL phenyl ether. The reaction mixture heated under nitrogen purging to 200°C for 15 min and refluxed at 320°C 1 hour, washed and stored.

NiFe₂O₄ nanoparticles

Nickel Fe₂O₄ (NiFe₂O₄) were synthesized by thermal decomposition method. Briefly, 1mM of Nickel (II) acetylacetonate and iron (III) acetylacetonate was added to 2mM oleic acid, 0.64 mL oleylamine, 0.67 g 1, 2 hexadecanediol and 30 mL phenyl ether. The reaction mixture heated under nitrogen purging to 200°C for 15 min and refluxed at 320°C 1 hour. The sample was washed by centrifuging with ethanol and hexane.

2.1.3 Synthesis of ultra-small Gd₂O₃ nanoparticles

Ultra-small Gadolinium oxide (Gd₂O₃) nanoparticles were also synthesized by thermal decomposition method. 1 mM gadolinium acetate was added to 18 mM oleic acid and 60 mM oleylamine. The reaction mixture was heated at 120°C in a for 1 hour under mild nitrogen purging remove moisture. Later the temperature was raised to 280°C immediately and maintained at the same for

6 hours. After cooling down, the mixture was treated with ethanol for the particles to precipitate. The nanoparticles were collected by centrifuging and washed with toluene and ethanol thrice. The final product was stored in 20 ml toluene or chloroform.

2.2 Hydrophilic and biocompatible phase transfer of magnetic metal oxide nanoparticles

The as-synthesised Fe_3O_4 nanoparticles were hydrophobic in nature due to the oleic acid capping. The magnetic metal oxide (Fe_3O_4 , Gd_2O_3) have to be converted to hydrophilic phase so as to use it for *invitro* and *invivo* applications.

As the magnetic metal oxide (Fe_3O_4 , Gd_2O_3) nanoparticles are usually administered intravenously or intra-arterially. Biocompatibility and prolonged blood circulation form the basis for the development of targeted magnetic hyperthermia system. This can be achieved by various surface modification/functionalization strategies. As per the desired biological application, magnetic metal oxide (Fe_3O_4 , Gd_2O_3) nanoparticles are rendered biocompatibility by different types of surface modifying agents like polymers, surfactants, biomolecules etc [106-108]., The magnetic suspensions have high magnetic susceptibility and zero coercive force with a magnetic core and hydrophilic surface, as shown in Fig. 2.2. Apart from rendering hydrophilicity and/or biocompatibility, they also help prevent agglomeration

and hence enhance the heating characteristics for magnetic hyperthermia and signalling for MRI applications.

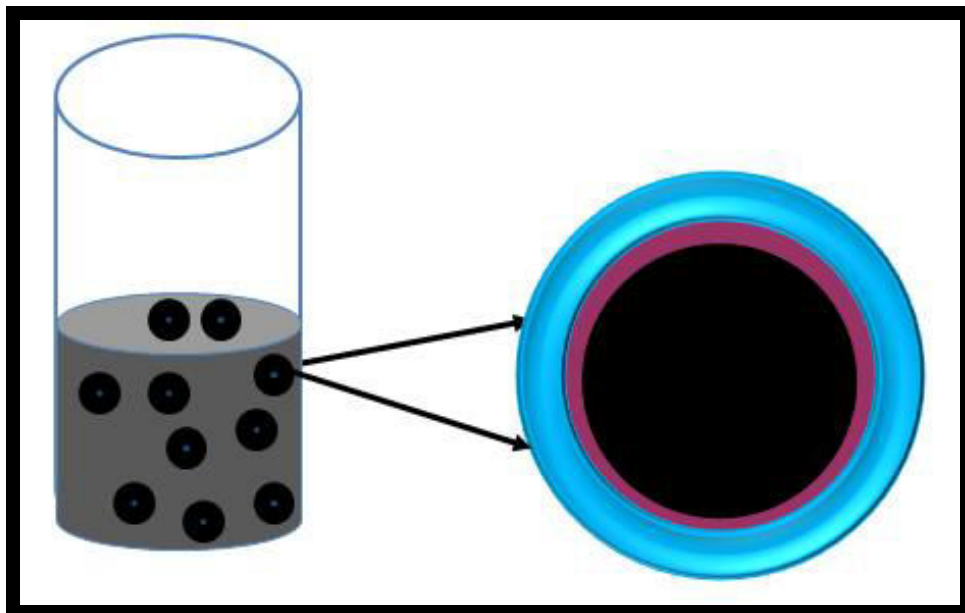


Fig. 2.2: Schematic representation of ferrofluid. The fluid consists of small magnetic particles dispersed in a liquid (left). Each particle consists of a single domain iron oxide core grafted with surfactant (right).

2.2.1 Surfactant coating

Cetyl Trimethyl Ammonium Bromide (CTAB)

The strategy of phase transfer using additional hydrophilic molecular layer over the original ligand (oleic acid) of magnetic metal oxide (Fe_3O_4 , Gd_2O_3) nanoparticles was used in this approach. Cetyl Trimethyl Ammonium Bromide (CTAB) is a quarternary salt whose hydrocarbon chains adsorb onto the oleic moiety of the magnetic metal oxide (Fe_3O_4 , Gd_2O_3) nanoparticles,

allowing the cationic ammonium moiety to face out into the solution, making the Fe_3O_4 nanoparticles hydrophilic [109]. A schematic representation of the same is shown in Fig. 2.3. In our experiments, the cationic CTAB was coated over the oleic acid capped, as-synthesized magnetic metal oxide (Fe_3O_4 , Gd_2O_3) nanoparticles. Briefly, 0.1 M of CTAB was added to 10 mg magnetic metal oxide (Fe_3O_4 , Gd_2O_3) nanoparticles. The mixture was vortexed and heated to 80°C . The reaction was stopped after 3 hours and washed.

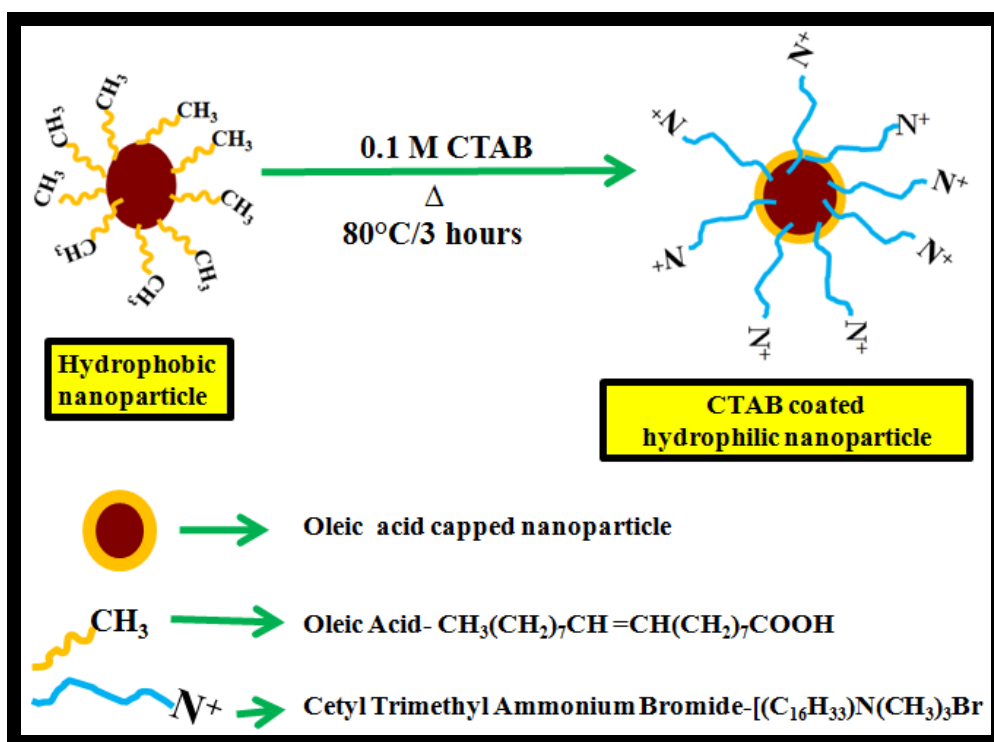


Fig. 2.3: Schematic overview of CTAB coating over metal oxide (Fe_3O_4 , Gd_2O_3) nanoparticles.

Polyethyleneimine (PEI)

PEI is anionic polymer with negative surface charges. PEI was used to coat around the oleic acid capped 1 mg magnetic metal oxide (Fe_3O_4 , Gd_2O_3) nanoparticles. Briefly, 10 mg/mL sample and 100 mg PEI were vortexed

together in water. Later the reaction mixture was maintained at in water vortex sonicate at 80°C for 2 hours. The product was centrifuged and dispersed well in water. A schematic representation of the same is shown in Fig. 2.4

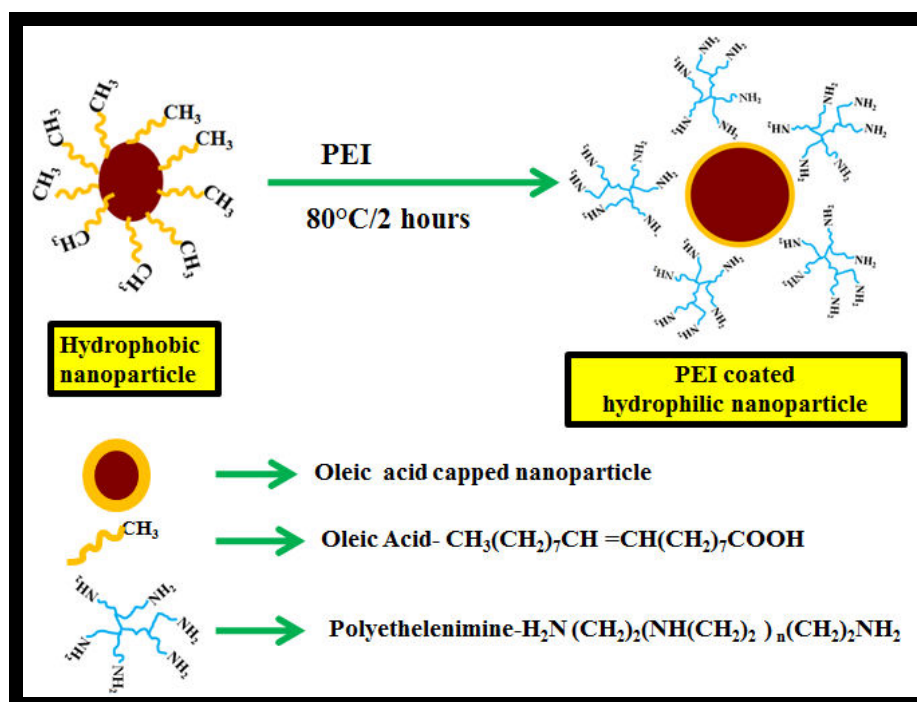


Fig. 2.4: Schematic overview of PEI coating over metal oxide (Fe_3O_4 , Gd_2O_3) nanoparticles.

2.2.2 Ligand exchange reaction

In the ligand exchange strategy, the hydrophilic ligand with more affinity towards the inorganic magnetic metal core replaces the original hydrophobic ligand capping the magnetic metal oxide (Fe_3O_4 , Gd_2O_3) nanoparticles, thus rendering hydrophilicity [110]. In our experiments, the hydrophobic oleic moiety capping the magnetic metal oxide (Fe_3O_4 , Gd_2O_3) nanoparticles is replaced by the silane group of (3-Aminopropyl) trimethoxysilane (APTMS) and thiol group of thioglycolic acid (TA).

(3-Aminopropyl) trimethoxy silane (APTMS)

The silane group of APTMS was exchanged for oleic moiety on the magnetic metal oxide (Fe_3O_4 , Gd_2O_3) nanoparticles. The amino groups are thus exposed out, causing rendering hydrophilicity. Briefly, 1 mg magnetic metal oxide (Fe_3O_4 , Gd_2O_3) nanoparticles were dispersed in 10 ml toluene. To the dispersion, 90 μL of APTMS was added and vortexed thoroughly. The mixture was kept in the shaker at room temperature for 72 hours for the ligand exchange reaction to take place. The reaction mixture was washed with ethanol and later with distilled water. The product was found to be well dispersed in water as the hydrophilic amino side faces the solvent. A schematic representation of the same is shown in Fig. 2.5.

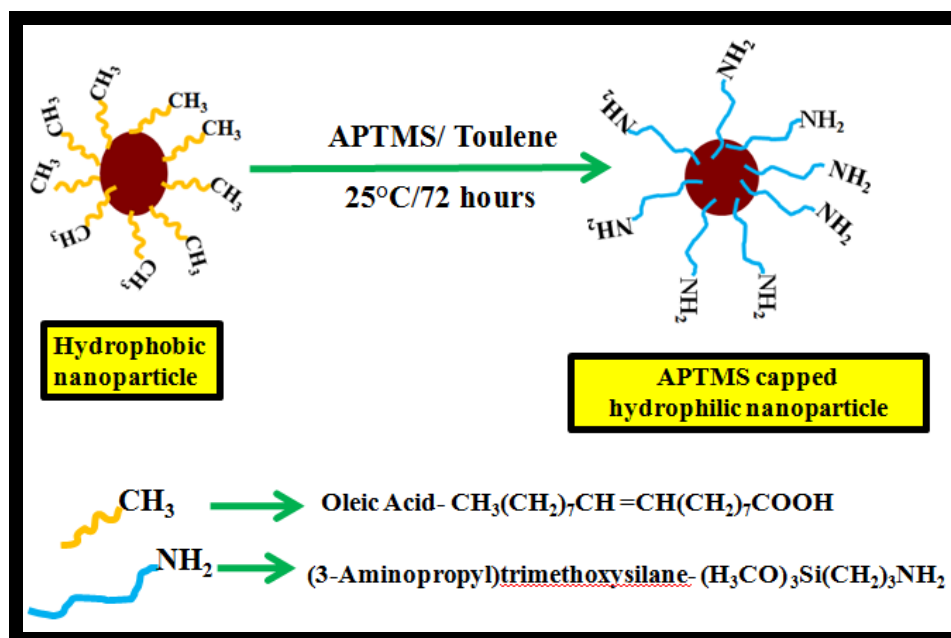


Fig. 2.5: Schematic overview of APTMS capping over metal oxide (Fe_3O_4 , Gd_2O_3) nanoparticles.

Thioglycolic acid (TA)

The thiol group of TA was exchanged for oleic moiety on the magnetic metal oxide (Fe_3O_4 , Gd_2O_3) nanoparticles. The amino groups are thus exposed out, causing rendering hydrophilicity. Briefly, 1 mg magnetic metal oxide (Fe_3O_4 , Gd_2O_3) nanoparticles were dispersed in 10 ml toluene. To the dispersion, 0.3 mM TA was added and vortexed thoroughly. The mixture was kept in the shaker at room temperature for 24 hours for the ligand exchange reaction to take place. The reaction mixture was washed with ethanol and later with distilled water. The product was found to be well dispersed in water as the hydrophilic carboxy group faces the solvent. A schematic representation of the same is shown in Fig. 2.6.

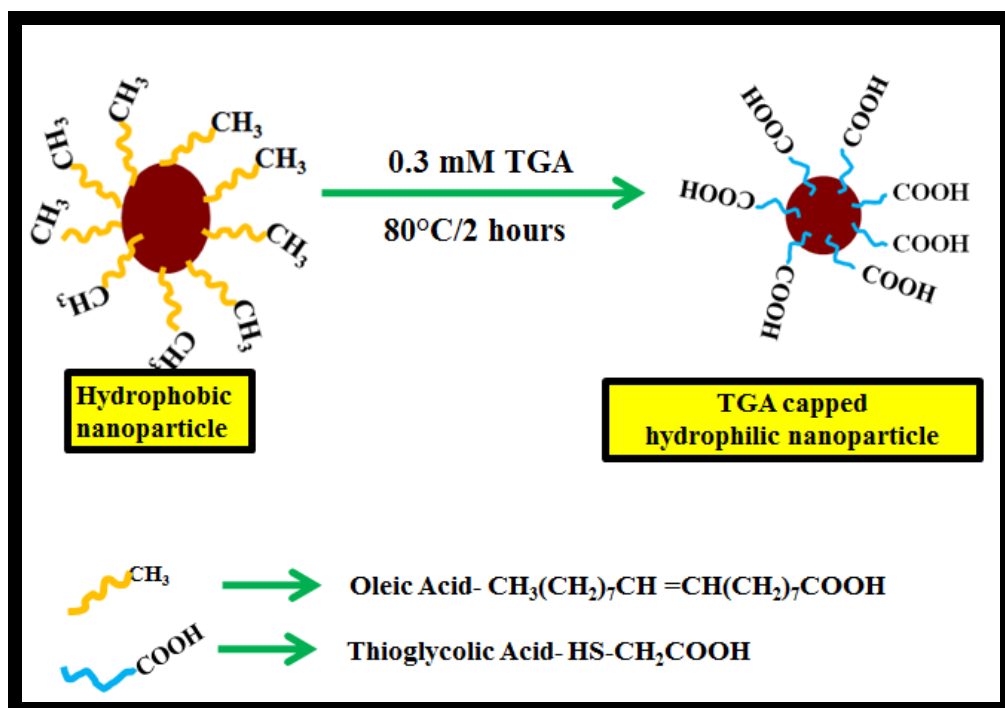


Fig. 2.6: Schematic overview of TA capping over metal oxide (Fe_3O_4 , Gd_2O_3) nanoparticles.

Poly Vinyl Pyrrolidone (PVP)

PVP is a neutral polymer. PVP of molecular weight 40000 was used to coat the magnetic metal oxide (Fe_3O_4 , Gd_2O_3) nanoparticles. 0.02 mM of PVP was added to 0.25 mM of the magnetic metal oxide (Fe_3O_4 , Gd_2O_3) nanoparticles stock solution in toluene and 1:1 volume ratio of dimethyl formamide /dichloromethane (volume ratio of 1:1) were mixed and refluxed at 80°C for 12 hours. The reaction mixture was cooled down and added dropwise to 130 ml diethyl ether and stirring rigorously. The white precipitate was collected by centrifugation. The product was washed with toluene and diethyl ether thrice and the final product was suspended in DI water. A schematic representation of the same is shown in Fig. 2.7.

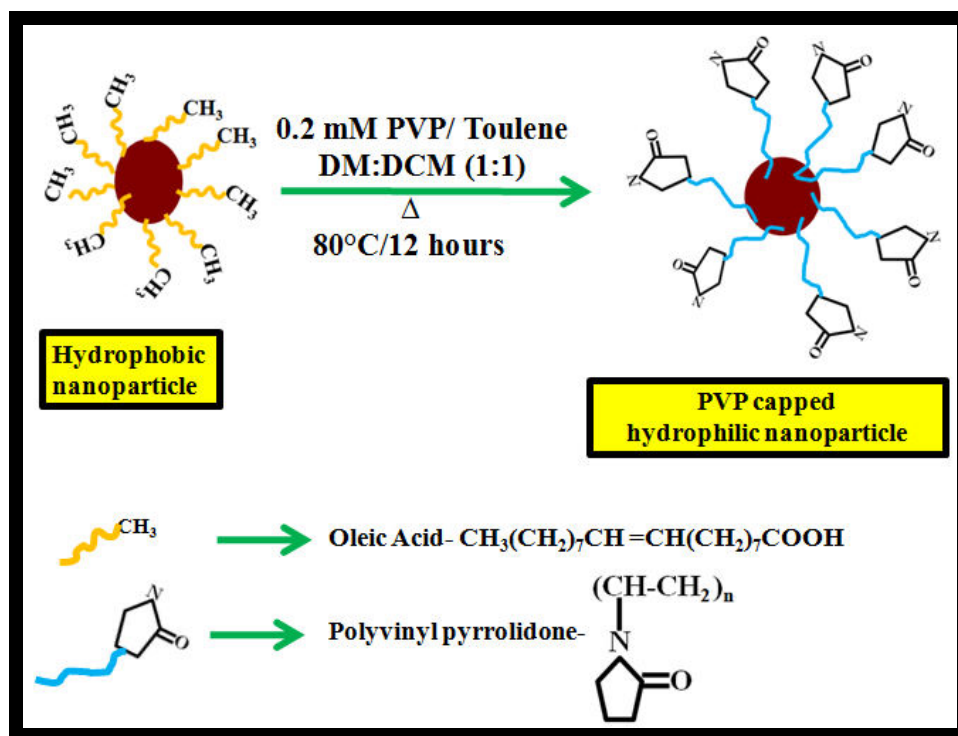


Fig. 2.7: Schematic overview of PVP capping over metal oxide (Fe_3O_4 , Gd_2O_3) nanoparticles.

Later *in situ* photodegradation of the capped PVP was done. 10 mL of 1mM PVP capped Gd_2O_3 nanoparticles was diluted upto a volume of 250 mL. UV irradiation was performed for upto 4 hours. The UV lamp was turned off after every 15 minutes and allowed to cool down for 15 minutes. The samples were retrieved every 30 minutes of UV irradiation, inorder to measure the hydrodynamic radius, so as to confirm the photodegradation of PVP chains.

2.2.3 *In situ* polymerization reaction

Dopamine was conjugated over TA capped magnetic metal oxide (Fe_3O_4 , Gd_2O_3) nanoparticles and allowed for *in situ* polymerization. Briefly, 6 mg dopamine was added to 10 mM PBS at pH 8.5. This mixture was added to 5 mg of nanoparticles and incubated in shaker overnight for conjugation and *in situ* polymerization. The product was centrifuged and dispersed in water. A schematic representation of the same is shown in Fig. 2.8.

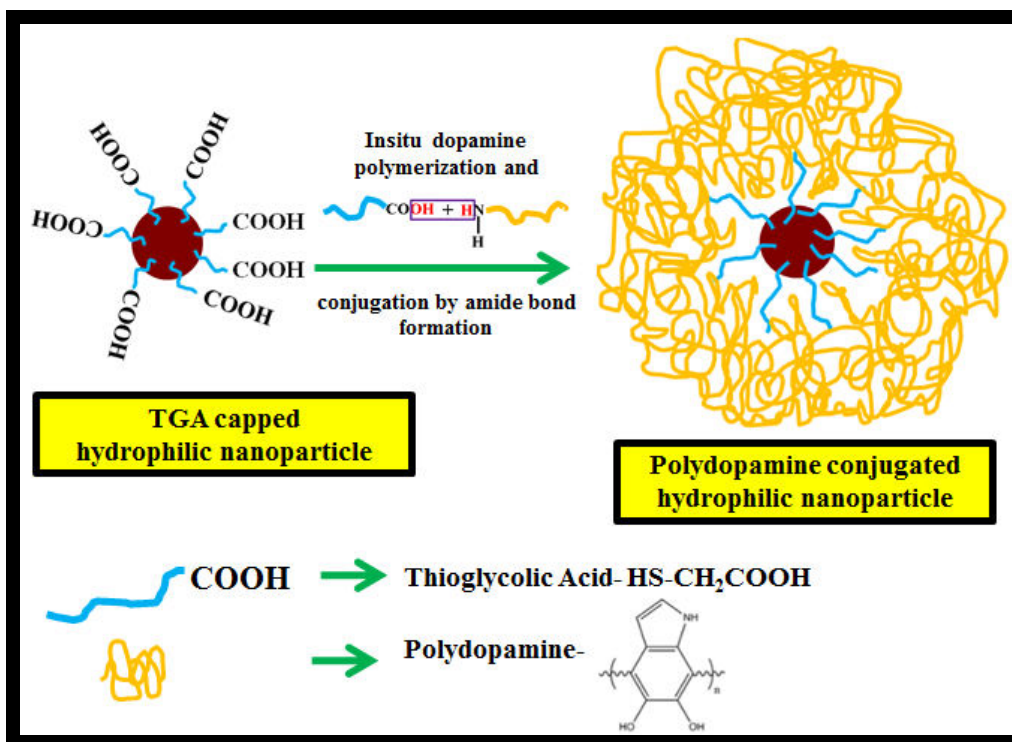


Fig. 2.8: Schematic overview of *in situ* polymerization of dopamine over metal oxide (Fe_3O_4 , Gd_2O_3) nanoparticles.

2.2.4 Biocompatible phase transfer

The APTMS capped magnetic metal oxide (Fe_3O_4 , Gd_2O_3) nanoparticles have exposed amino groups which form strong amide bond with the carboxylic groups on the BSA by the EDC method [111]. Briefly, 26 mM EDC and 10 mM NHS was prepared in MES (2-(N-morpholino) ethane sulfonic acid) buffer. 200 μL of EDC / NHS / MES mixture was added to 1 mL BSA (2 mg/mL) to activate the carboxylic group. 2 mL of APTMS-iron oxide nanoparticles were dispersed in 1xPBS (0.1 mg/mL). The pH was maintained around 7.2-7.4. Both the solutions were then mixed and left in the shaker overnight at room temperature. A schematic representation of the same is shown in Fig. 2.9.

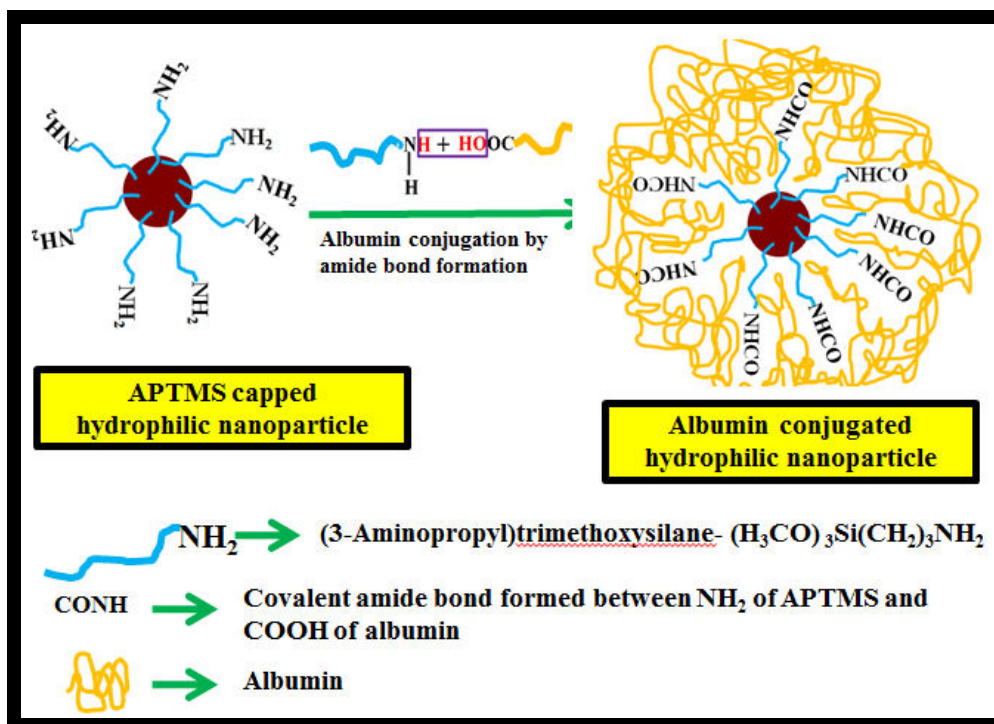


Fig. 2.9: Schematic overview of albumin conjugation over metal oxide (Fe_3O_4 , Gd_2O_3) nanoparticles.

2.3 Characterization techniques

A series of techniques were employed for the characterization of the magnetic metal oxide (Fe_3O_4 , Gd_2O_3) nanoparticles. The morphology of the nanostructures was studied by transmission electron microscopy (TEM). The crystallographic structure and purity was investigated by X-ray diffraction (XRD) and Selected Area Electron Diffraction (SAED) attached to TEM. The magnetization saturation of magnetic metal oxide (Fe_3O_4 , Gd_2O_3) nanoparticles was measured by vibrating sample magnetometer (VSM) and Superconducting quantum interface devices (SQUID). The particle size distribution, stability and surface charge of the hydrophilic particles were

investigated by a dynamic light scattering (DLS) system. The chemical bonding of the surface modified magnetic metal oxide (Fe_3O_4 , Gd_2O_3) nanoparticles was interpreted by Fourier Transform InfraRed (FTIR) spectrometer. The conjugation of biomolecules to the magnetic metal oxide (Fe_3O_4 , Gd_2O_3) nanoparticles was confirmed using Ultra Violet Spectrophotometer. The magnetic hyperthermia properties of magnetic metal oxide (Fe_3O_4 , Gd_2O_3) nanoparticles were characterized by a heat induction machine. Table 2.2 lists the make and model of the above listed instruments

Table 2.2: Make and Model of instruments used in this thesis

| S.No. | Characterization Technique | Make and Model |
|-------|--|---------------------------|
| 1 | Transmission Electron Microscopy (TEM) | JEOL 2010/3010 |
| 2 | X-Ray Diffractometer (XRD) | Bruker D8 Advance |
| 3 | Vibrating Sample Magnetometer (VSM) | Lakeshore 7404 |
| 4 | Superconducting Quantum Interface Device (SQUID) | Quantum Design, MPMS XL-5 |
| 5 | Dynamic light scattering (DLS) | Malvern Zetasizer Nano-ZS |
| 6 | UV/Vis spectroscopy | Shiamadzu –UV-1601 |
| 7 | Confocal Microscopy | Olympus Fluoview FV1000 |

| | | |
|---|--|--------------------------------|
| 8 | Flow cytometry | Flouview FV4 |
| 9 | Heat induction (Magnetic Hyperthermia) | Shenzhen Shuangping, SPG-10-II |

2.3.1 Transmission electron microscopy (TEM) and Selected Area Electron Diffraction (SAED)

Transmission electron microscopy (TEM) is the analytical tool to investigate morphology of samples. Generally, TEM is used to investigate crystal orientation, crystal structure, dislocations, composition, etc., The main components of a TEM system are electron gun, a condenser lens system, objective and intermediate lenses, a sample chamber, projector systems, vacuum systems and a holder that used to insert or remove samples [112]. In a TEM, a ultra-thin sliced sample of thickness about 100 nm is exposed to a parallel high-energy electron beam (100-400 KeV), so as to allow the electrons to pass through the sample easily. Apart from the electrons passing through the sample, some electrons are scattered to certain angles due to diffraction by atoms of sample. The bright-field and dark-field modes are the imaging methods in TEM.

Fig. 2.10 shows the schematic illustration of TEM in Bright field mode. As shown in the figure, an objective aperture is positioned on-axis with the transmitted beams and transmitted electrons are allowed to pass through and contribute to the image. For the dark-field imaging, the aperture is placed off-

axis from the transmitted beams only allowing the diffracted electrons to pass through. The dark-field mode is to study crystalline grains and defects. In addition, a TEM could perform the selected area electron diffraction (SAED) pattern.

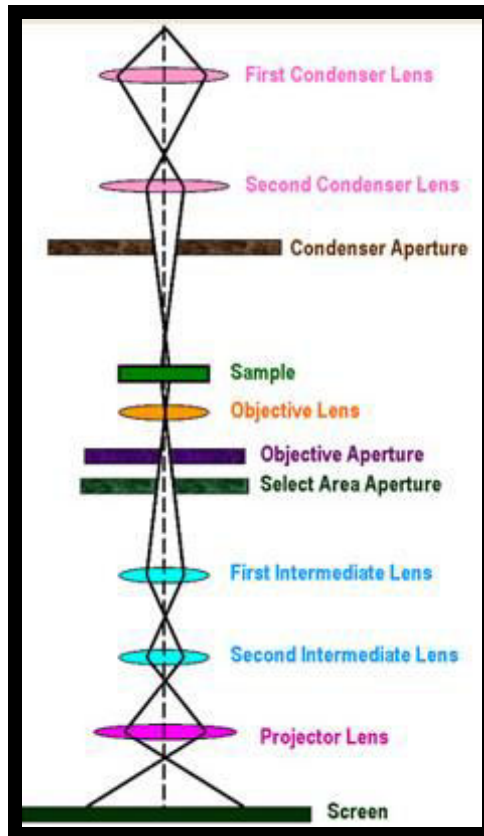


Fig. 2.10: Schematic illustration of working principle of Transmission Electron Microscope ^[107].

For a single crystalline material, the image on the screen is a series of spots, each referring to a satisfied diffraction condition of the sample's crystal structure. For a polycrystalline material, a series of rings would be observed. According to the diffraction pattern, the inter-planar distance is given by equation 2.1,

$$dhklR = L\lambda \quad (2.1)$$

where, $dhkl$ - inter-planar distance of reflecting planes $\{hkl\}$, R - the distance between the center spot on the focal plane and diffracted spot, L - distance between focal plane and sample, λ - the wavelength of the electron beam.

The SAED can be used to identify the lattice parameters and crystal structure. The operating voltage of TEM is 300 kV. Samples were prepared for imaging by drying nanoparticles on a copper grid coated with a thin layer of carbon.

2.3.2 X-Ray diffraction (XRD)

XRD is the major technique for determining the atomic and molecular structure of a crystal. It is a non-destructive technique used for the determination of lattice constants, crystalline phase, grain size, preferred orientation strain, thermal expansion, etc. The XRD is principled Bragg's law, proposed by English physicists William Lawrence Bragg in 1913. As shown in Fig. 2.10, the crystal is made of a discrete parallel planes separated by a constant distance. When the phase shift is a multiple of 2π , the interference is constructive. Therefore, when Bragg's Law shown by equation 2.2 is satisfied diffraction takes place [114]

$$2d \sin\theta = n\lambda \quad (2.2)$$

where, n - an integer corresponding to the order of diffraction, λ - the wavelength of incident X-ray, d -the inter-planar distance of reflecting planes and θ -the relative angle between the reflecting planes and incident wave.

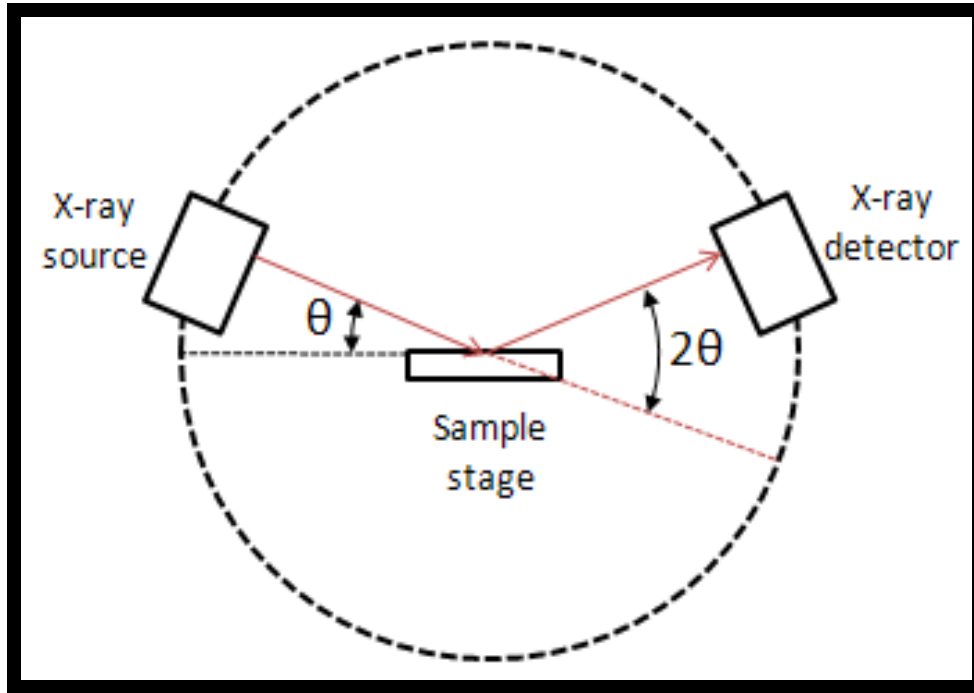


Fig. 2.11: Schematic illustration of working principle of X-Ray Diffractometer [115]

2.3.3 Vibrating sample magnetometer (VSM)

VSM is a basic technique to measure magnetostatic properties of magnetic materials. VSM works on Faraday's law of electromagnetic induction. According to which the induced electromotive force (voltage) $V(t)$ in any closed electrical circuit is proportional to the rate of the change of magnetic flux $d\Phi/dt$ through the circuit [116]. This is given by the equation 2.3,

$$V(t) = - C \cdot d\Phi/dt \quad (2.3)$$

Where C is a constant

Fig. 2.12 represents a schematic illustration of VSM system. The sample is attached on a non-magnetic holder and placed between the two

electromagnets. The sample is then sinusoidally oscillated by a vibrator made of piezoelectric material. The oscillation induces the change of magnetic flux through pick-up coil and in turn inducing an electrical signal in the coils. This electrical signal is measured by a lock-in amplifier and transferred to magnetic moment of the sample since the amplitude of the signal is proportional to magnetic moment of sample. Hysteresis loop is got by measuring the sample in the external applied field which is continuously changed from a maximum positive field to negative field and back to the maximum positive field.

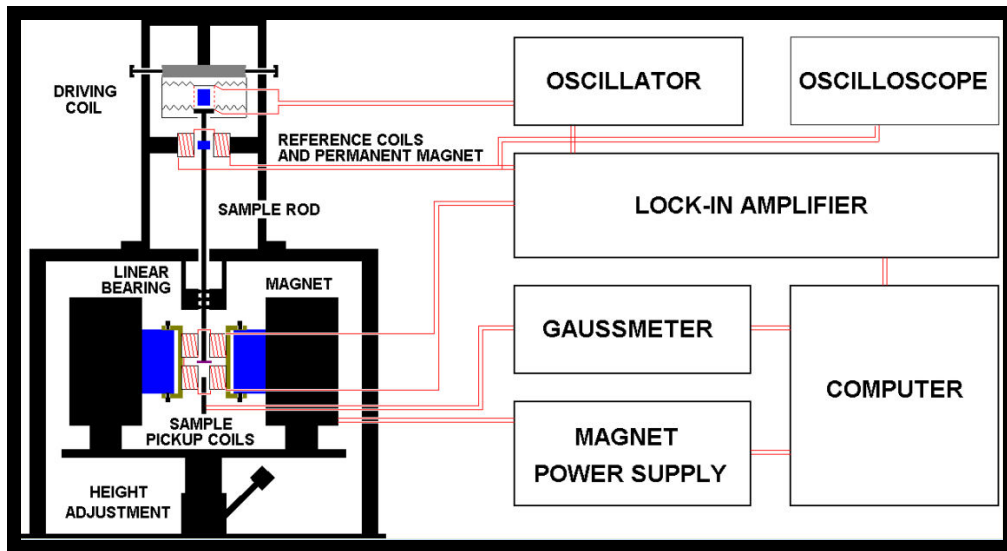


Fig. 2.12: Schematic illustration of working principle of Vibrating Sample magnetometer ^[117].

2.3.4 Superconducting Quantum Interface Device (SQUID)

SQUID is a highly sensitive magnetometer for magnetic properties investigation. It is used to measure even mild magnetic moment. The key

component of the SQUID is a superconducting material loop with one or more weak links, forming several Josephson junctions. Superconducting material found in 1911 means that at below transition temperature, it exhibits a resistant-less state. The Cooper pair transportation in a circuit proposed by Leon Cooper in 1956 explains this phenomenon. Cooper pair is a pair of electrons (or other fermions) that coupled each other by an arbitrarily small attraction. In addition, the weak links comprise of a thin insulating barrier or a non-superconducting metal. SQUID works on the principle that when a current flows between two superconductors isolated from each other by a weak link layer (Josephson junctions) [118], quantum tunneling of Cooper pairs across the gap occurs. SQUID utilizes this the property of Josephson Junctions to detect minute deviations in magnetic flux, which induces a current in the superconductor loop. By detecting the resulting electrical signal, the magnitude of the magnetic flux can be obtained. The set-up of SQUID system is depicted in Fig. 2.13. The Dewar shield helps to eliminate the, ambient electronic noise, thermal radiation and external magnetic signals. The sample was inserted into a non-magnetic straw (Quantum Design). Before starting measurement, the magnet was reset in order to remove the remnant magnetic field trapped in the superconducting coils.

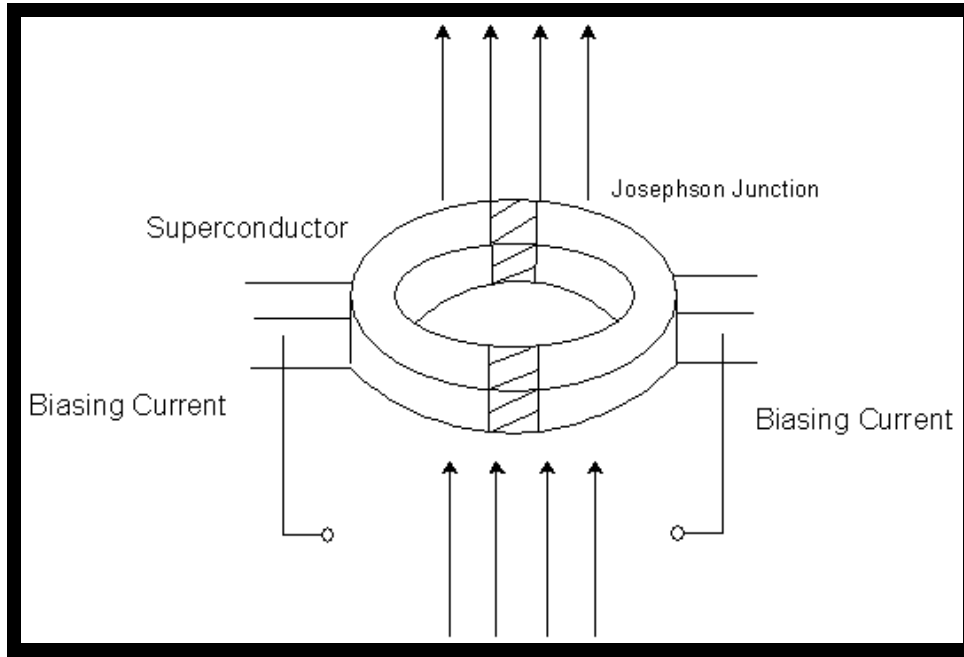


Fig. 2.13: Schematic illustration of working principle of Superconducting Quantum Interface Device ^[119].

2.3.5 Fourier Transform Infrared Spectroscopy (FTIR)

FTIR technique helps to characterize and analyse the structure and chemical composition of the sample. The light passes through a beamsplitter, which sends the light bi-directionally at right angles. One beam goes to a stationary mirror and gets back to the beamsplitter while the other hits a moving mirror. When both the beams meet up at the beamsplitter, they recombine, but the difference in their path lengths create constructive and destructive interference and thus an interferogram is obtained [120]. When the recombined beam passes through the sample, it absorbs all the different wavelengths characteristic to its spectrum, while this subtracts specific wavelengths from the interferogram. The detector

now reports differences in time and energy for all wavelengths simultaneously. The schematic diagram is given in Fig. 2.14.

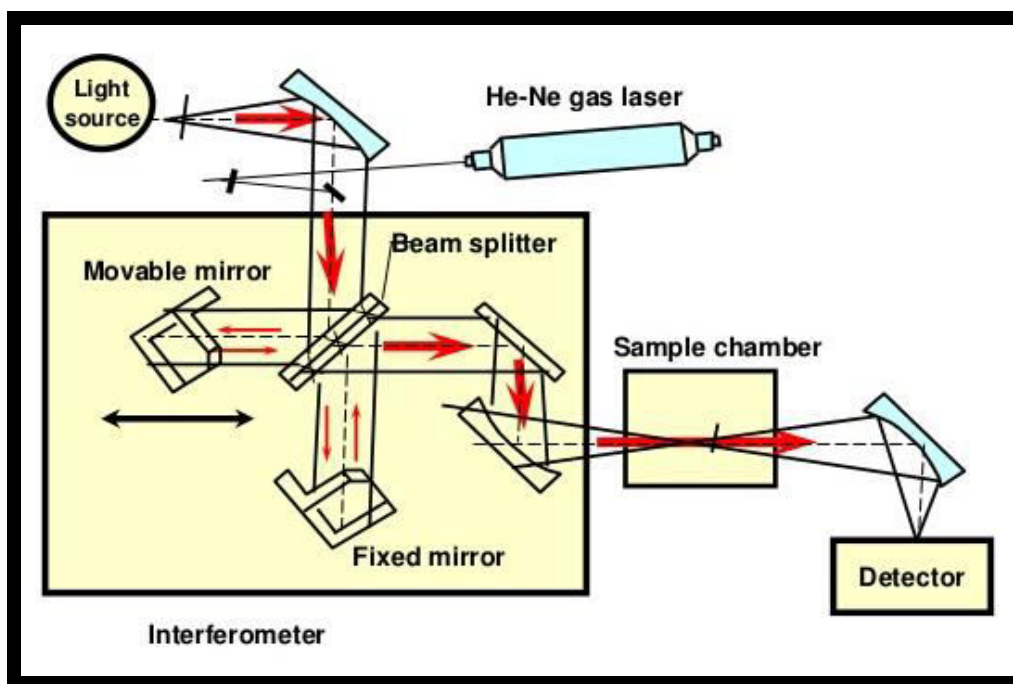


Fig. 2.14: Schematic illustration of principle of Fourier Transform Infrared Spectroscopy ^[121].

Fourier transform allows the conversion of an intensity vs time spectrum into an intensity vs frequency spectrum. The Fourier transform is given by equation 2.4.

$$A(r) = \sum_{n=1}^{\infty} X(k) \exp(-2\pi i \frac{rk}{N}) \quad (2.4)$$

Where, $A(r)$ and $X(k)$ - frequency domain and time domain points, respectively.

2.3.6 Dynamic light scattering (DLS)

DLS is the technique to determine the size distribution of small particles in suspension [122]. Fig. 2.15 illustrates a DLS set-up. The light from laser passes through a polarizer and defines polarization of the incident beam. This beam later impinges on the scattering particle. The scattered light passes through an analyzer, selecting a certain polarization, and then enters the detector where a time-dependent fluctuation in the scattering intensity is recorded. The dynamic information of the particles is derived from an autocorrelation of the intensity trace recorded during the experiment. The stability and surface charge of the colloid was also proved by DLS measurement.

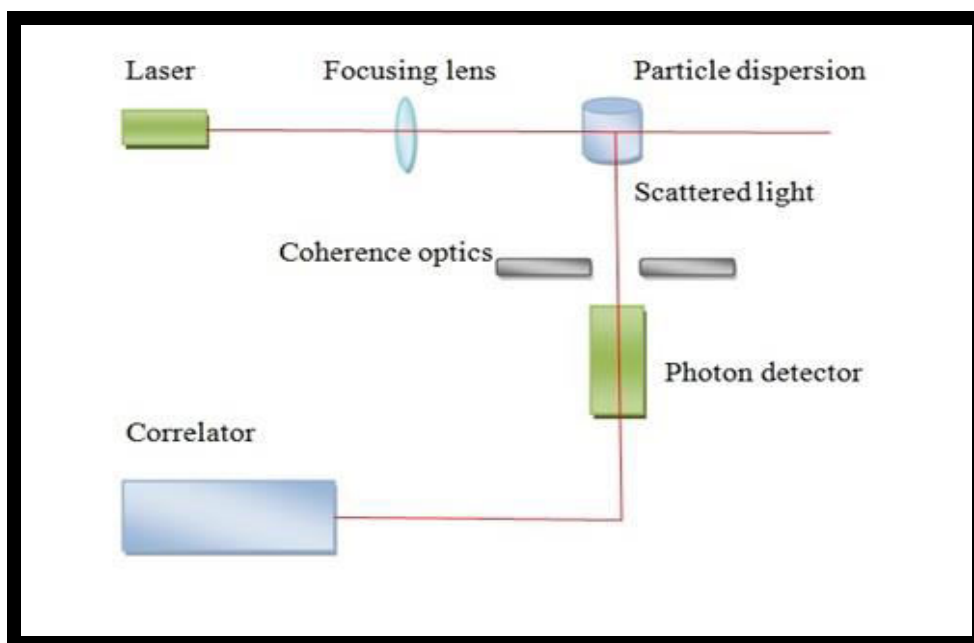


Fig. 2.15: Schematic illustration of principle of Dynamic Light Scattering [123].

2.3.7 UV/Vis spectroscopy

UV is used in analytical chemistry for the quantitative determination of different materials like transition metals, biomacromolecules etc., It measures the intensity of light passing through a sample and compares the same with the initial intensity before passing through the sample [124]. The relation between the final and initial intensity is expressed as percentage transmittance. The absorbance A is based on the transmittance given by the equation 2.5,

$$A = -\log (\%T/100\%) \quad (2.5)$$

Where, % T – transmittance.

The basic parts of the UV spectrophotometer are a light source, diffraction grating in a monochromator, a holder for the sample and a detector. The radiation source is often a Tungsten filament (300-2500 nm), a deuterium arc lamp, continuous over the ultraviolet region. The detector is a photodiode. The scanning monochromator moves the diffraction grating to "step-through" each wavelength so as to measure the intensity as a function of wavelength. Samples are placed in a cuvette with an internal width of 1 cm, which is the path length L in the Beer-Lambert law. The Fig. 2.16 gives a schematic representation of the same.

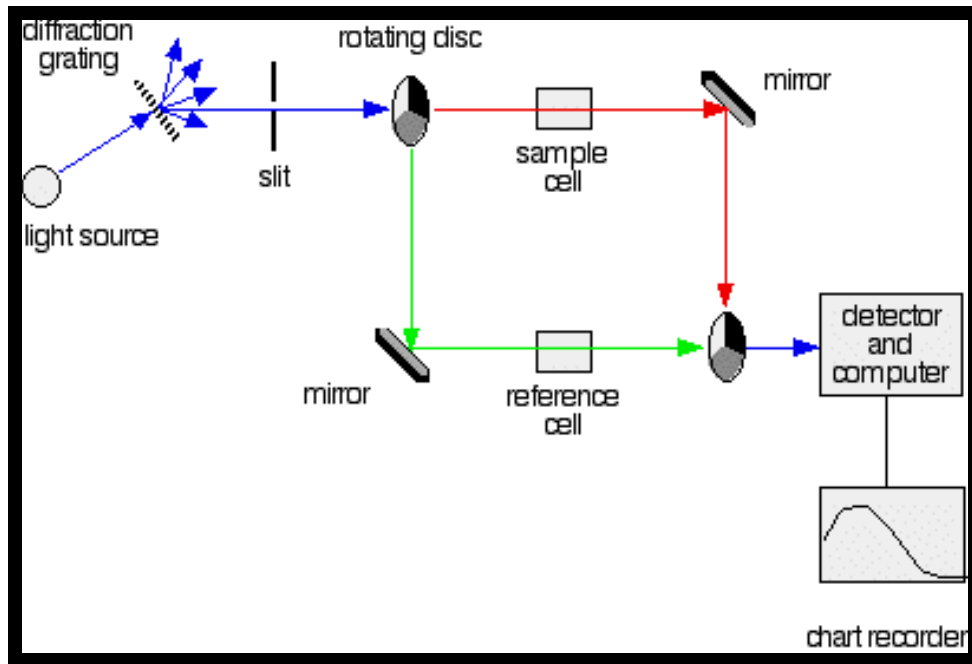


Fig. 2.16: Schematic illustration of principle of UV-Visible Spectroscopy [125]

2.3.8 Confocal microscopy

In a confocal microscope, the illumination share a common focal plane with detection light paths by 2 pinholes that are equidistant to the specimen as shown in Fig. 2.17. Usually, Krypton/Argon and Helium/Neon mixed gas lasers are used that give a range of distinct wavelengths. This light is passed through a pinhole and reflected by a beamsplitter to the objective lens and specimen [126]. The beamsplitter which is a dichroic filter acts as a mirror for the excitation. Hence, the emitted light from the specimen goes through the beam splitter to the detection pinhole and the detector. The Fig. 2.17 gives a schematic representation of the same.

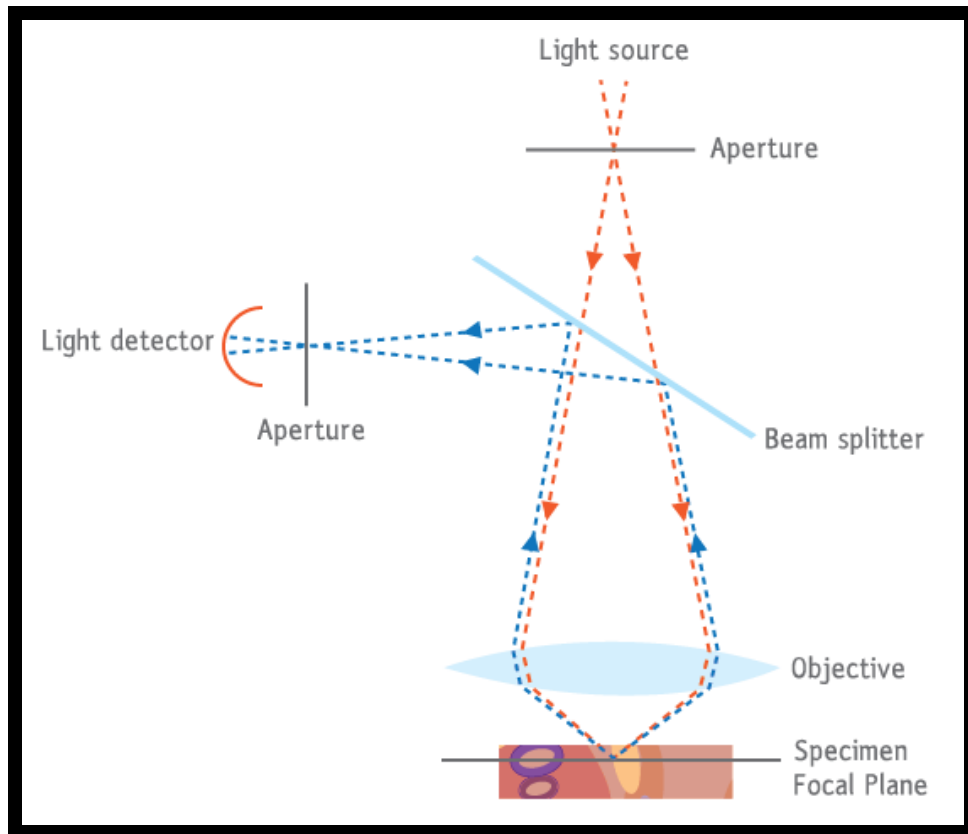


Fig. 2.17: Schematic illustration of principle of confocal microscopy ^[127].

2.3.9 Flow cytometry

Flow cytometry is used to measure the optical and fluorescence characteristics of single cells. The fluorescent molecules are excited to a higher energy state, when labeled cells are passed through a light source [128]. The fluorochromes emit light energy at higher wavelengths when they return to their resting state. Commonly used dyes for cytometry are propidium iodide, phycoerythrin, and fluorescein etc. Cells in suspension are streamed by isotonic fluid that creates laminar flow, permitting the cells to pass individually through an interrogation

point. At the interrogation point, a beam of monochromatic light from a laser, intersects the cells. Emitted light is given off in all directions and is collected by optics that direct the light into a series of dichroic mirrors that isolate particular wavelength bands. The light signals are detected by photomultiplier tubes. The resulting information is displayed in histogram. Fig. 2.18 is a schematic diagram of flow cytometer.

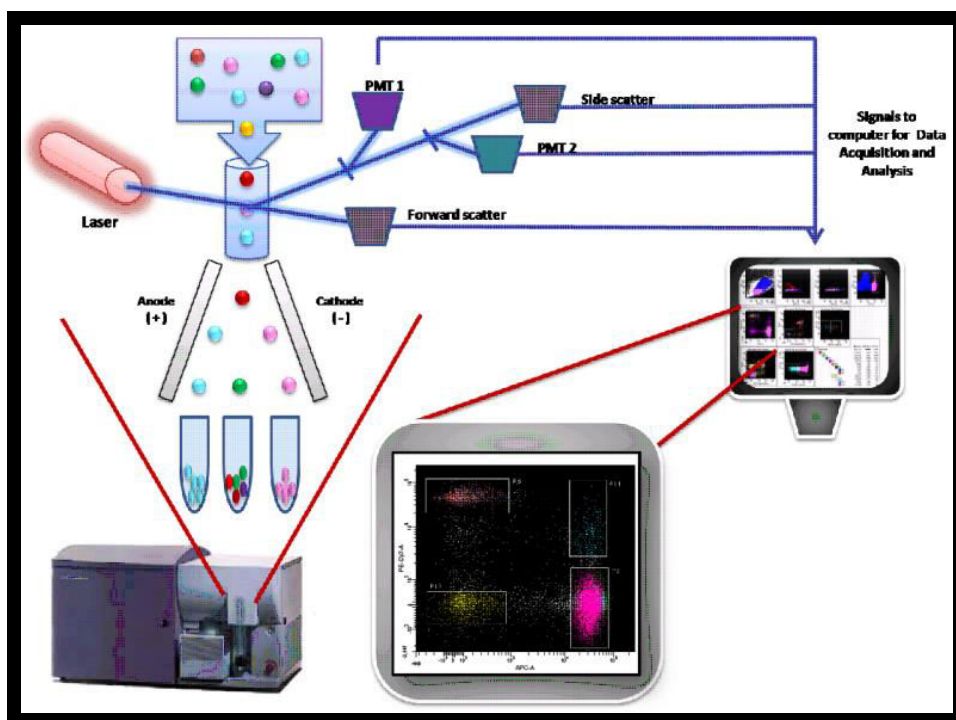


Fig. 2.18: Schematic illustration of principle of Flow Cytometry ^[129].

2.3.10 Heat Induction

The principle of magnetic hyperthermia is based on the fact that the magnetic nanoparticles, under an alternating magnetic field will generate heat which kill the tumor cells. Magnetic hyperthermia system includes AC power supplier, copper coil and a temperature measurement system, as shown in Fig 2.19.

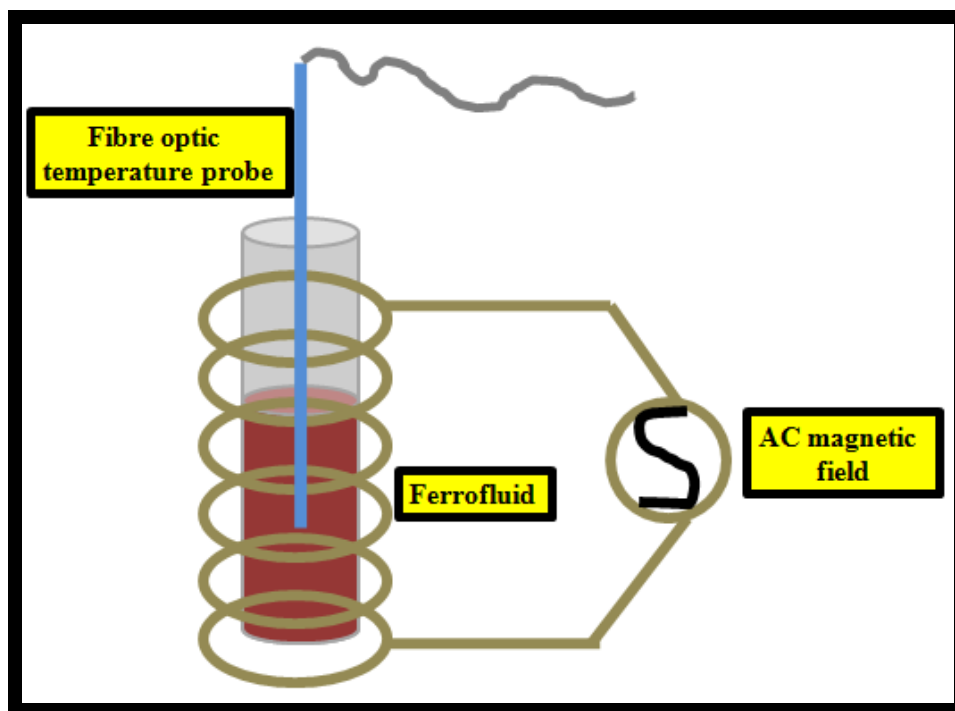


Fig. 2.19: Schematic illustration of Magnetic hyperthermia set-up.

The AC power supplier generates AC current which goes through the copper coil to generate an AC magnetic field and the amplitude of the field in the center of coil is given by equation 2.6,

$$B = \mu I \frac{N}{L} \quad (2.6)$$

Where, μ - vacuum permeability, I - current going through the coil, N - total number of turns and L - length of coil. Under the induction field, the samples in the coil generate heat that increases the temperature of sample, which is recorded by the temperature meter.

To evaluate the heat dissipation efficiency, specific absorption rate (SAR) value was calculated by equation 2.7,

$$SAR = C_{wat} \frac{\Delta T}{\Delta t} * \frac{1}{C_{Fe}} (Wg^{-1}) \quad (2.7)$$

Where, C -specific heat of water (4.18 J/g °C), $\frac{\Delta T}{\Delta t}$ - initial slope of the time-dependent temperature curve, C_{Fe} - weight fraction of magnetic element (i.e., Fe) in the sample. It should be noted that the maximum product of field amplitude and frequency (Hxf) should be below $4.5 \times 10^{10} \text{ Am}^{-1}\text{s}^{-1}$ [130] so as to avoid non-selective heating of both cancerous and healthy tissue due to eddy currents [131].

2.3.11 Magnetic Resonance Imaging (MRI)

The principle behind MRI is the directional magnetic field associated with charged particles in motion as shown in Fig. 2.20. As nuclei are charged particles, the precession of the same produces a small magnetic moment. When a human body is placed in a magnetic field, the free hydrogen nuclei align themselves parallel to the magnetic field. The nuclei precess about the magnetic

field direction like gyroscopes and is called Larmor precession [132]. The frequency of the same is proportional to the applied magnetic field strength as expressed as Larmor frequency given by the equation 2.8,

$$\omega = \gamma B \quad (2.8)$$

where, γ - gyromagnetic ratio and B - strength of the applied magnetic field.

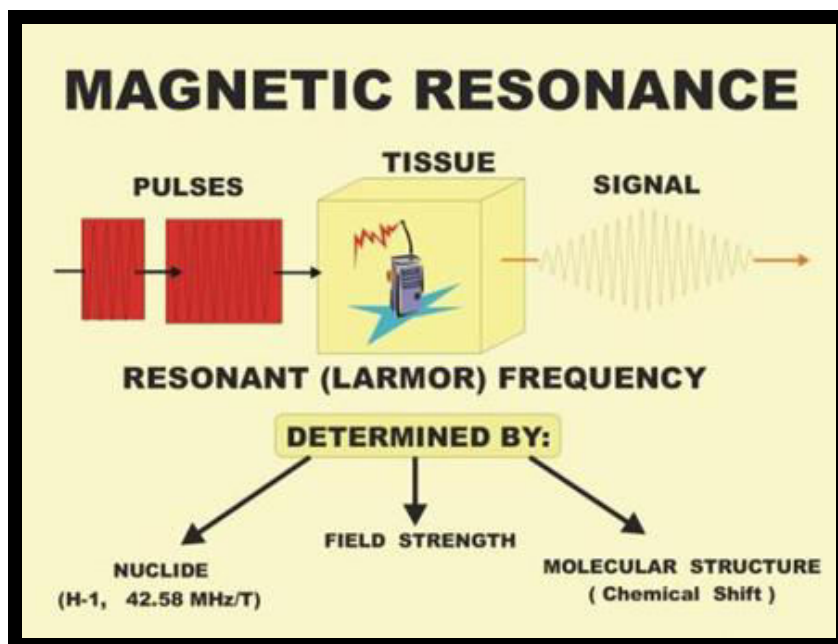


Fig. 2.20: Schematic illustration of principle of MRI ^[133].

To obtain an MR image, the object is placed under a uniform magnetic field of 0.5 to 1.5 Tesla. Once the Radio Frequency signal is removed, the nuclei realign themselves such that their net magnetic moment is again parallel with magnetic field. This return to equilibrium is referred to as relaxation. The longitudinal relaxation time is T1 and the transverse relaxation time is T2. T1 measures the time required for the magnetic moment of the displaced nuclei to realign itself with B_0 . T2 indicates the time required for the response signal from a given tissue type to decay.

Chapter 3: Fe₃O₄ Nanoparticles for Magnetic Hyperthermia Applications

3.1 Introduction

This chapter discusses our attempt to fabricate Fe₃O₄ nanoparticles for improved heating efficiency and biocompatibility for magnetic hyperthermia application. Magnetic hyperthermia is a promising cancer treatment strategy to selectively kill the tumor cells. When the temperature of the tumor site reaches 42°C, the tumor cell apoptosis and subsequent necrosis occurs. This is because of the enhanced permeation and retention characteristic of the tumor site [134, 135]. In order to minimize the adverse side effect to patients, for clinical application, the Fe₃O₄ nanoparticles should not only be biocompatible but also possess high heating efficiency in order to offer the flexibility to reduce particle concentration. Thus this chapter focuses on the experiments to try to improve the heating efficiency without compromising on the biocompatibility and the vice-versa.

Size of the Fe₃O₄ nanoparticles is the first and foremost factor in determining the heating efficiency. This is a widely researched topic in the field of magnetic hyperthermia. Increase in size increases the SAR value, as bigger Fe₃O₄ nanoparticles show higher saturation magnetization [136]. On the flip-side, bigger nanoparticles are also expected to cause cytotoxicity and are difficult to be excreted out of the biological system. We have attempted to fabricate optimum size of Fe₃O₄ nanoparticles of 10 nm superparamagnetic iron oxide nanoparticles (10 nm SPIONs) and 30 nm ferrimagnetic iron oxide nanoparticles (30 nm

FIONs), without compromising on the heating characteristics and biocompatibility. This is discussed in the first section. The next section explores the convenient shape of the Fe₃O₄ nanoparticles. Different shapes prefer different magnetic domain structures for in order to minimize the energy, leading to enhanced variation in both static and dynamic magnetic properties. Nanospheres, nanohexagons and nanotetragons each of size 20 nm Fe₃O₄ nanoparticles were fabricated, due to the ease of synthesis and reproducibility of 20 nm nanoparticles. Varying the composition of Fe₃O₄ nanoparticles by partially replacing the ferrous ions with divalent like cobalt and nickel with higher anisotropy, increases the magnetic properties even at superparamagnetic regime. Difference in geometrical arrangement of nanoparticles in suspensions also influences the magnetization. The third section explores the fabrication of Fe₃O₄ nanoparticles with varying composition using cobalt and nickel.

After discussing size, shape and composition of Fe₃O₄ nanoparticles for improving heating efficiency, the last section discusses about enhancing both the biocompatibility and heating efficiency of Fe₃O₄ nanoparticles combinatorially by albumin conjugation. Extensive research has been done to improve the biocompatibility and blood circulation of iron oxide nanoparticles by numerous surface modification and functionalization strategies for various biomedical applications [137-139]. Similarly, various attempts have been made to enhance the Specific Absorption Rate (SAR) value of the iron oxide nanoparticles by

controlling the aggregation, saturation magnetization, anisotropy, etc., [140, 141]. The size and shape of the iron oxide nanoparticles can also be controlled in order to improve the SAR value and thereby enhance the heating characteristics [142]. Achieving both biocompatibility and improved heating efficacy without compromising on either factor poses a huge challenge in the research of clinical magnetic hyperthermia. Biocompatible Fe₃O₄ nanoparticles for magnetic hyperthermia using polymers like poly ethylene glycol (PEG), poly vinyl pyrrolidone (PVP), poly ethyleneimine (PEI), biomacromolecules like proteins, aptamers, DNA, surfactants like CTAB etc., are well reported [143, 144]. Combinatorial approach to simultaneously improve the biocompatibility and SAR value using noble metal like Platinum coated iron oxide core-shell nanoparticles are also reported [145, 146]. Chemical surface modifying agents render good hydrophilicity and stability to the Fe₃O₄ nanoparticles. But they are cytotoxic when used beyond the optimum threshold level [147, 148]. Therefore biomacromolecules like DNA, proteins etc., are preferred surface functionalization agents. For our work, we have chosen Bovine Serum Albumin (BSA) as the biocompatibility agent. Albumin, is a versatile protein which forms almost 55% of blood plasma protein content and helps to maintain the pH and osmotic pressure of blood [149, 150]. Thus BSA conjugation improves the stealth characteristics of iron oxide nanoparticles and hence prolongs the blood circulation time [151, 152]. BSA is also reported to raise the temperature of a nanoparticle system under an applied AC magnetic field by the formation

of isotropic clusters [153]. Previous reports of Human Serum Albumin (HSA) conjugated superparamagnetic iron oxide nanoparticles (SPIONs) by Keshavarz et al and BSA conjugated SPIONs by Samanta et al [154] also show that albumin conjugation improves the colloidal stability and thereby the SAR value for magnetic hyperthermia. In these reports SPIONs were synthesized by inorganic co-precipitation method and albumin was conjugated by physical adsorption method. Thus we have chosen BSA as our single preferred candidate for both improved biocompatibility and enhanced heating efficiency. Moreover ferrimagnetic iron oxide nanoparticles (FIONs) have higher saturation magnetization and hence better SAR value than SPIONs [155, 156]. The unique heat enhancement property of BSA adds further value to heating efficiency of FIONs. Therefore BSA and FIONs are the candidates of interest for the single combinatorial approach to address the challenges in magnetic hyperthermia. We have fabricated BSA conjugated SPIONs of size 10 nm and FIONs of size 30 nm using the highly preferred thermal decomposition method.[157, 158]. Two surface modifying agents viz, Cetyl Trimethyl Ammonium Bromide (CTAB) and 3-Aminopropyltrimethoxysilane (APTMS) were used to render preliminary hydrophilicity to the as-synthesized hydrophobic iron oxide nanoparticles and also to facilitate the conjugation of BSA by two different approaches

3.2 Method

Blood aggregation and haemolytic studies

Erythrocytes were collected by centrifuging the blood of 5 weeks old SCID mice at 700 rpm. The pellet was re-suspended in saline at a ratio of 1:4. The test samples- as- Fe₃O₄ nanoparticles, hydrophilic Fe₃O₄ nanoparticles and biocompatible Fe₃O₄ nanoparticles, each of ferric ion concentration 0.5 mg/mL were added to the erythrocytes and the samples were incubated at 37°C for 2 hours. Distilled water, which leads to 100% lysis was used as the positive control. 0.1 M NaCl was used as negative control, as it is isotonic with the intracellular solute concentration. Haemolysis of erythrocytes is due to the oxidative stress caused by the test samples on the erythrocytes. The stress ruptures the cell membrane of the erythrocytes and hence the haemoglobin (Hb) leaks out into the solution. The absorbance of the leaked haemoglobin was measured at 540 nm by UV–Vis spectrophotometer. % Haemolysis can be calculated using the formula,

$$\%Haemolysis = [A_t - A_n / A_c - A_n] * 100$$

Where, A_t- absorbance of the test sample at 540 nm; A_n- absorbance of the negative control (0.1M NaCl) at 540 nm; A_c- absorbance of the positive control (distilled water) at 540 nm. The haemolytic index was also calculated according to ASTM F756-00 standards, according to which, 0-2% is non-haemolytic; 2-5% is mildly haemolytic and >5% is haemolytic [159].

Cell viability studies

The healthy Baby Hamster Kidney (BHK) cells suspended in 1xPBS were co-incubated with 100 µg/mL of samples for 24 hours at 37°C. The BHK cells after incubation were run under flow cytometry. Dyes NucBlue (ThermoFischer Scientific) to stain the total nuclei of cells, AlexaFluor (Invitrogen) to stain the apoptotic cells green and Propidium Iodide (PI-ThermoFischer Scientific) to stain the nucleus of dead cells red were used to qualitatively visualize the cells. Briefly, to 1 mm² of the BHK cells, 2 drops of NucBlue, 2.5 µL of AlexaFluor and 0.5 µL of PI were added along with 100 µL binding buffer and were incubated at room temperature for 15 minutes. The reaction was stopped by adding excess binding buffer and the samples were run in flow cytometry. In the histogram comprises of 4 quadrants. Quadrant 1 (Q1) represents cells that have under gone complete necrosis; Quadrant 2 (Q2) represents cells at late stage apoptosis, wherein the cell membrane has ruptured; Quadrant 3 (Q3) represents cells at early stage apoptosis; Quadrant 4 (Q4) represents live cells. The BHK cells after incubation were also observed under confocal microscope (Olympus-FluoView, FV1000). The images were later processed using the software IMARIS 8.0.

Magnetic hyperthermia experiments

The magnetic hyperthermia studies, to calculate the Specific Absorption Rate (SAR) were carried out by placing the sample inside a copper coil generating an external AC magnetic field. The temperature raise due to 0.1 mg/mL each sample with respect to the time of exposure of the sample to an AC magnetic field at an amplitude of 32.4 kAm⁻¹, frequency of 360 kHz and a magnetic field of 600 Oe was investigated. SAR is expressed as the heat released by the magnetic iron oxide nanoparticles under a magnetic field. The SAR value is calculated from the formula,

$$SAR = C_{wat} \frac{\Delta T}{\Delta t} * \frac{1}{C_{Fe}} (Wg^{-1})$$

Where, C_{wat}- specific heat of the medium (distilled water), 4.18 J /g/ °C; ΔT/Δt- initial slope of the time-dependent temperature curve; C_{Fe}- concentration of ferric ions in the medium, 0.1 mg/mL. The concentration of ferric ions in the samples was determined using ICP-OES analysis (Perkin-Elmer Dual view Optima 5300 DV ICPOES system).

The effect of AC magnetic field and 0.1 mg/mL BSA conjugated 30 nm ferrimagnetic iron oxide nanoparticles (FIONs) on healthy liver tissue was studied. Liver was treated with 0.1 mg/mL sample and an applied AC magnetic

field of 600 Oe (frequency 360 kHz), to bring a ΔT of upto 42°C-45°C. The healthy tissue before and after treatment were observed under confocal microscope (Olympus-FluoView, FV1000). Dyes NucBlue (ThermoFischer Scientific) to stain the total nuclei of cells, AlexaFluor (Invitrogen) to stain the apoptotic cells green and Propidium Iodide (PI-ThermoFischer Scientific) to stain the nucleus of dead cells red were used to qualitatively visualize the excised organ tissue. While the nuclei of the live cells are stained blue, the nuclei of completely dead cells (necrosis) appear pink. Briefly, to 1 mm² of the excised tissue, 2 drops of NucBlue, 2.5 μ L of AlexaFluor and 0.5 μ L of PI were added along with 100 μ L binding buffer and were incubated at room temperature for 15 minutes. The reaction was stopped by adding excess binding buffer and the samples were viewed under the confocal microscope. The images were later processed using the software IMARIS 8.0. Our preliminary studies are based on the qualitative observations of the stained cells/tissue morphology.

3.3 Results and Discussion

3.3.1 Fe₃O₄ nanoparticles of different sizes

Synthesis and hydrophilic phase transfer of Fe₃O₄ nanoparticles of different sizes

We have synthesized 10 nm and 30 nm Fe₃O₄ nanoparticles of octahedral and cubic geometry respectively. Fig. 3.1(a-i) shows the TEM image of the as-synthesized hydrophobic oleic acid capped 10 nm Fe₃O₄ nanoparticles. We have synthesized 30 nm Fe₃O₄ nanoparticles. It is evident from the image that the Fe₃O₄ nanoparticles were monodisperse with uniform size distribution. Fig. 3.1(b) shows that the particles were mono crystalline and pure. Fig. 3.1(b-i) gives the SAED pattern of Fe₃O₄ nanoparticles corresponding to (111), (220), (311), (400), (422), (440) and (511). From Fig. 3.1(b-ii), the diffraction peaks can be indexed as cubic spinel Fe₃O₄ (JCPDS no.19-0629), corresponding to (220), (311), (400), (422), (511) and (440). The broad peaks of 10 nm Fe₃O₄ nanoparticles and sharp peaks of 30 nm Fe₃O₄ nanoparticles also confirm the size of the particles. The saturation magnetization (Ms) value of the as-synthesized 10 nm and 30 nm Fe₃O₄ nanoparticles are 45 emu/g and 87 emu/g respectively as shown in the Fig. 3.1(c-i). 30 nm Fe₃O₄ nanoparticles have a higher magnetic saturation which makes it our preferred candidate for magnetic hyperthermia

application. The inset figure in Fig. 3.1(c-i), shows the coercivity exhibited by 30 nm Fe₃O₄ nanoparticles (30 nm FIONs). SQUID magnetometer was used to further characterize ferrimagnetic behaviour of 30 nm FIONs. The magnetization hysteresis loops at different temperatures are shown in Fig. 3.1(c-ii). As observed from the loops, the coercivity increases as the temperature decreases. All our magnetization studies show the characteristic ferrimagnetic behaviour of 30 nm Fe₃O₄ nanoparticles. The temperature dependent Field Cooling (FC) and Zero-Field Cooling (ZFC) magnetization were measured for the 30 nm Fe₃O₄ nanoparticles (30 nm FIONs). The Verwey transition temperature (T_v) is the reflection point of the characteristic magnetization jump and is deduced from a ZFC plot derivative as shown in Fig. 3.1(c-iii). The T_v of the as-synthesized 30 nm 30 nm Fe₃O₄ nanoparticles is around 115 K, which is very close to the characteristic T_v of 120 K for magnetite as reported extensively [160, 161]. The minor shift is commonly observed in magnetite (Fe₃O₄) nanoparticles. Also we further conclusively confirm that the as-synthesized 30 nm Fe₃O₄ nanoparticles are ferrimagnetic nature, in accordance to our extensive studies [162]. The higher magnetic saturation of 30 nm Fe₃O₄ nanoparticles make it our preferred candidate for magnetic hyperthermia application.

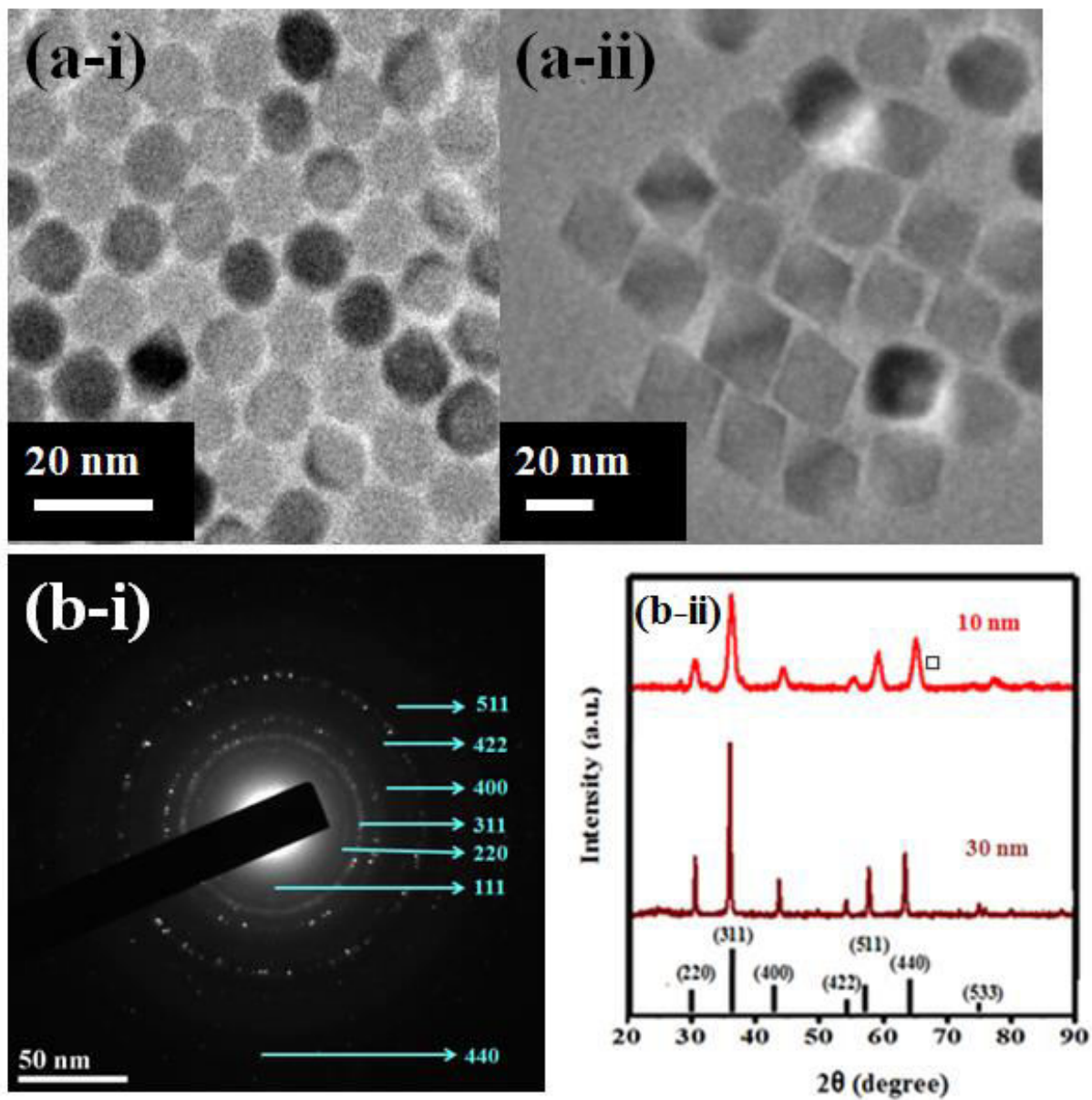


Fig. 3.1: Characterization of as-synthesized Fe_3O_4 nanoparticles (a-i) TEM image of 10 nm SPIONs (a-ii) TEM image of 30 nm FIONs (b-i) SAED pattern of Fe_3O_4 nanoparticles (b-ii) XRD plots of Fe_3O_4 nanoparticles

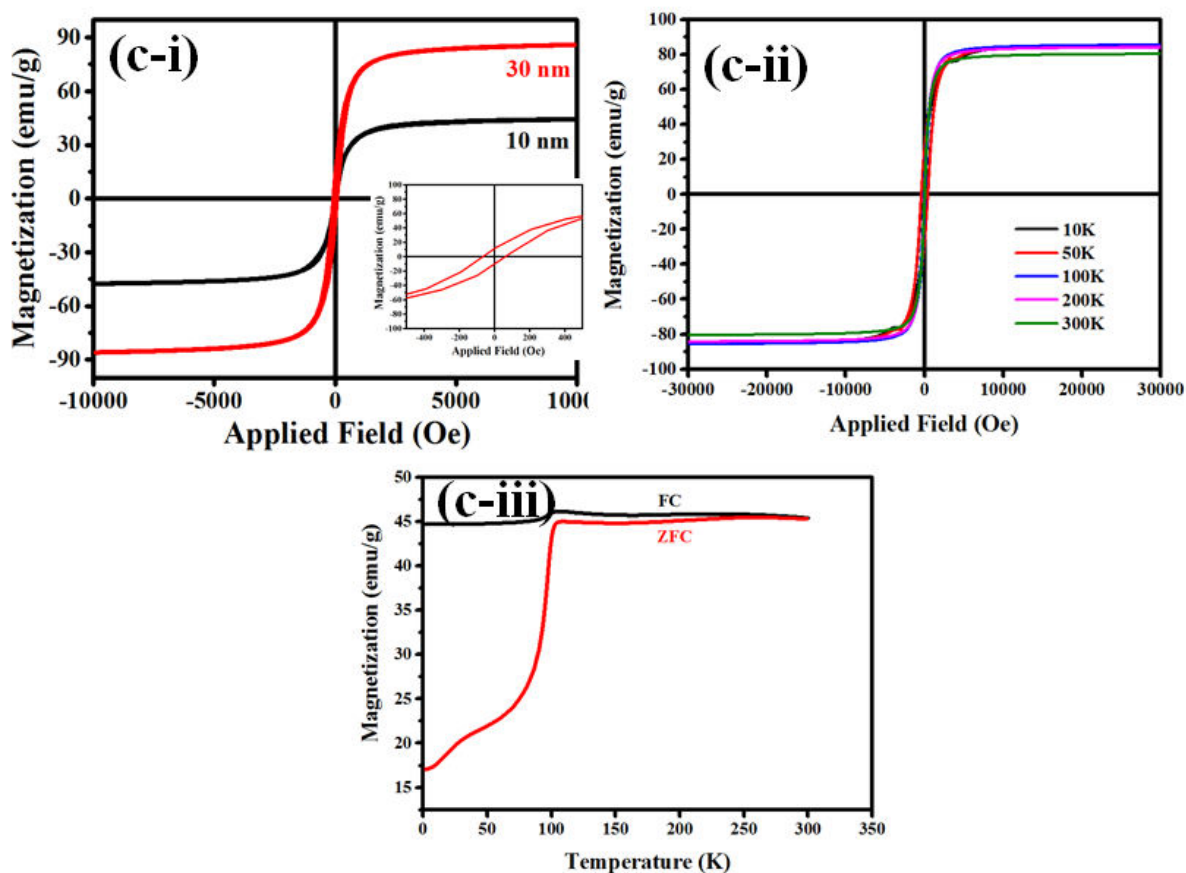


Fig. 3.1: (c-i) saturation magnetization (M_s) of Fe₃O₄ nanoparticles. Inset image shows the coercivity of 30 nm FIONs (c-ii) magnetization hysteresis loops of 30 nm FIONs at different temperatures (c-iii) Verwey transition temperature (T_v) of 30 nm FIONs.

The hydrophobic as-synthesized Fe₃O₄ nanoparticles were surface modified to hydrophilic phase using three different surface modifying agents- Cetyl Trimethyl Ammonium Bromide (CTAB), (3-Aminopropyl) trimethoxysilane (APTMS) and Polyethyleneimine (PEI). The FTIR plot in Fig.3.2(a-i) confirms that the CTAB was coated over the Fe₃O₄ nanoparticles. The peaks corresponding to 2900 1/cm is due to C- H stretching and 1440 1/cm is due to the scissoring vibration of

methylene and asymmetric bending mode of the head [N(CH₃)₃] methyl group [163]. The FTIR peak corresponding to 592 1/cm in plot is related to the Fe–O group and thus confirm the existence of Fe₃O₄. For the APTMS coated Fe₃O₄ nanoparticles, the peaks at 1700 1/cm and 1648 1/cm are due to the stretching vibration of C=O and stretching vibration of C=C bonds, respectively. The peaks at 1172 1/cm and 1017 1/cm are due to the stretching vibration of C–O. The asymmetric stretching vibration and scissoring bending vibration of CH₂ group is represented by peaks at 2926 1/cm and 1460 1/cm, respectively [164]. The FTIR peak corresponding to 592 1/cm in plot is related to the Fe–O group and thus confirm the existence of Fe₃O₄. This is evident from Fig. 3.2(a-ii) For the PEI coated Fe₃O₄ nanoparticles, the peaks at 3420 1/cm is due to NH and peaks corresponding to 2925 1/cm and 2852 1/cm are due to the asymmetric stretching vibration of CH₂. The FTIR peak corresponding to 592 1/cm in plot is related to the Fe–O group and thus confirm the existence of Fe₃O₄. This is evident from Fig. 3.2(a-iii). Fig. 3.2(b-i) and 3.2(b-ii) shows the average hydrodynamic radius of the hydrophilic 10 nm and 30 nm Fe₃O₄ nanoparticles.

As expected, due to their longer polymer chain length, PEI coated 10 nm and 30 nm Fe₃O₄ nanoparticles have a bigger size of 21±2 nm and 52±2 nm respectively. The CTAB coated 10 nm and 30 nm Fe₃O₄ nanoparticles have an average hydrodynamic radius of 19±2 nm and 40±2 nm respectively. Since APTMS immediately caps the Fe₃O₄ nanoparticle surface, they have the smallest average

hydrodynamic radius of 15 ± 2 nm and 36 ± 2 nm for 10 nm and 30 nm Fe₃O₄ nanoparticles respectively. The hydrophilic Fe₃O₄ nanoparticles were stable even upto a period of 1 month, as shown in Fig. 3.2(b-iii).

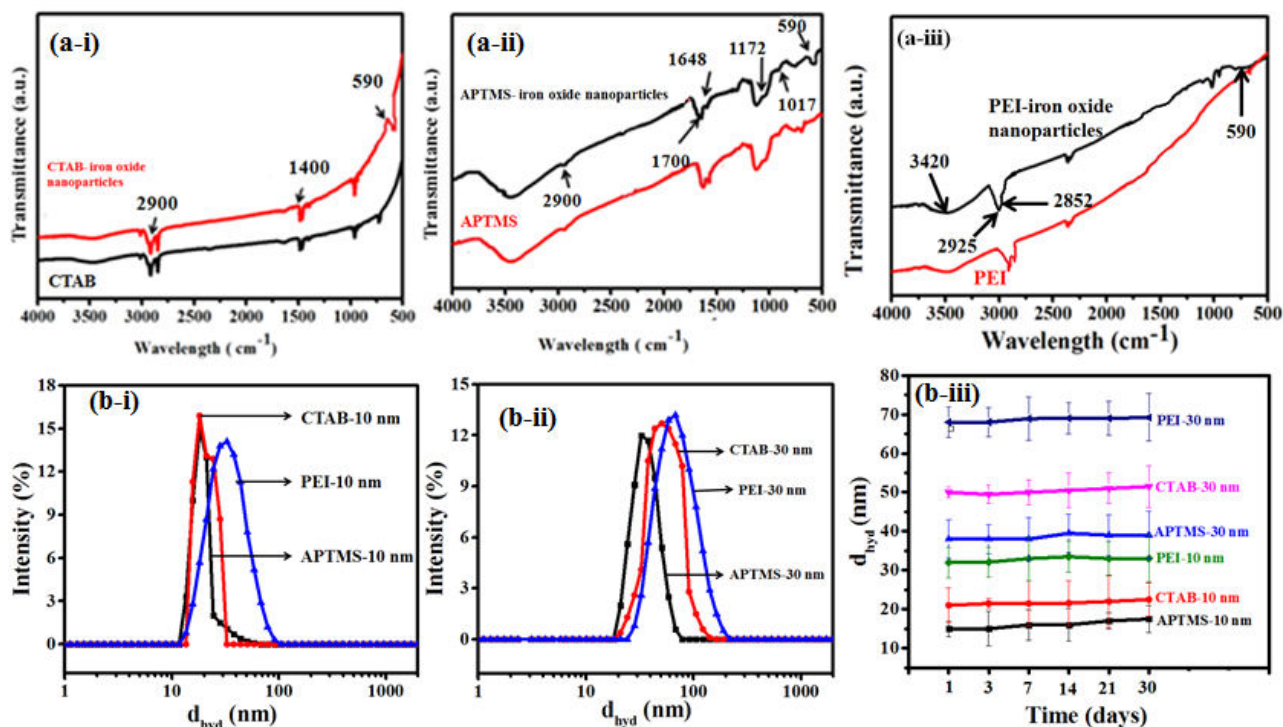


Fig. 3.2: Hydrophilic phase transfer of Fe₃O₄ nanoparticle (a-i) FTIR plot for CTAB coated Fe₃O₄ nanoparticles (a-ii) FTIR plot for APTMS capped Fe₃O₄ nanoparticles (a-iii) FTIR plot for PEI coated Fe₃O₄ nanoparticles (b-i) Average hydrodynamic radius of CTAB, APTMS and PEI coated 10 nm SPIONs (b-ii) Average hydrodynamic radius of CTAB, APTMS and PEI coated 30 nm FIONs. Inset shows the 30 nm FIONs individually coated with APTMS and the stable APTMS-FIONs solution (b-iii) stability of hydrophilic Fe₃O₄ nanoparticles over a period of 1 month.

Cell viability studies of Fe₃O₄ nanoparticles of different sizes

Fig. 3.3 shows the histogram of cell viability studies of 10 nm SPIONs and 30 nm FIONs. It is obvious from the Fig. 3.3(a) and 3.3(b) that there is no much difference in the cell viability between 10 nm and 30 nm Fe₃O₄ nanoparticles. While the 10 nm SPIONs show a viability of 99.4 % 30 nm FIONs show a viability of 99 %. There are more live cells in Q4 in both the histograms. While Q1 of Fig. 3.3(a) has almost no cells, Fig. 3.3(b) shows cells in Q1 and Q2, indicating that cells are starting to enter into late apoptosis and necrosis stage. This shows that, irrespective of the surface modifying agent used, the optimum size of Fe₃O₄ nanoparticles used for biomedical applications is between 10-30 nm. This is also the optimum size for magnetic hyperthermia applications, as Fe₃O₄ nanoparticles lesser than 10 nm, do not have strong heating characteristics and Fe₃O₄ nanoparticles bigger than a core size 30 nm might pose cell cytotoxicity and later difficulty in excretion from the biosystem.

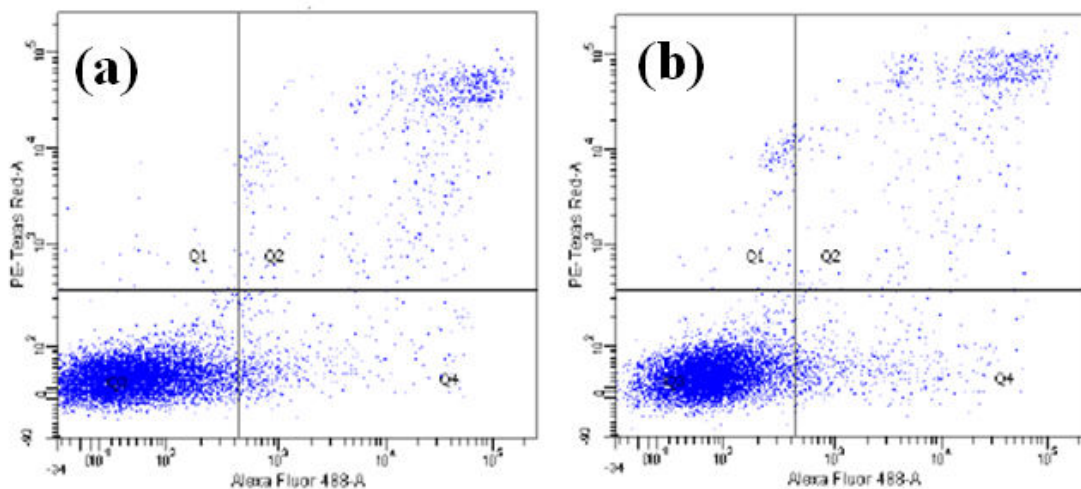


Fig. 3.3: Cell viability studies of Fe₃O₄ nanoparticles of different sizes a) 10 nm SPIONs- 99.4% viability b) 30 nm FIONs- 98% viability.

Magnetic hyperthermia of Fe₃O₄ nanoparticles of different sizes

As expected, the SAR value of the 30 nm Fe₃O₄ nanoparticles (FIONs) is higher than that of 10 nm Fe₃O₄ nanoparticles (SPIONs) irrespective of the surface modifying agent used, due to their higher magnetization. But the SAR value plot in Fig. 3.4 indicates that APTMS capped Fe₃O₄ nanoparticles shows slightly higher SAR value, this might be because of the smaller chain length of the same. The SAR values for APTMS capped 10 nm and 30 nm Fe₃O₄ nanoparticles are 510 W/g and 1790 W/g respectively. The SAR values for CTAB coated 10 nm and 30 nm Fe₃O₄ nanoparticles are 300 W/g and 1725 W/g respectively and for PEI coated 10 nm and 30 nm Fe₃O₄ nanoparticles are 285 W/g and 1685 W/g respectively. The inset figure shows that the temperature raise (ΔT) for 10 nm

Fe₃O₄ nanoparticles is only around 1.5°C and 30 nm Fe₃O₄ nanoparticles is 4.8°C respectively for a 3 minute exposure to 600 Oe field.

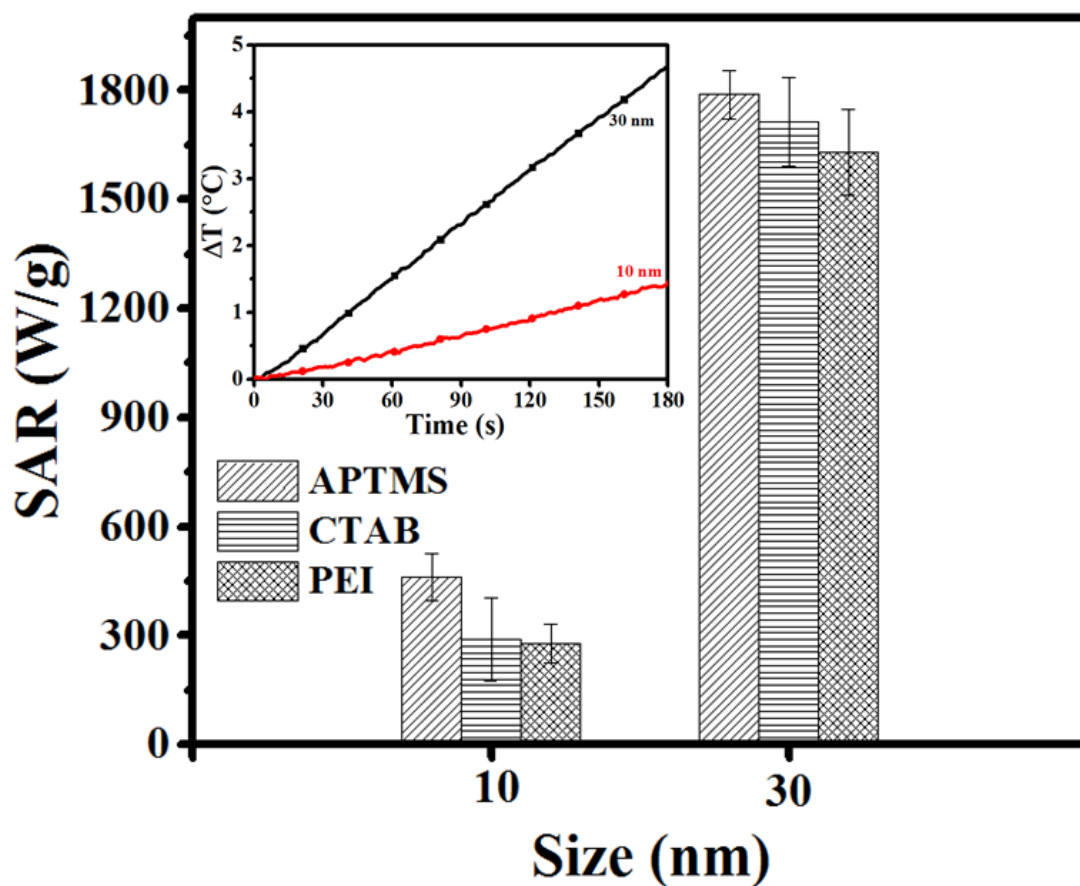


Fig. 3.4: SAR value comparison between hydrophilic Fe₃O₄ nanoparticles. Inset image shows the temperature raise comparison between 10 nm and 30 nm Fe₃O₄ nanoparticles for 3 minutes at 600 Oe.

3.3.2 Fe₃O₄ nanoparticles of different shapes

Synthesis and hydrophilic phase transfer of Fe₃O₄ nanoparticles of different shapes

We have synthesized 20 nm Fe₃O₄ nanoparticles of spherical, hexagonal and tetragonal geometry respectively. Fig. 3.5(a) shows the TEM image of the as-synthesized hydrophobic oleic acid capped Fe₃O₄ nanoparticles of different shapes. It is evident from the Fig. 3.5(a-i) and Fig. 3.5(a-ii) that the Fe₃O₄ nanoparticles of spherical and hexagonal shapes respectively were monodisperse with uniform size distribution, while from Fig. 3.5(a-iii) the nanotetragons were not uniformly distributed in terms of size and shape. We find the overall average size and shape of nanotetragon is 20 nm. The inset image shows the SAED corresponding to (111), (220), (311), (400), (422), (511) and (440) and confirms the crystal structure of the samples. The saturation magnetization (M_s) value of the as-synthesized nanotetragon was higher than that of nanosphere and nanohexagon as shown in Fig. 3.5(b). This might be because of the non-uniform size and shape distribution. Fig. 3.5(c) shows that the particles were monocrystalline and pure. This was measured using X-Ray Diffractometer (XRD, Bruker D8 Advanced Diffractometer System with Cu K α (1.5418 Å) source. The diffraction peaks can be indexed as cubic spinel Fe₃O₄ (JCPDS no.19-0629), corresponding to (220), (311), (400), (422), (511) and (440).

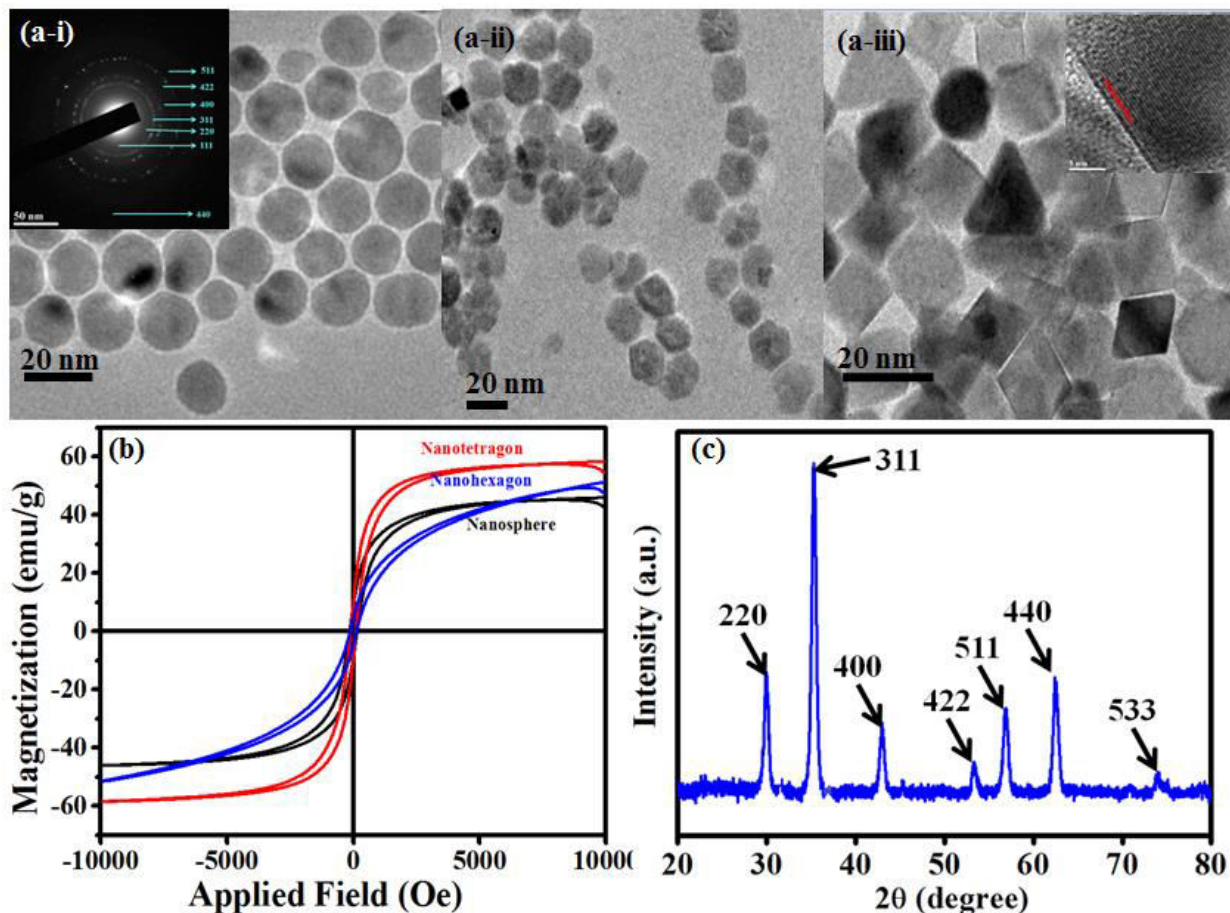


Fig. 3.5: Characterization of as-synthesized 20 nm Fe₃O₄ nanoparticles of different shapes (a-i) TEM image of nanospheres (a-ii) TEM image of nanohexagons (a-iii) TEM image of nanotetragons (a-ii) TEM image of nanohexagons (b) saturation magnetization (Ms) of Fe₃O₄ nanoparticles of different shapes (b) XRD plots of 20 nm Fe₃O₄ nanoparticles.

The hydrophobic as-synthesized Fe₃O₄ nanoparticles were surface modified to hydrophilic phase using (3-Aminopropyl) trimethoxysilane (APTMS) as our previous studies showed better stability and reduced average hydrodynamic radius for the same, with improved SAR value. Fig. 3.6 shows the average

hydrodynamic radius of nanosphere is 28 ± 2 nm, nanohehexagon is 36 ± 2 nm and nanotetragon 52 ± 2 nm is respectively.

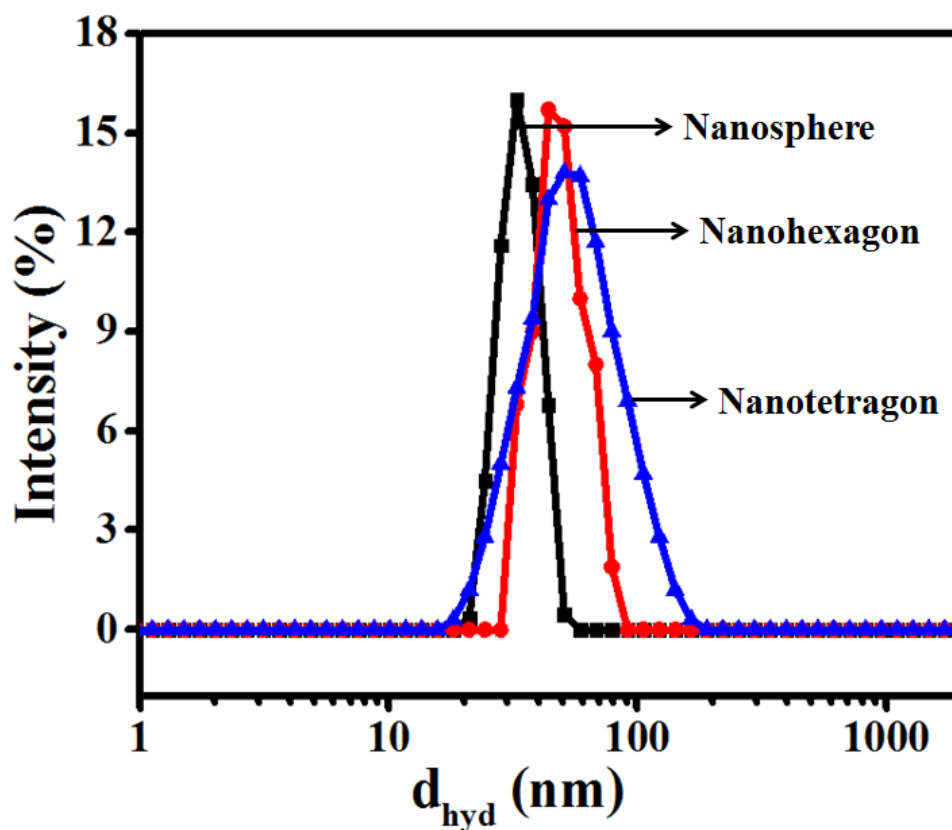


Fig. 3.6: Average hydrodynamic radius of Fe₃O₄ nanoparticles of different shapes.

Magnetic hyperthermia of Fe₃O₄ nanoparticles of different shapes

Overall the Fe₃O₄ nanoparticles showed higher SAR value than 10 nm particles in the previous section. This is because as the size increases the magnetization increases and thus the SAR value. Fig. 3.7 shows that nanotetragons have a higher

SAR value of 1865 W/g almost equivalent to that of 30 nm Fe₃O₄ nanoparticles from previous section. This is because of their non-uniformity leading to high magnetization. The nanospheres and nanohexagons have a SAR value of 910 W/g and 1285 W/g respectively, which are in the optimum range to be used for clinical applications.

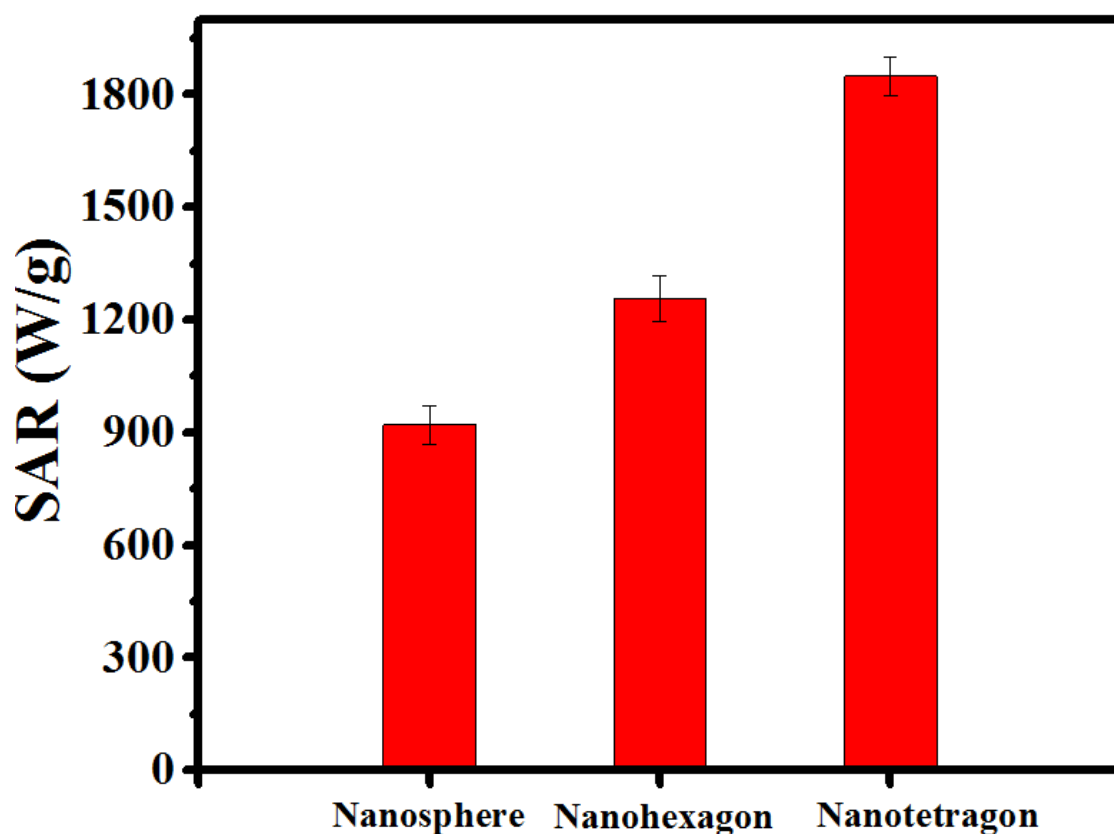


Fig. 3.7: SAR value of Fe₃O₄ nanoparticles of different shapes.

3.3.3 Fe₃O₄ nanoparticles of different composition- MetalFe₂O₄ (CoFe₂O₄, NiFe₂O₄) nanoparticles

Synthesis and hydrophilic phase transfer of MetalFe₂O₄ (Co Fe₂O₄, NiFe₂O₄) nanoparticles

Fig. 3.8 shows the TEM image of the as-synthesized hydrophobic nanoparticles of varied composition. For comparison sake we have synthesized 15 nm cubic Fe₃O₄ nanoparticles as shown in Fig. 3.8(a-i). The inset image shows the High Resolution TEM (HRTEM) of Fe₃O₄ nanoparticles. Fig. 3.8(a-ii) shows the SAED pattern corresponding to (111), (220), (311), (400), (422), (440) and (511). Fig. 3.8(b-i) shows the TEM image of CoFe₂O₄. The average size of the particles is 15 nm as seen from the TEM. The inset figure shows the HRTEM image of the same. Fig. 3.8(b-ii) shows the SAED pattern corresponding to (111), (220), (331), (222) and (422). Fig. 3.8(c-i) shows the TEM image of NiFe₂O₄. The average size of the particles is 150 nm as seen from the TEM. Fig. 3.8(c-ii) shows the SAED pattern corresponding to (111), (311), (400) and (422). The NiFe₂O₄ particles were almost 10 times bigger than the other two but since this section focuses on the composition and magnetization to anisotropy arising from composition, we used the NiFe₂O₄ particles for our studies. As seen from Fig. 3.8(d) the Fe₃O₄ nanoparticles have higher magnetization of 55 emu/g when compared to 52 emu/g of CoFe₂O₄ and 40 emu/g of NiFe₂O₄. The hysteresis loop

of CoFe_2O_4 bigger than the other two compositions. Therefore it has better heating characteristics than the other compositions.

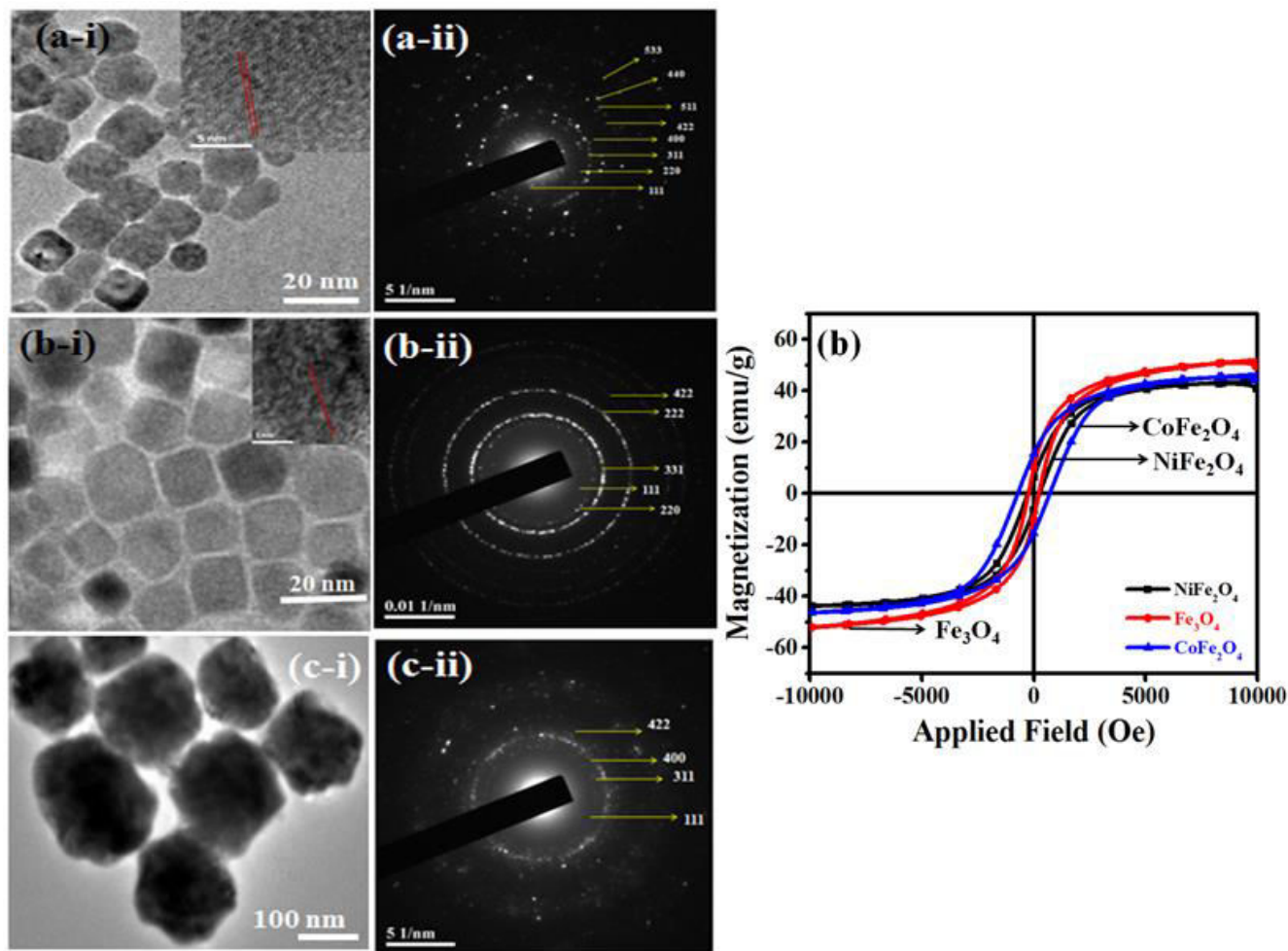


Fig. 3.8: Characterization of as-synthesized $\text{MetalFe}_2\text{O}_4$ nanoparticles of different compositions (a-i) TEM image of 15 nm Fe_3O_4 nanoparticles (a-ii) SAED pattern of Fe_3O_4 nanoparticles (b-i) TEM image of 15 nm CoFe_2O_4 nanoparticles (b-ii) SAED pattern of CoFe_2O_4 nanoparticles (c-i) TEM image of 150 nm NiFe_2O_4 nanoparticles (c-ii) SAED pattern of NiFe_2O_4 nanoparticles (b) saturation magnetization (Ms) of $\text{MetalFe}_2\text{O}_4$ nanoparticles of different compositions.

The particles were made hydrophilic by capping the same with APTMS. The average hydrodynamic radius of hydrophilic Fe_3O_4 nanoparticles is 21 ± 2 nm. CoFe_2O_4 nanoparticles is 25 ± 2 nm and NiFe_2O_4 nanoparticles is 170 ± 2 nm as seen in Fig. 9.

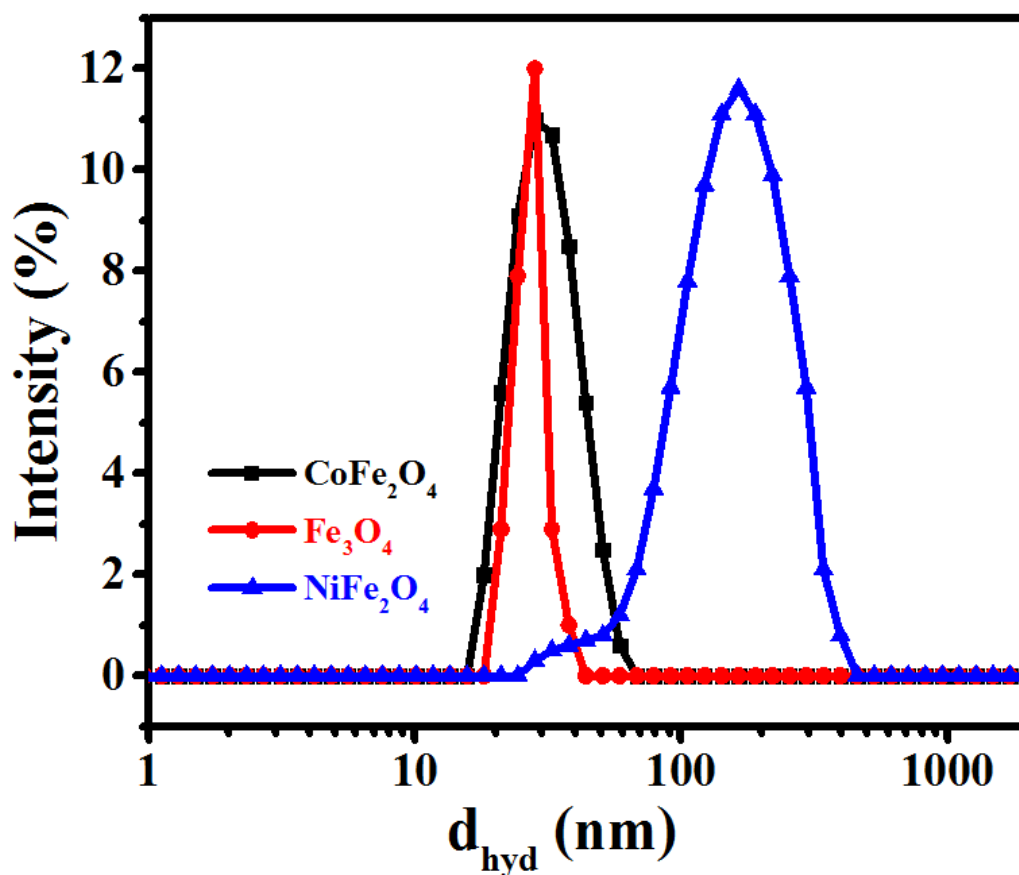


Fig. 3.9: Average hydrodynamic radius of hydrophilic $\text{MetalFe}_2\text{O}_4$ nanoparticles of different compositions.

Magnetic hyperthermia of MetalFe₂O₄ (CoFe₂O₄, NiFe₂O₄) nanoparticles

The SAR value of the nanoparticles with varied composition is shown in Fig. 3.10. CoFe₂O₄ nanoparticles of size 15 nm have a very high SAR value of 885 W/g when compared to 625 W/g of 15 nm Fe₃O₄ nanoparticles. NiFe₂O₄ nanoparticles have a low SAR value of 575 W/g. This is due to various factors like, bigger size and lower magnetization. It is widely considered that as the size of the Fe₃O₄ nanoparticles increases over an optimum size of 50 nm, the magnetization decreases. [165]. Also NiFe₂O₄ nanoparticles are widely considered to decrease heating efficiency than its counterparts discussed in this section [166, 167]. CoFe₂O₄ nanoparticles are also biologically safe to be used for clinical applications [168]. The inset figure shows that the temperature raise (ΔT) for CoFe₂O₄ nanoparticles is 2.8°C, Fe₃O₄ nanoparticles is 2.5°C and NiFe₂O₄ nanoparticles is 3.2°C respectively.

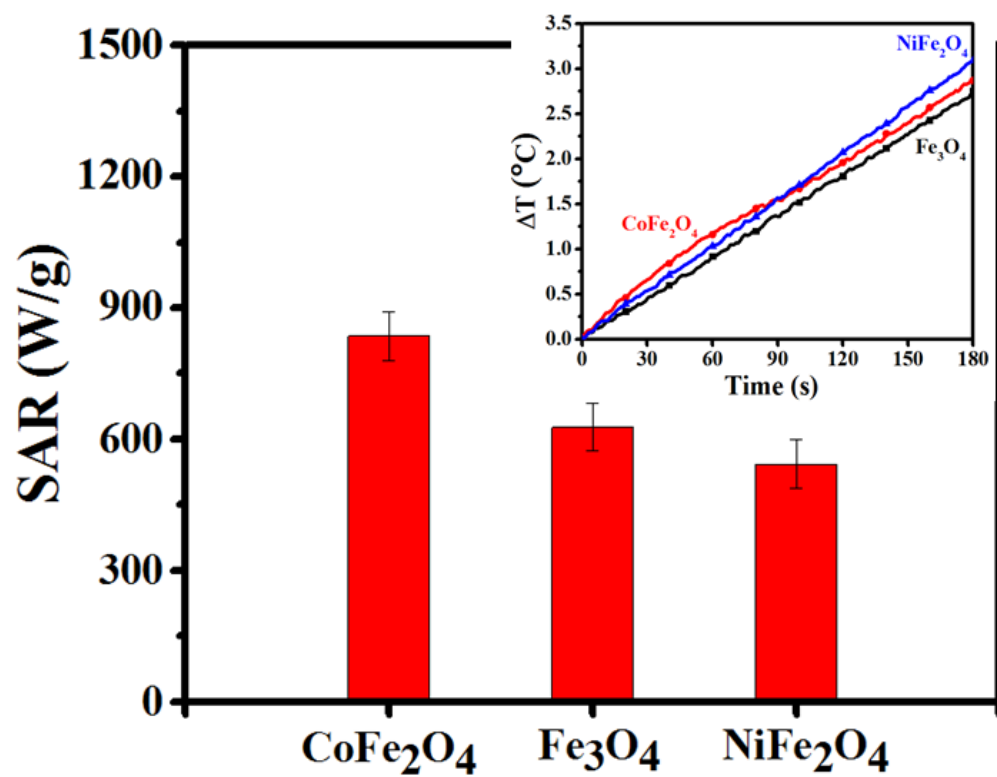


Fig. 3.10: SAR value of MFe_2O_4 nanoparticles of different composition. Inset figure shows the temperature raise of the same.

3.3.4 Combinatorial approach to enhance the biocompatibility and magnetic hyperthermia performance

The hydrophilic 10 nm superparamagnetic iron oxide nanoparticles (SPIONs) and 30 nm ferrimagnetic iron oxide nanoparticles coated with CTAB and APTMS were used for our studies to enhance biocompatibility and heating efficiency combinatorially.

Biocompatibility of BSA- Fe₃O₄ nanoparticles of different sizes

It is also evident Fig. 3.11(a-i) and (a-ii) that there is no peak observed in the surface modified (hydrophilic) Fe₃O₄ nanoparticles, viz, CTAB- Fe₃O₄ nanoparticles and APTMS- Fe₃O₄ nanoparticles. The characteristic peak of BSA is evident at 280 nm from Fig. 3.11(a-iii). The blue-shift in the UV-Vis spectrum shown in Fig. 3.11(a-iv) and 3.11(a-v) proves that the BSA is conjugated to the hydrophilic Fe₃O₄ nanoparticles and not merely present in the solution. The disturbances in the polypeptide environment within the BSA due to conjugation of the same to the surface modified Fe₃O₄ nanoparticles system is the reason behind the blue-shift. The Fig. 3.11(b) shows the zeta potential comparison of the BSA conjugated samples and non-conjugated samples. The reduction in surface charge after conjugating with BSA proves that BSA was conjugated with the surface modified Fe₃O₄ nanoparticles, as the anionic BSA reduces the

zeta potential of the system. Fig. 3.11(c) show the average hydrodynamic radius of BSA-CTAB-SPIONs to be 40 nm, BSA-CTAB-FIONs to be 80 nm, BSA-APTMS-SPIONs is 30 nm and BSA-APTMS-FIONs is 70 nm respectively. From the inset, it is evident that the FIONs are individually conjugated by the BSA and are well separated so as to prevent aggregation. The stability of the BSA conjugated iron oxide nanoparticles was enhanced when compared to the Fe₃O₄ nanoparticles without BSA conjugation, irrespective of the method of conjugation. This is evident from the DLS plot over a period of one month in Fig. 3.11(d). Thus the average hydrodynamic radius of BSA-SPIONs and BSA-FIONs is around 35±4 nm and 75±4 nm respectively. The size range is narrower and is more stable than albumin conjugated SPIONS reported in previous studies.

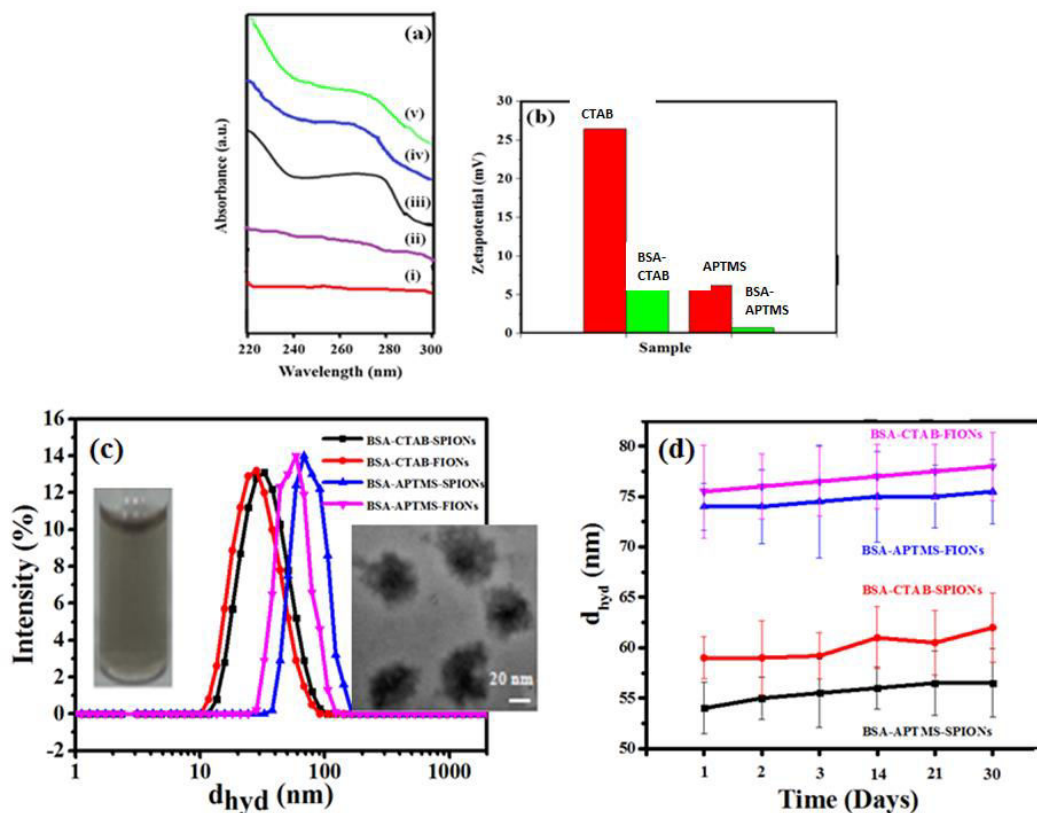


Fig. 3.11: Biocompatible Fe_3O_4 nanoparticles (a) UV-Visible spectrum of (i) CTAB- Fe_3O_4 nanoparticles (ii) APTMS- Fe_3O_4 nanoparticles (iii) characteristic peak of BSA at 280 nm (iv) blue-shift due to BSA-CTAB- Fe_3O_4 nanoparticles (v) blue-shift due to BSA-APTMS- Fe_3O_4 nanoparticles (b) Zeta potential comparison of hydrophilic and biocompatible Fe_3O_4 nanoparticles (c) Average hydrodynamic radius of BSA conjugated CTAB/APTMS coated SPIONs/FIONs. Inset shows the 30 nm FIONs individually conjugated with BSA and the stable BSA-APTMS-FIONs solution (d) stability of biocompatible Fe_3O_4 nanoparticles over a period of 1 month.

Haemolytic studies of BSA-Fe₃O₄ nanoparticles

The photos in Fig. 3.12(a)-(e) show the effect of test samples on erythrocytes. Fig. 3.12(a) shows aggregation of ruptured erythrocytes due to as-synthesized Fe₃O₄ nanoparticles -SPIONs and FIONs. Due to the high oxidative stress, haemoglobin was released into the solution as the ruptured erythrocytes settled down as debris. Fig. 3.12(b) and 3.12(d) show the haemolysis due to hydrophilic Fe₃O₄ nanoparticles-CTAB-Fe₃O₄ nanoparticles and APTMS-Fe₃O₄ nanoparticles respectively. Mild haemolysis was observed in this case. The Fig. 3.12(c) and 3.12(e) of BSA-CTAB-Fe₃O₄ nanoparticles and BSA-APTMS-Fe₃O₄ nanoparticles respectively show that there was a significant reduction in haemolysis after conjugating with BSA. There was almost no cell debris and therefore no haemoglobin leakage in the BSA conjugated test samples, which implies that cell lysis was almost nil in the same. This is the reason for the reduced absorbance at 540 nm. Fig. 3.12(f) graphically depicts the general mechanism of haemolysis in both as-synthesized and BSA conjugated iron oxide nanoparticles. The haemolytic studies were conducted as per the ASTM F756-00 standards. It is evident from Fig. 3.12(g) and 3.12(h) that the haemolytic index of the as-synthesized, hydrophobic SPIONs is 57% and that of FIONs is 78 %, both well above the 5 % standard, showing that they are highly haemolytic in nature. From Fig. 3.12(g) it is evident that the haemolytic index of CTAB-SPIONs is 28% when compared to 2.5 % of BSA-CTAB-SPIONs and

CTAB-FIONs is 38% when compared to 2.2 % of BSA-CTAB-FIONs. Fig. 3.12(h) shows that the haemolytic index of APTMS-SPIONs is 17 % and that of BSA-APTMS-SPIONs is 1.2 %. It also shows that the haemolytic index of APTMS-FIONs is 28% and that of BSA-APTMS-FIONs is 1.3%. This shows that BSA conjugation makes the Fe₃O₄ nanoparticles almost non-haemolytic nature, as the haemolytic index is $\leq 2\%$, irrespective of the method of conjugation. Surface modification by APTMS is non-haemolytic in nature, when compared to CTAB. This may be because the covalent bonding is stronger than physical adsorption and hence the particles are well conjugated with BSA. It is also observed that BSA-FIONs have biocompatibility similar to that of BSA-SPIONs, even though their size is bigger. Better biocompatibility for a bigger size is an added advantage, as FIONs have better magnetic properties to be used in magnetic hyperthermia experiments.

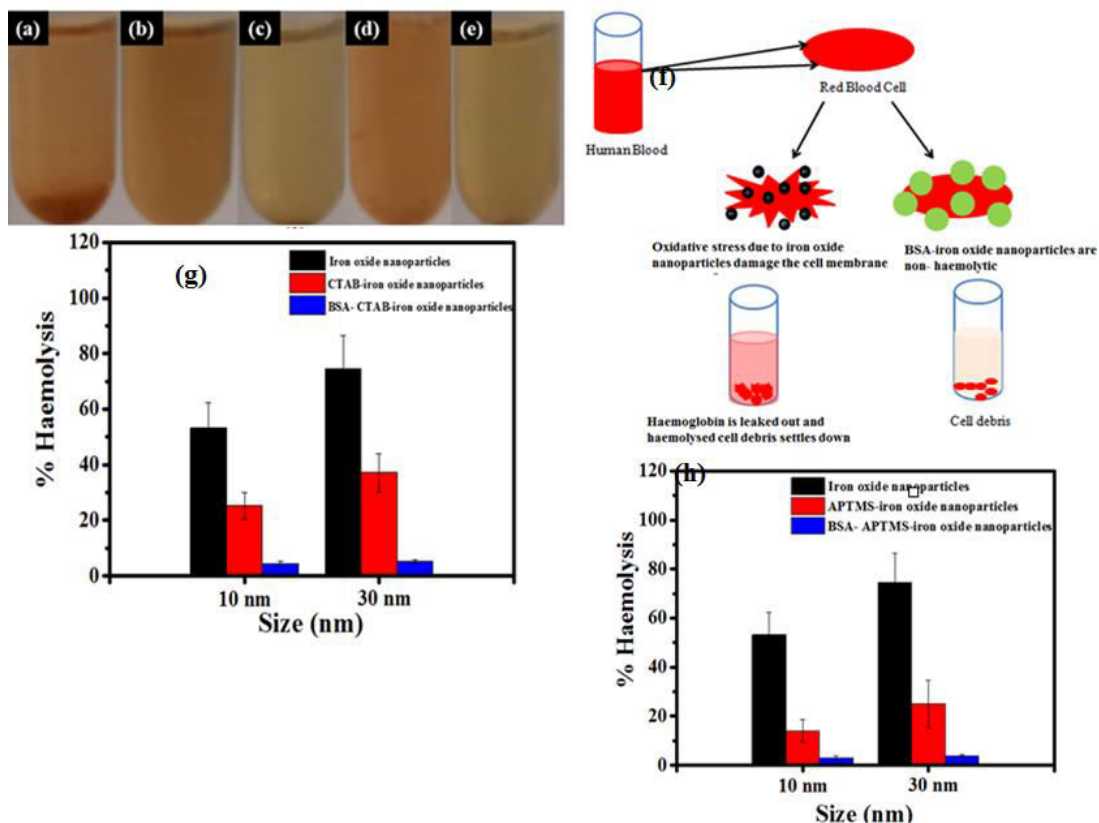


Fig. 3.12: Haemolytic studies. Haemolytic effect of test samples (a) as-synthesized Fe₃O₄ nanoparticles (b) CTAB-Fe₃O₄ nanoparticles (c) BSA-CTAB-Fe₃O₄ nanoparticles (d) APTMS-Fe₃O₄ nanoparticles (e) BSA-APTMS-Fe₃O₄ nanoparticles (f) Mechanism of haemolysis (g) Haemolytic index of the BSA conjugated CTAB- Fe₃O₄ nanoparticles (h) Haemolytic index of the BSA conjugated CTAB- Fe₃O₄ nanoparticles.

Cell viability studies of BSA-Fe₃O₄ nanoparticles

Since APTMS-FIONs and BSA-APTMS-FIONs showed reduced or nil haemolysis respectively, we performed cell viability studies using the same. The BSA conjugated APTMS-FIONs show a normalized viability range of upto 120% (for 12.5 µg/mL and 25 µg/mL), when compared to the normalized

100% of APTMS-FIONs (for 12.5 µg/mL and 25 µg/mL). Previous studies also show that addition of BSA conjugated SPIONs, without the external application of magnetic field show no harmful effect on cell viability [163]. It is also evident from Fig. 3.13(a) that the cell viability decreases as the concentration of FIONs in the test sample increases, as in 50 µg/mL and 100 µg/mL. Fig. 3.13(b) and 3.4.4(c) shows the histogram of BHK cells after incubation with 100 µg/mL of APTMS-FIONs and BSA-APTMS-FIONs respectively. The cell viability of APTMS-FIONs is 98 % and BSA-APTMS-FIONs is 99.5% as seen from the histograms. Though statistically the difference seems to be very insignificant, it is to be noted that Fig. 3.13(b) has more cells in late apoptosis (Q2) and a few cells in necrosis (Q1) stage. Fig. 3.13(c) shows almost no cells Q1 and Q2 showing that BSA conjugation significantly reduces the cytotoxicity of FIONs. The inset confocal images of Fig. 3.13(b) and 3.13(c) conform the same. This shows that BSA conjugated FIONs exhibit less or no cytotoxicity to healthy BHK cells.

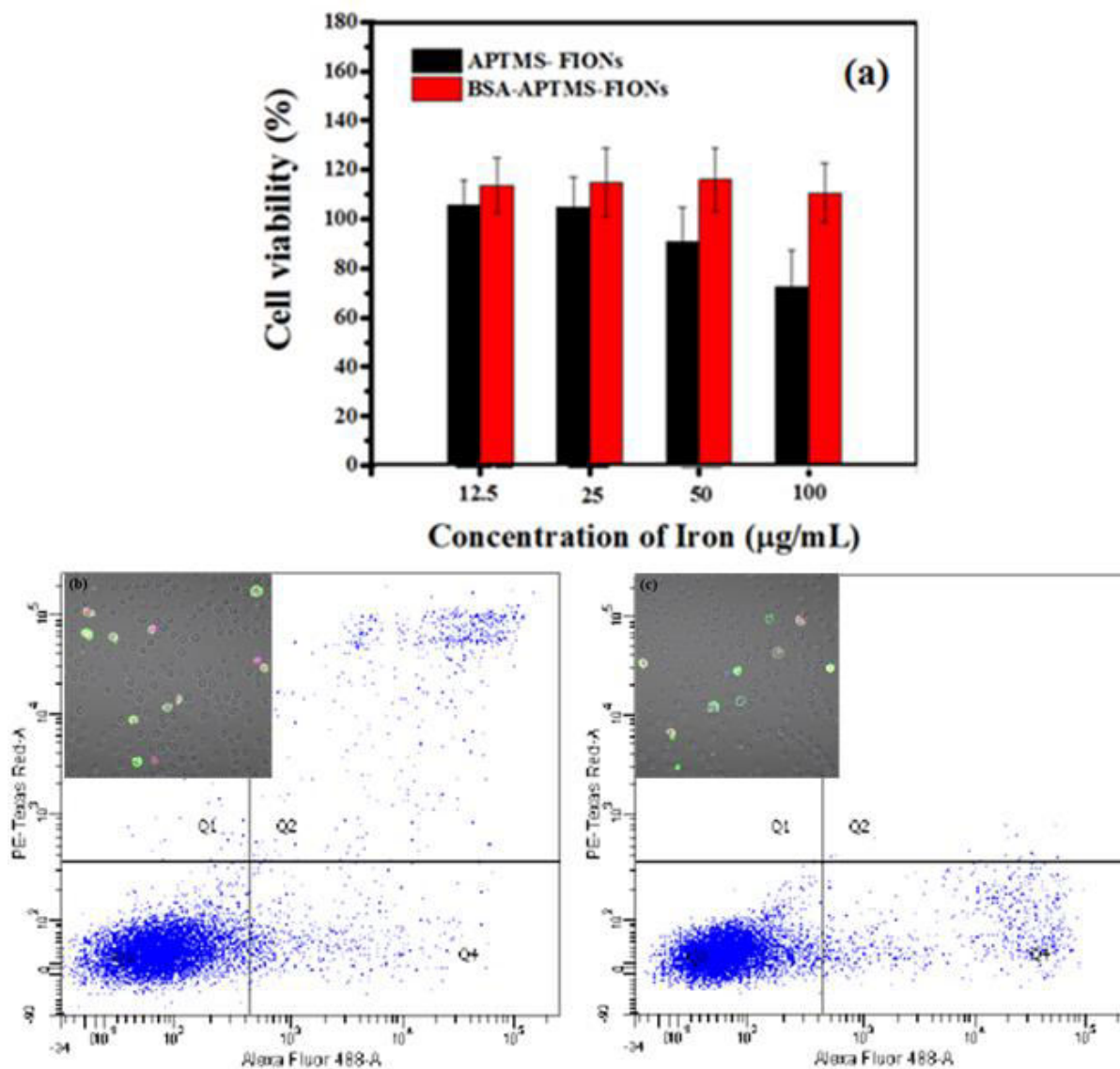


Fig. 3.13: Cell viability studies (a) The BSA conjugated APTMS-FIONs exhibit higher percentage of cell viability than the non-conjugated FIONs (b) APTMS-FIONs are 98 % viable (c) BSA-APTMS-FIONs are almost 99.5 %. Inset figures shows the confocal images of the same.

From the haemolytic studies and the cell viability studies, it is evident that BSA conjugation improves the biocompatibility of the iron oxide nanoparticles system. BSA-FIONs show better results when compared BSA-SPIONs or as-synthesized particles or the hydrophilic particles. Thus the first requisite for an efficient magnetic hyperthermia system is met out.

Magnetic hyperthermia experiment of BSA-Fe₃O₄ nanoparticles

The heating efficiency of the hydrophilic iron oxide nanoparticles and BSA conjugated iron oxide nanoparticles were studied by the magnetic hyperthermia experiments. Fig. 3.14(a) shows the temperature raise comparison of the CTAB- Fe₃O₄ nanoparticles and BSA- CTAB- Fe₃O₄ nanoparticles. From Fig. 3.14(b) it is evident that the SAR value of CTAB-SPIONs is 270 W/g and that of BSA-CTAB-SPIONs is 540 W/g; CTAB- FIONs is 1750 W/g and that of BSA-CTAB-FIONs is 2200 W/g. Fig. 3.14(c) shows the temperature raise comparison of APTMS-Fe₃O₄ nanoparticles and BSA-APTMS- Fe₃O₄ nanoparticles. A temperature raise of around 11°C is observed in BSA-FIONs, when compared to the 3°C raise shown by BSA-SPIONs in 3 minutes. Fig. 3.14(d) shows that the SAR value of APTMS-SPIONs is 480 W/g when compared to 520 W/g of BSA-APTMS-SPIONs; APTMS-FIONs is 1700 W/g and BSA-APTMS-FIONs is 2300 W/g. It is observed that the covalent bond method using APTMS shows slightly better efficiency irrespective of the size of

the particles due to the strong bonding between the hydrophilic iron oxide particles and the BSA and hence improved colloidal stability. It is evident that FIONs of 30 nm size show higher SAR value than SPIONs of 10 nm size, due to their higher saturation magnetization.

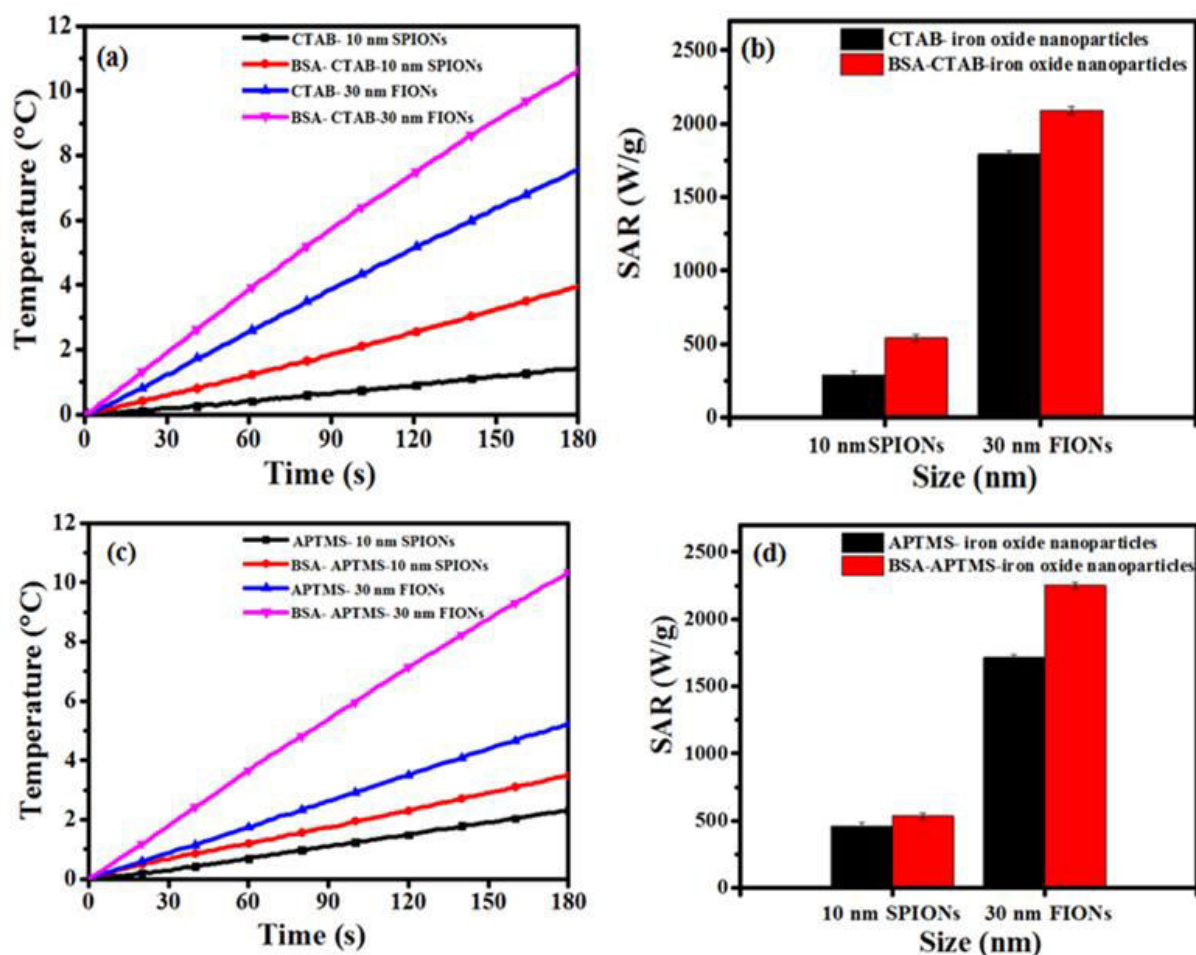


Fig. 3.14: Heating characteristics a) Temperature raise comparison between BSA-CTAB-Fe₃O₄ nanoparticles and CTAB-Fe₃O₄ nanoparticles b) SAR value comparison between BSA-CTAB-Fe₃O₄ nanoparticles and CTAB-Fe₃O₄ nanoparticles c) Temperature raise comparison between BSA-APTMS-Fe₃O₄ nanoparticles and APTMS-Fe₃O₄ nanoparticles d) SAR value comparison between BSA-APTMS-Fe₃O₄ nanoparticles and APTMS-Fe₃O₄ nanoparticles.

The SAR value plots show that, irrespective of the method of conjugation, BSA improves the heating efficiency of the system. While here we report the phenomenon, we are to further investigate the possible reasons behind this interesting phenomenon. It is stated elsewhere that isotropic clusters of BSA are formed under AC magnetic field [169]. Isotropic clusters might have possibly prevented the fibrous aggregation of iron oxide nanoparticles under the AC magnetic field. In general, fibrous aggregation increases the critical size of the nanoparticles in a solution and hence decreases the specific heat of the system. It is well reported that aggregation of nanoparticles decreases the SAR value significantly [170, 171]. Prevention of aggregation by BSA conjugation might have thus enhanced the SAR value of the system. As reported by Samanta et al in similar studies with SPIONs, this phenomenon could also be attributed to the increased colloidal stability of the BSA conjugated iron oxide nanoparticles. The BSA conjugated iron oxide nanoparticles were well separated and well suspended, even under applied magnetic field. Whereas the hydrophilic iron oxide nanoparticles without BSA conjugation aggregate in the presence of magnetic field. This interesting phenomenon of improved heating efficiency, relating to the colloidal stability imparted by the BSA to the iron oxide nanoparticles will be studied further. BSA conjugation over FIONs shows better SAR value than the BSA-SPIONS, due to the high saturation magnetization. Thus the second requisite for an efficient magnetic hyperthermia system is also well established.

As schematic overview of the enhancement of biocompatibility and heating efficiency, combinatorially using BSA conjugation is shown in Fig. 3.15

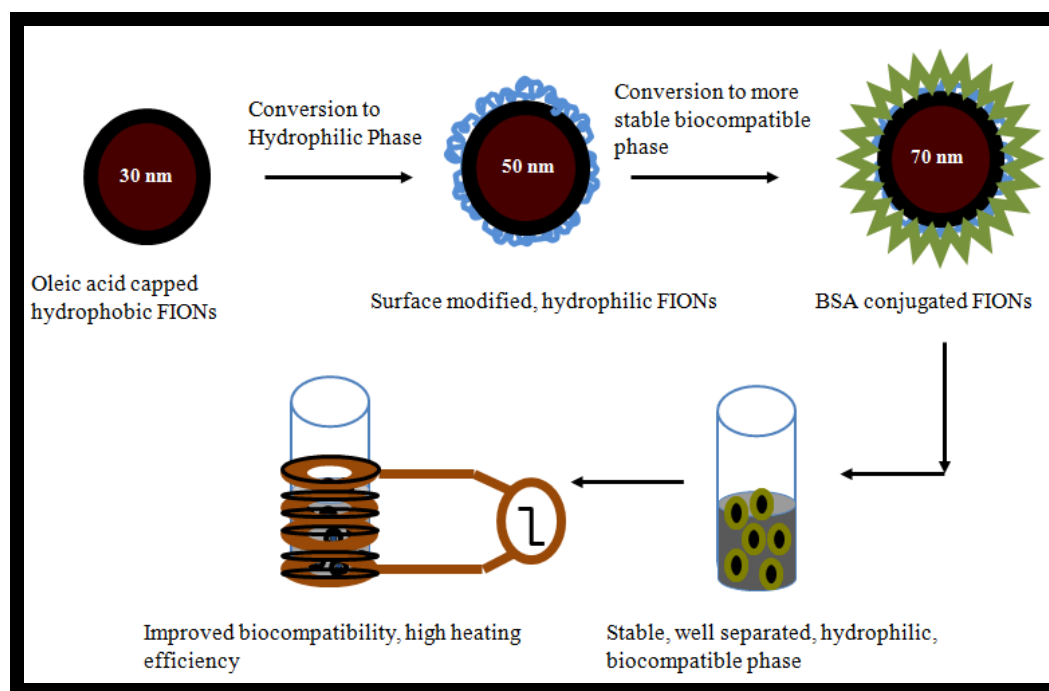


Fig. 3.15: Schematic overview of the BSA-FIONs to improve biocompatibility and heating efficiency.

Magnetic hyperthermia treatment of BSA-Fe₃O₄ nanoparticles on tissue

Since our results show that BSA-APTMS-FIONs can be potential candidates for a single combinatorial approach to enhance both the biocompatibility and heating efficiency. We studied the same on liver tissue. The AC magnetic field was adjusted so as to raise the temperature upto 45 °C. It is clearly evident from Fig. 3.16(a) that before the magnetic hyperthermia treatment, there is no tissue

damage, as indicated by blue nuclei of live cells of the tissue. Magnetic hyperthermia treatment causes apoptosis (green cells) and further necrosis (pink nuclei) as shown in Fig. 3.16(b)

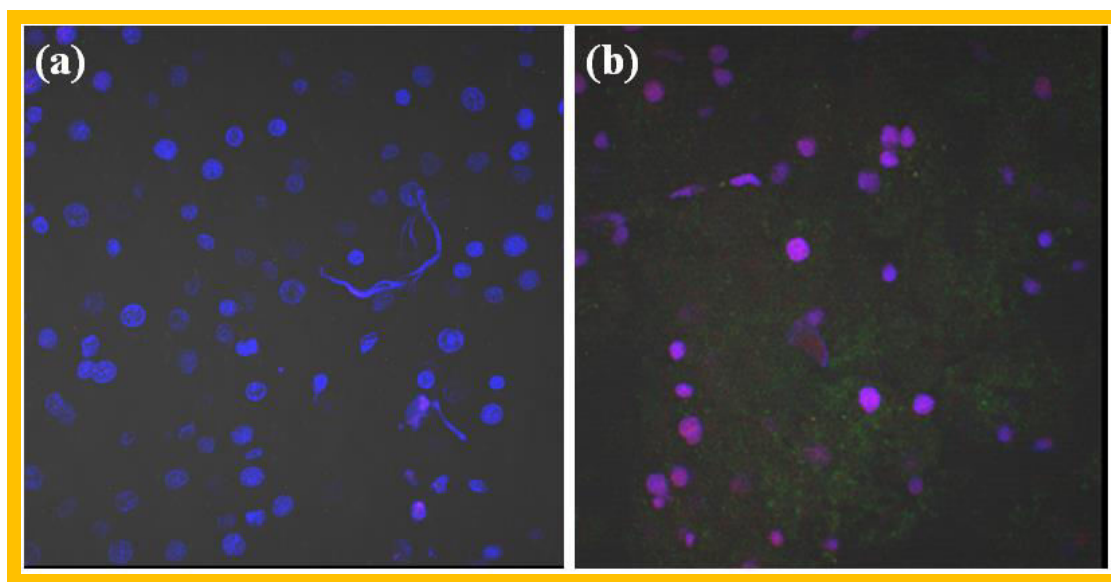


Fig. 3.16: Magnetic hyperthermia treatment on liver tissue (a) liver tissue before magnetic hyperthermia treatment (b) liver tissue after magnetic hyperthermia treatment with 0.1 mg/mL BSA-APTMS-FIONs and 600 Oe AC magnetic field to raise the temperature upto 45 °C.

3.4 Conclusion

Our preliminary work focuses on fabricating the optimum size Fe₃O₄ nanoparticles without compromising on the heating efficiency and biocompatibility. We find that due to their higher magnetization of 87 emu/g and hence a SAR value of almost 1700 W/g irrespective of the surface modifying

agent used and a very good cell viability of almost 99%, 30 nm Fe₃O₄ nanoparticles (FIONs) are promising candidates for magnetic hyperthermia.

Fe₃O₄ nanoparticles of size 20 nm and different shapes were fabricated. nanospheres were found to be uniform in size and shape distribution, though they have low heating efficiency. Spherical shape is widely considered to be lower in magnetization when compared to other shapes. The nanohexagons and nanotetragons fabricated gave a better SAR value of almost 1800 W/g, but the uniformity is under question. Therefore in this section we conclude nanospheres as better candidates due to their ease of synthesis and uniformity in size and shape.

Varying the composition of Fe₃O₄ nanoparticles by replacing the Fe²⁺ ions with Co²⁺/ Ni²⁺ increases the surface anisotropy, thus increasing the SAR value even at the superparamagnetic regime. Thus 15 nm CoFe₂O₄ nanoparticles have a very high SAR value of almost 885 w/g than Fe₃O₄ nanoparticles of same size. Thus CoFe₂O₄ nanoparticles can be considered as potential candidates for magnetic hyperthermia application owing to their better SAR value. Though the biosafety of CoFe₂O₄ nanoparticles might not be as comparable as Fe₃O₄ nanoparticles, future works can be directed towards improving the biocompatibility of CoFe₂O₄ nanoparticles.

We have studied the biocompatibility and heating characteristics of both BSA-SPIONS and BSA-FIONs. BSA conjugation was done by both physical adsorption and strong covalent amide bond formation. The haemolytic studies and cell viability studies discussed in this chapter confirm that the biocompatibility of the iron oxide nanoparticles increased after BSA conjugation. Particularly BSA-FIONs show better biocompatibility than that of BSA-SPIONS. The improved SAR value of the BSA conjugated iron oxide nanoparticles system is due to the enhanced colloidal stability and prevention of aggregation. Though the study of efficiency of the surface modifying agents used is beyond the scope of this chapter, we still report that BSA conjugation by covalent bonding using APTMS has better colloidal stability and hence better biocompatibility and heating efficiency, as BSA-APTMS-FIONs show better results than that of BSA-CTAB-FIONs. Also the higher magnetic saturation of FIONs lead to higher SAR value and hence better heating efficiency than SPIONS. We thus conclude that the two key challenges of a very good magnetic hyperthermia system-improved biocompatibility and heating enhancement were addressed through the fabrication of BSA-FIONs.

CHAPTER 4: Effects of Physiological Components and AC Magnetic Field on Magnetic Hyperthermia

4.1 Introduction

Our previous chapters discussed the effect of magnetic hyperthermia on biosystem. Just as magnetic nanoparticles influence the physiology, the physiological components also have a significant impact on the biosystem. The pre-requisites for an efficient magnetic hyperthermia system are multitude, ranging from applied AC magnetic field, frequency, size and material properties of magnetic nanoparticles time dependent temperature exposure etc [172, 173]. Among these factors, applied AC magnetic field of radiofrequency 100-1000 kHz plays a significant role in influencing the heating efficiency of magnetic nanoparticles [174, 175]. The heating efficiency of magnetic hyperthermia is measured in terms of specific absorption rate (SAR). The SAR value of the magnetic nanoparticles is also found to increase with the AC magnetic field [176, 177]. This raises serious concerns about biological safety under an applied AC magnetic field [178, 179]. In electrochemical therapy, under an applied electric field the chemical reactions between physiological ions causes cancer cell death due to change in chemical environment, pH and increase in temperature of the tumor site [180, 181]. Since physiological ions are found to be influenced by applied electric field, a better understanding of the effect of applied AC magnetic field of the magnetic hyperthermia system on the physiological ions is needed. Our previous studies have also indicated that surface modification of magnetic

nanoparticles using surfactants of different surface charges contribute to temperature raise in magnetic hyperthermia due to better colloidal stability [182, 183]. Though a systematic study on the effect of surface modification on magnetic hyperthermia is beyond the scope of this chapter, this further arises the question about contribution of surface charges or other physiological ions to heating efficiency.

This chapter discusses the effect of physiological components under an applied AC magnetic field on heating efficiency and biosafety of magnetic hyperthermia system. Our results show that under an applied AC magnetic field of 600 Oe and frequency of 360 kHz, while the physiological electrolytes/ions contribute significantly to the heating efficiency of superparamagnetic iron oxide nanoparticles (SPIONs), the plasma proteins and cellular components tend to retard the temperature raise. Even without SPIONs, under an applied AC magnetic field, physiological ions increase the temperature raise and physiological proteins and cells retard the same. We understand that while heating efficiency of a magnetic hyperthermia system is increased by the physiological ions, the proteins present in the biosystem tend to mask the adverse temperature raise and radiation effects, thus acting as biosafety agents. We further confirmed these results by treating healthy kidney and liver tissue to AC magnetic field of 600 Oe and frequency of 360 kHz, with and without SPIONs. The results show

that AC magnetic field alone, without SPIONs does not cause any damage to the tissue, as proteins and cells insulate the heat dissipation under the exposed radiation. To our best knowledge, no previous attempts have been reported to systematically study the possible contribution of physiological ions, proteins and cells to magnetic hyperthermia. It is important to study the effect of physiological components on magnetic nanoparticles and their contribution to temperature raise under an AC magnetic field. This helps to develop a magnetic hyperthermia system which is better in heating efficiency, without compromising on the biosafety.

4.2 Methods

Magnetic hyperthermia experiments with superparamagnetic iron oxide nanoparticles in various media

The hydrophilic SPIONs (0.1 mg/mL) were well suspended in water, 1xPBS, plasma (Sigma Aldrich), albumin solution, blood and other physiological fluids and used for our experiments. DLS measurements were made to confirm the size and stability of SPIONs in 1xPBS. Under an applied AC magnetic field of 600 Oe, frequency 360 kHz and exposure time of 3 minutes, the temperature raise (ΔT) of SPIONs in the above mentioned media was studied.

SAR is expressed as the heat released by the magnetic iron oxide nanoparticles under a magnetic field. The SAR value is calculated from the formula,

$$\text{SAR} = C_{\text{wat}} \frac{\Delta T}{\Delta t} * \frac{1}{C_{\text{Fe}}} (\text{Wg}^{-1})$$

Where, C_{wat} - specific heat of the medium (distilled water), 4.18 J /g/ °C; $\Delta T/\Delta t$ - The initial slope of the time-dependent temperature curve; C_{Fe} - concentration of ferric ions in the medium, 0.1mg/mL. The concentration of ferric ions in the samples was determined using ICP-OES analysis (Perkin-Elmer Dual view Optima 5300 DV ICPOES system). The individual contribution of various physiological components without superparamagnetic iron oxide nanoparticles, towards temperature raise was studied under an applied AC magnetic field of 600 Oe, frequency 360 kHz and exposure time of 3 minutes.

Magnetic hyperthermia experiments and imaging with cells and tissue

The MCF-7 cells suspended in 1xPBS were subjected to 0.1 mg/mL SPIONs and an applied AC magnetic field of 600 Oe (frequency 360 kHz), to bring a temperature raise (ΔT) of upto 42-45°C. The MCF-7 cells under AC magnetic field alone and after hyperthermia treatment were observed under confocal microscope (Olympus-FluoView, FV1000). The live MCF-7 cells were stained

green with AlexaFluor 488 (Invitrogen) and nuclei of dead cells were stained red by Propidium Iodide (PI-ThermoFischer Scientific).

The effect of application of AC magnetic field and the combination of AC magnetic field and 0.1 mg/mL SPIONs on healthy kidney and liver tissue were studied. The organs (kidney and liver) were treated with 0.1 mg/mL SPIONs and an applied AC magnetic field of 600 Oe (frequency 360 kHz), to bring a ΔT of upto 42°C-45°C. The healthy tissue before and after treatment were observed under confocal microscope (Olympus-FluoView, FV1000). Dyes NucBlue (ThermoFischer Scientific) to stain the total nuclei of cells, AlexaFluor (Invitrogen) to stain the apoptotic cells green and Propidium Iodide (PI-ThermoFischer Scientific) to stain the nucleus of dead cells red were used to qualitatively visualize the excised organ tissue. While the nuclei of the live cells are stained blue, the nuclei of completely dead cells (necrosis) appear pink. Briefly, to 1 mm² of the excised tissue, 2 drops of NucBlue, 2.5 μ L of AlexaFluor and 0.5 μ L of PI were added along with 100 μ L binding buffer and were incubated at room temperature for 15 minutes. The reaction was stopped by adding excess binding buffer and the samples were viewed under the confocal microscope. The images were later processed using the software IMARIS 8.0. Our preliminary studies are based on the qualitative observations of the stained cells/tissue morphology.

4.3 Results and Discussion

Synthesis of hydrophilic superparamagnetic iron oxide nanoparticles

The heating efficiency of SPIONs in various physiological media was studied and are discussed in this paper. We had synthesized the SPIONs to be used in our studies. The size of the monodisperse, close-packed SPIONs was confirmed by the TEM micrographs in Fig. 4.1(a). The SAED pattern from Fig. 4.1(b) confirms the cubic spinel of the as-synthesized Fe_3O_4 . The size of SPIONs was further confirmed from the XRD data using Scherrer's formula. The diffraction peaks from Fig. 4.1(c) can be indexed as cubic spinel Fe_3O_4 (JCPDSno.19-0629), corresponding to (220), (311), (400), (422), (511) and (440). Broad peaks indicate that the particles are smaller in size. The magnetization saturation of the as-synthesized SPIONs is found to be 45 emu/g as shown in Fig. 4.1(d). The hydrodynamic size of the CTAB-SPIONs was found to be 20 ± 2 nm as shown in Fig. 4.1(e).

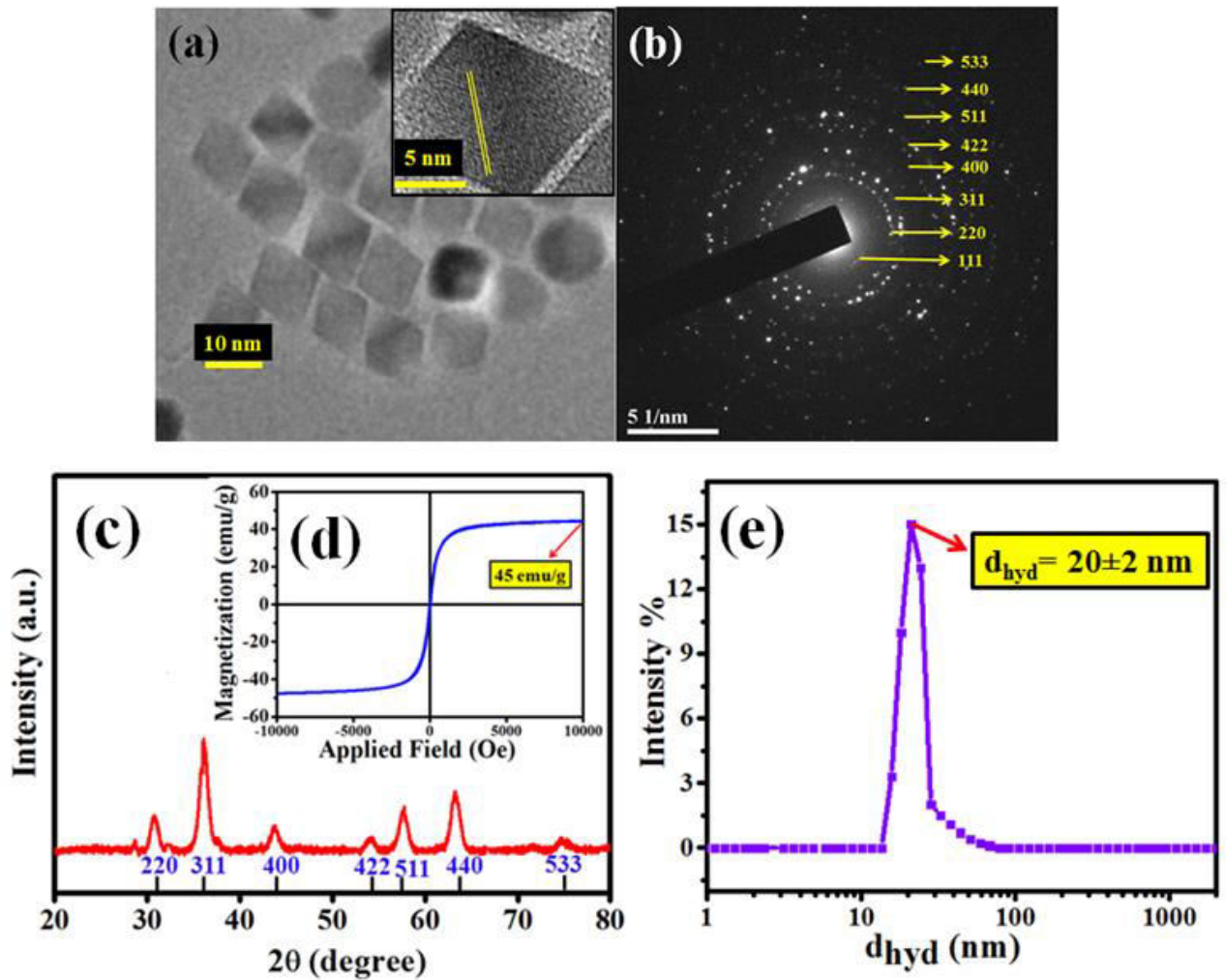


Fig. 4.1: (a) TEM image of the as-synthesized SPIONs. Inset image is the high resolution TEM micrograph showing lattice; (b) TEM selected area electron diffraction image (SAED) of the SPIONs (c) XRD plot (d) Magnetization of the SPIONs (e) Average hydrodynamic radius of SPIONs in water.

Heating efficiency of superparamagnetic iron oxide nanoparticles in physiological fluids

As discussed earlier, SPIONs are potential candidates for magnetic hyperthermia. However, most hyperthermia studies for SPIONs are carried out in de-ionized water. In this work, we have studied the hyperthermia effect of SPIONs in biological systems. The hydrophilic SPIONs were dispersed in de-ionized water and the temperature raise (ΔT) was recorded. PBS of 1x concentration is widely used for biological studies to mimic the physiological electrolytes. Hence the same was used in our studies to represent physiological electrolytes. We studied the temperature raise (ΔT) due to hydrophilic SPIONs dispersed in 1x PBS. Furthermore any biological system is made of physiological fluids along with proteins and cellular components (which are also largely made of proteins). Since clinical applications involve the injection of SPIONs in blood before reaching the target site, we had studied the temperature raise (ΔT) of hydrophilic SPIONs in liquid tissue-blood. As shown in Fig. 4.2, 0.1 mg/mL hydrophilic SPIONs in de-ionised water raises the temperature upto 2.8°C within 3 minutes, corresponding to a SAR value of 291 W/g (the value is well expected for SPIONs in water). In the second test, we dispersed 0.1 mg/mL SPIONs into 1xPBS. Temperature raise was around 8.5°C within 3 minutes, which corresponds to a SAR value of 750 W/g for 0.1 mg/mL SPIONs under the same conditions (600 Oe and 360 kHz).

The result has shown that 1xPBS as the medium of dispersion for SPIONs can increase hyperthermia effect significantly. In the third test, 0.1 mg/mL SPIONs were dispersed blood. The temperature raise was reduced to 2.6 °C, very similar to that when de-ionized water was used as the carrier.

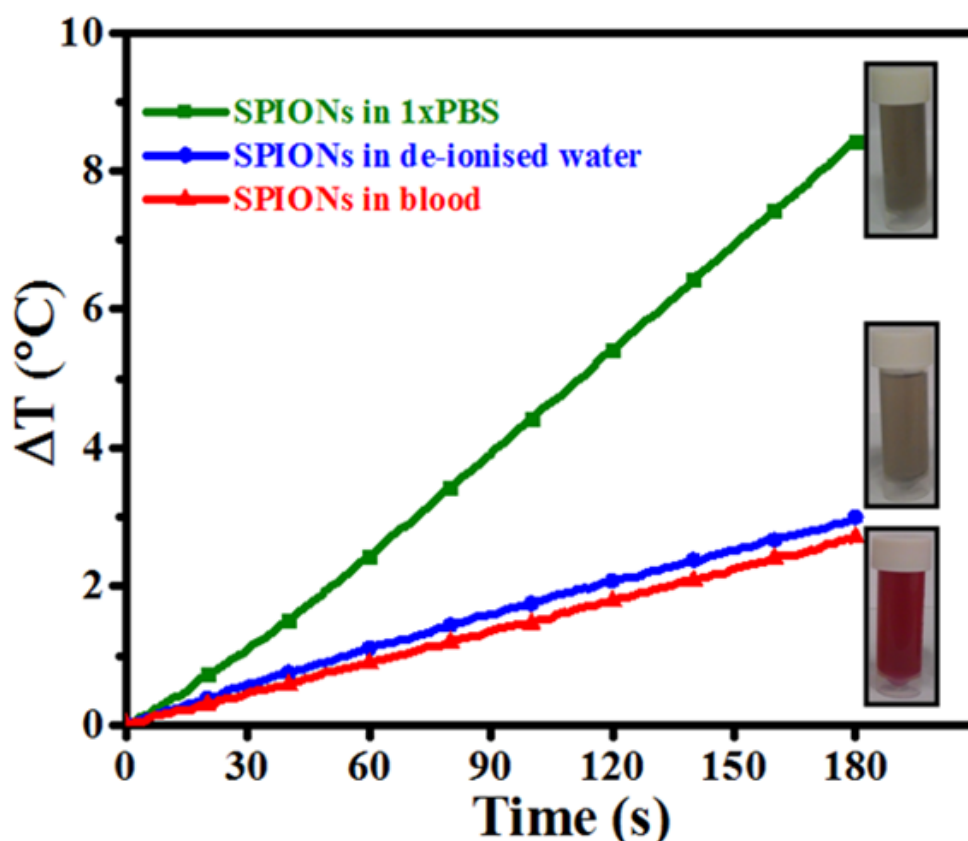


Fig. 4.2: Time dependent temperature raise (ΔT) of 0.1mg/ SPIONs in water, 1xPBS and blood under 600 Oe at 360 kHz. Inset images are representational pictures of the samples.

From Fig. 4.2, we observed that magnetic hyperthermia of SPIONs ticles can be enhanced greatly if the particles were dispersed in 1xPBS. Since our DLS measurements of SPIONs in 1xPBS showed that the particles were stable in

1xPBS with a similar result as Fig. 4.1(e) (SPIONs in de-ionized water), the increase in heating efficiency might be attributed to the presence of ions in the physiological electrolytes (1xPBS). As shown in Fig. 4.2, SPIONs dispersed in blood tend to have comparable magnetic hyperthermia effect to SPIONs in de-ionized water. It seems that the additional hyperthermia efficiency probably caused by the ions present was retarded by other components (such as cells and proteins). Thus, it is important to investigate how magnetic hyperthermia of SPIONs is affected in biological environment. This observation motivated us to further systematically study the contribution of individual physiological components towards hyperthermia under AC magnetic field.

Contribution of physiological components to magnetic hyperthermia

In this work, we have studied the contribution of individual physiological components towards magnetic hyperthermia. All studies were carried out under the standard conditions of 600 Oe and 360 kHz for a period of 3 minutes.

Contribution of physiological ions to temperature raise

Since 1xPBS can enhance magnetic hyperthermia as observed from Fig. 4.2, we carried out a series of experiments to further investigate if 1xPBS has hyperthermia properties. As shown in Fig. 4.3, the hyperthermia effect is

clearly dependent on concentration of ions. The temperature raise (ΔT) decreased with decreasing PBS concentration. With 0.2xPBS, the temperature increase decreases to the level below 1°C which is comparable with the measurement error ($0.5 - 1.0^\circ\text{C}$).

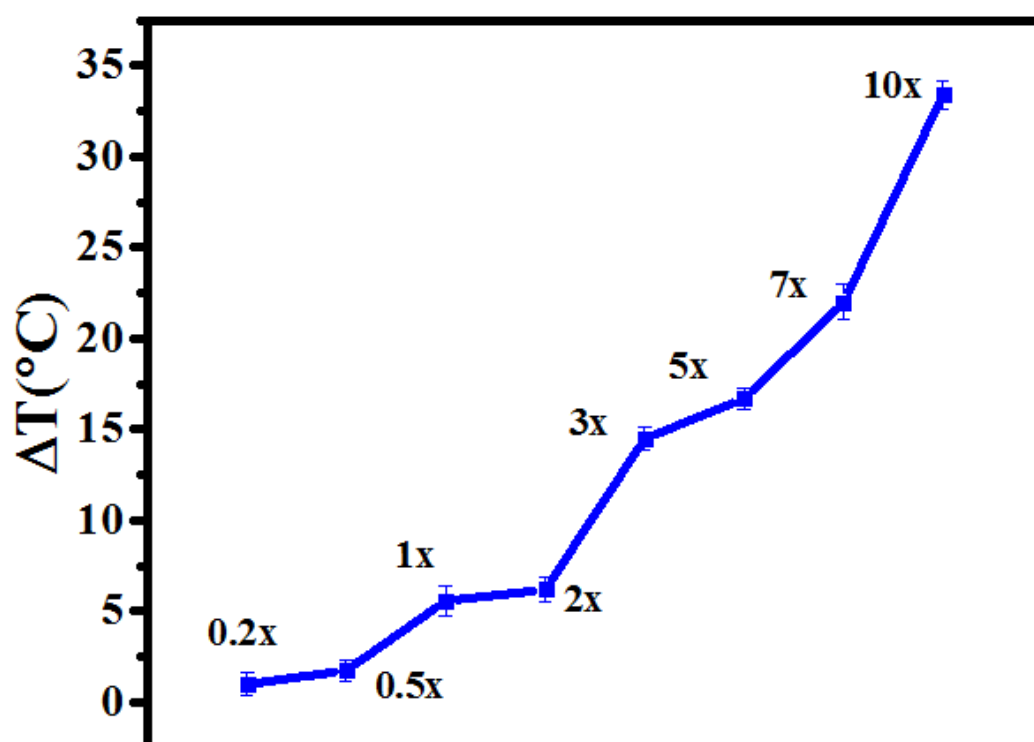


Fig. 4.3: Effect of concentration of PBS on temperature raise (ΔT). As the concentration of 1x PBS increases, ΔT increases, indicating that concentration of ions to ΔT .

In addition, we have studied how AC magnetic field affect the hyperthermia effect of 1xPBS. Magnetic field is found to affect the tissue in the presence of SPIONs. Therefore it is important to study the effect of magnetic field. Contribution of applied magnetic field over a range of 200-600 Oe and frequency at 360 kHz for 3 minutes were tested for 1x PBS without SPIONs.

As shown in Fig. 4.4 as the magnetic field increases, the ΔT increases linearly in a proportionality equivalent to the square of applied field, (Applied field)².

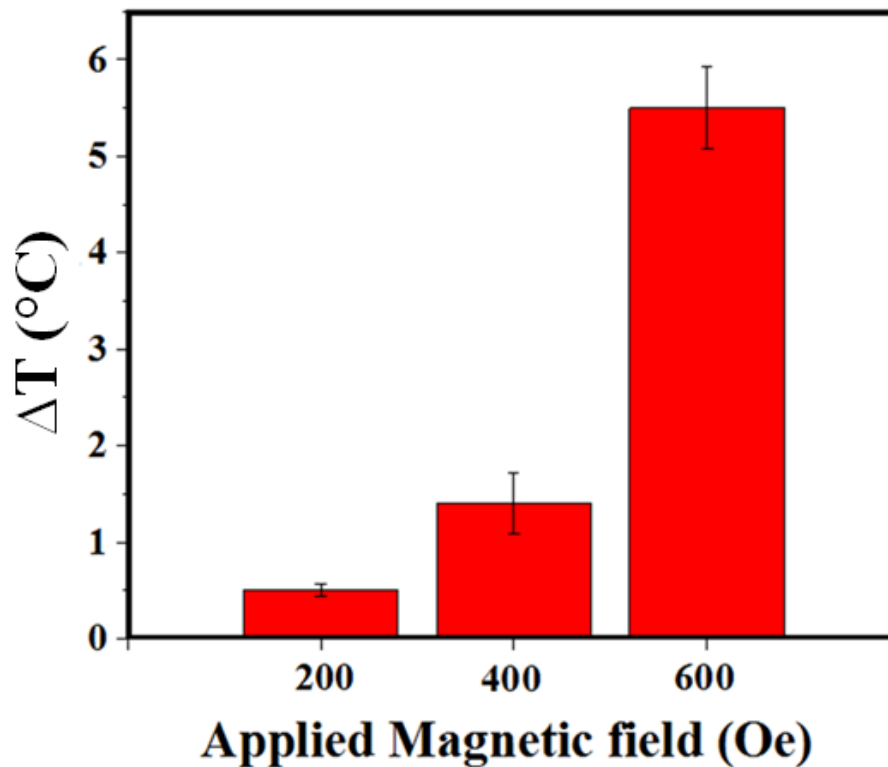


Fig 4.4: Contribution of applied magnetic field towards temperature raise (ΔT) of 1x PBS

The physiological composition of individual salts that constitute 1xPBS is shown in table 4.1. We have studied the hyperthermia effect of the individual constituent salts as shown in Fig. 4.5. It is also interesting to learn from the Fig. 4.5 that certain salts like potassium chloride (KCl) elicit higher temperature raise even at lower concentration of (0.05 M) when compared to a higher concentration of (0.1M) sodium chloride (NaCl). Fig. 4.5 also shows

that the contribution of certain salts like dipotassium phosphate (K_2HPO_4) and disodium phosphate (Na_2HPO_4) is almost negligible after statistical error.

Table 4.1: Physiological concentration of physiological electrolytes as present in 1xPBS

| Salt | Concentration (M) |
|--|------------------------------|
| Sodium Chloride (NaCl) | 0.1 |
| Potassium Chloride (KCl) | 0.05 |
| Disodium hydrogen phosphate (Na_2HPO_4) | 0.005 |
| Dipotassium hydrogen phosphate (K_2HPO_4) | 0.002 |
| Sodium bicarbonate (NaHCO_3) | 0.04 |
| Calcium Chloride (CaCl_2) | 0.02 |
| Magnesium Sulphate (MgSO_4) | 0.005 |
| Sodium Sulphate (Na_2SO_4) | 0.005 |

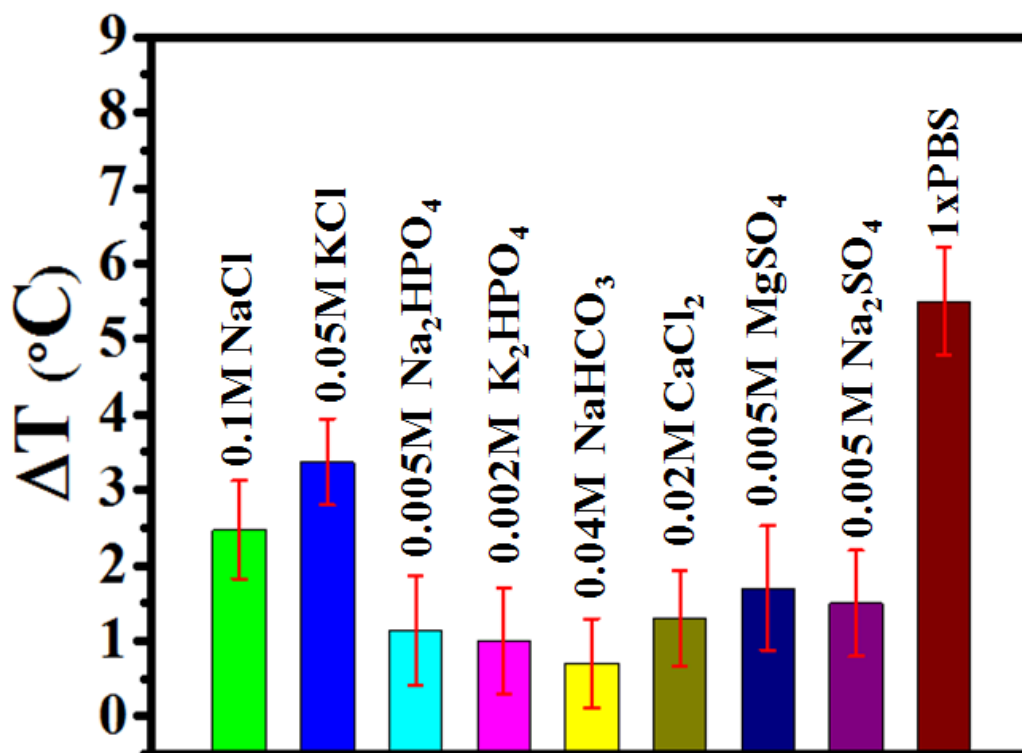


Fig. 4.5: Temperature raise (after 3 minutes under 600 Oe at 360 kHz) of individual salts that constitute 1xPBS.

To further confirm that mobility of ions contribute positively to hyperthermia, we studied the effect of individual ions that make up 1xPBS. We had taken physiological sodium salts (sodium chloride, sodium sulfate, disodium hydrogen phosphate and sodium bicarbonate) of different concentration, viz 0.1M, 0.5M and 1M. It is observed from Fig. 4.6(a) that as the degree of solvation increases, the contribution to temperature raise (ΔT) increases. The trend was maintained throughout increasing concentration of the salts. We also tried to study the contribution of different concentrations of physiological chloride salts (sodium chloride, potassium chloride and calcium chloride) to temperature raise (ΔT).

From Fig. 4.6(b), we understood that as the size and atomic mass of the physiological salt increases, the contribution to temperature raise (ΔT) increases. This might be because of the higher oxidation state and atomic mass of the ions. The heavier ions generate more heat under the applied magnetic field. Also higher the ability to ions' solvate and attract water molecules, higher is the heat generated. Thus ions contribute significantly towards the increase in heating efficiency of a magnetic hyperthermia system.

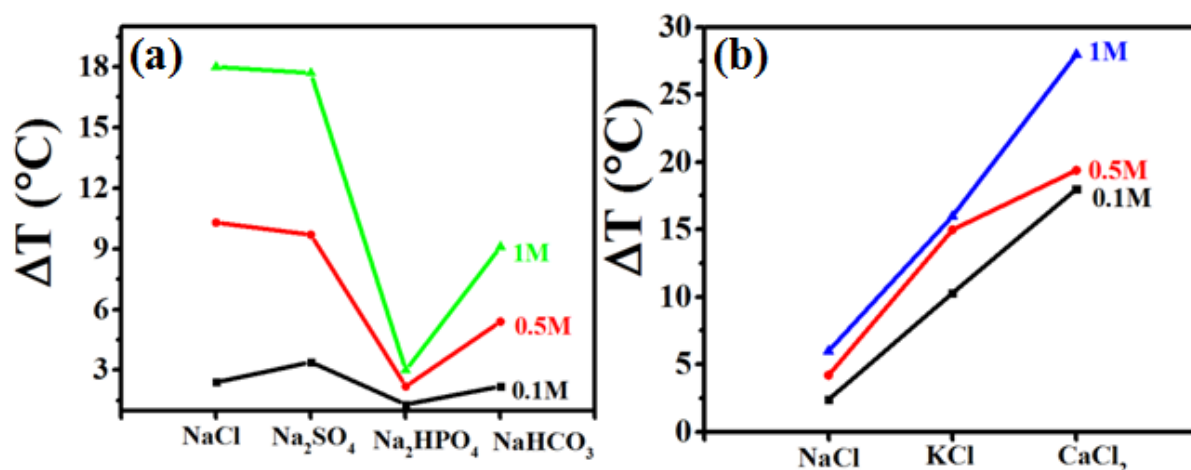


Fig. 4.6: Contribution of individual ions (a) sodium salts (b) chloride salts to temperature raise (ΔT)

Further studies on the effect of physiological acids and ions on temperature raise were carried out. pH plays a pivotal role in cancer biology, both in the intra and extracellular regimes [184, 185]. Physiological acids like lactic acid which are secreted because of anaerobic respiration of cancerous cells sensitize the tumor cells to heat treatment [186, 187]. We wanted to study if acids, in physiologically feasible concentration of around 0.1M and pH value

of 5.4-5.7 can be sole or synergistic heating agents under applied magnetic field for magnetic nanoparticle based hyperthermia. Fig. 4.7 shows that the cellular acids, in near physiological concentrations contribute a little to heating characteristics. Citric acid contributes to ΔT as low as 2.2°C , followed by acetic acid 2.38°C , ascorbic acid 2.5°C and lactic acid 2.7°C . Physiological acids are secreted more by cancerous tissue and have been reported to contribute towards the sensitization of tumor cells.

For comparison studies, we also studied the contribution of 0.1 M strong acids. Hydrochloric acid leads to higher temperature raise (ΔT) of 4.5°C , followed by nitric acid 3.8°C and sulphuric acid 3.2°C . The purpose of this study is to understand that as the dissociation constant (k_a) increases (weak acids to strong acids), the contribution of the acids to the temperature raise (ΔT) increases. The strength of any acid in a solution is quantitatively expressed as dissociation constant (k_a). Weak acids have low dissociation constant as their extent of dissociation into constituent components is low. The logarithmic constant of dissociation constant (k_a) is expressed as $\text{p}k_a$ and is the inverse of k_a . We understand from Fig. 4.7, that as the $\text{p}k_a$ decreases, the ΔT increases as the mobility of ions in the solution increases and causes a temperature raise (ΔT).

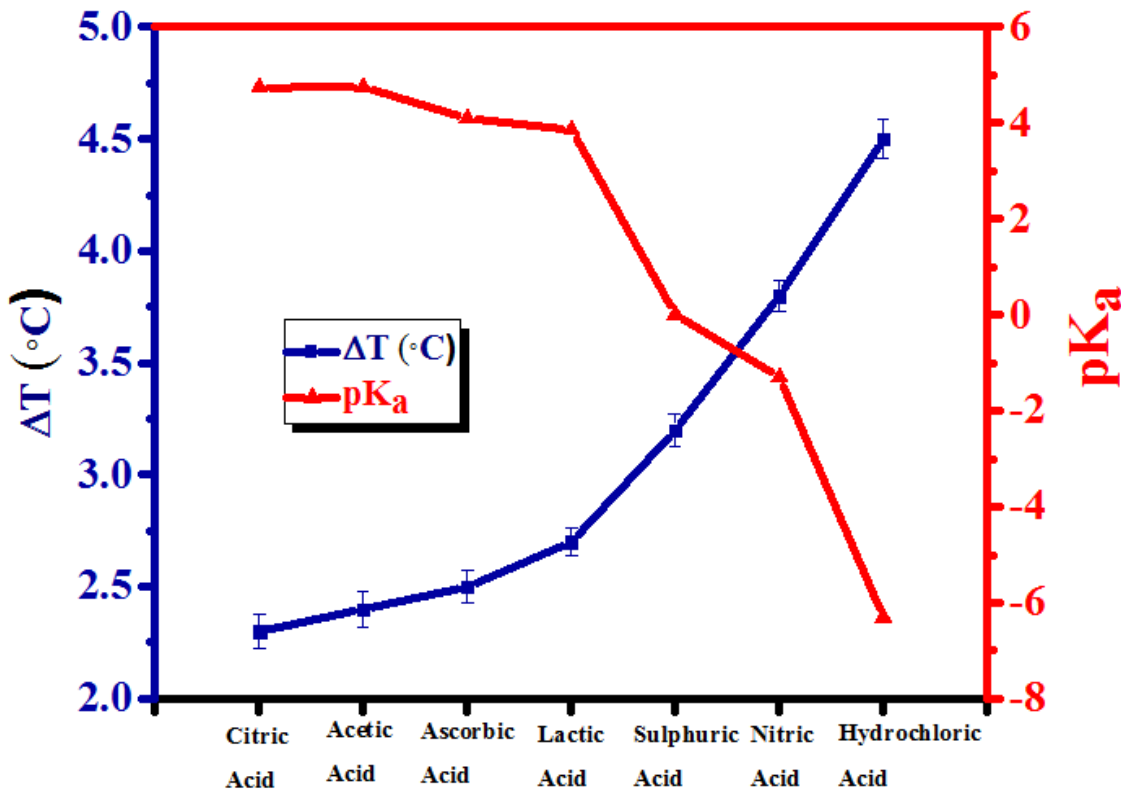


Fig. 4.7: Contribution due to acids to temperature raise (ΔT). The temperature raise (ΔT) is proportional to the dissociation constant (k_a) of the acids.

In this work, we have studied hyperthermia attributed to the presence of ions. Our study has shown that hyperthermia effect (or temperature raise, ΔT) strongly depends on magnetic field and concentration, as well as dissociation (or solvation) and ionic mass.

Contribution of physiological proteins to temperature raise

The above study has shown that the presence of ions can contribute to hyperthermia under AC magnetic field at radio-frequency range. As shown in Fig. 4.2, the contribution of ions to hyperthermia can be greatly reduced in blood. This observation motivated us to investigate the mechanism(s) behind the decreased heating efficiency of SPIONs in blood. We can simplify blood to be an amalgamation of physiological electrolytes, proteins and cells [188, 189]. Therefore along with the study on contribution of ions, a better understanding of the contribution of proteins and cells towards temperature raise (ΔT) is also important. Since in our previous sections we have already reported the heating efficiency of SPIONs in physiological electrolytes and individual contribution of ions, in this section we have attempted to study the heating efficiency of SPIONs in blood and the individual contribution of the blood components towards temperature raise (ΔT) without SPIONs. In addition, blood has higher viscosity compared to 1xPBS and ionized water.

Our first study is to understand if viscosity can affect greatly the hyperthermia effect of ions. In order to understand the contribution of viscosity towards retardation of temperature raise (ΔT), we simulated a viscous environment by the addition of 50mg/mL agarose in 1xPBS. Agarose was chosen for our viscosity studies as it is a neutral polymer and a common gelating agent [190, 191]. As shown in Fig. 4.8, the addition of agarose doesn't change the heating

curve significantly, showing that the hyperthermia effect due to ions is not strongly dependent on viscosity. Our previous results also indicate that SPIONs in agarose gel does not change the temperature raise (ΔT) [192].

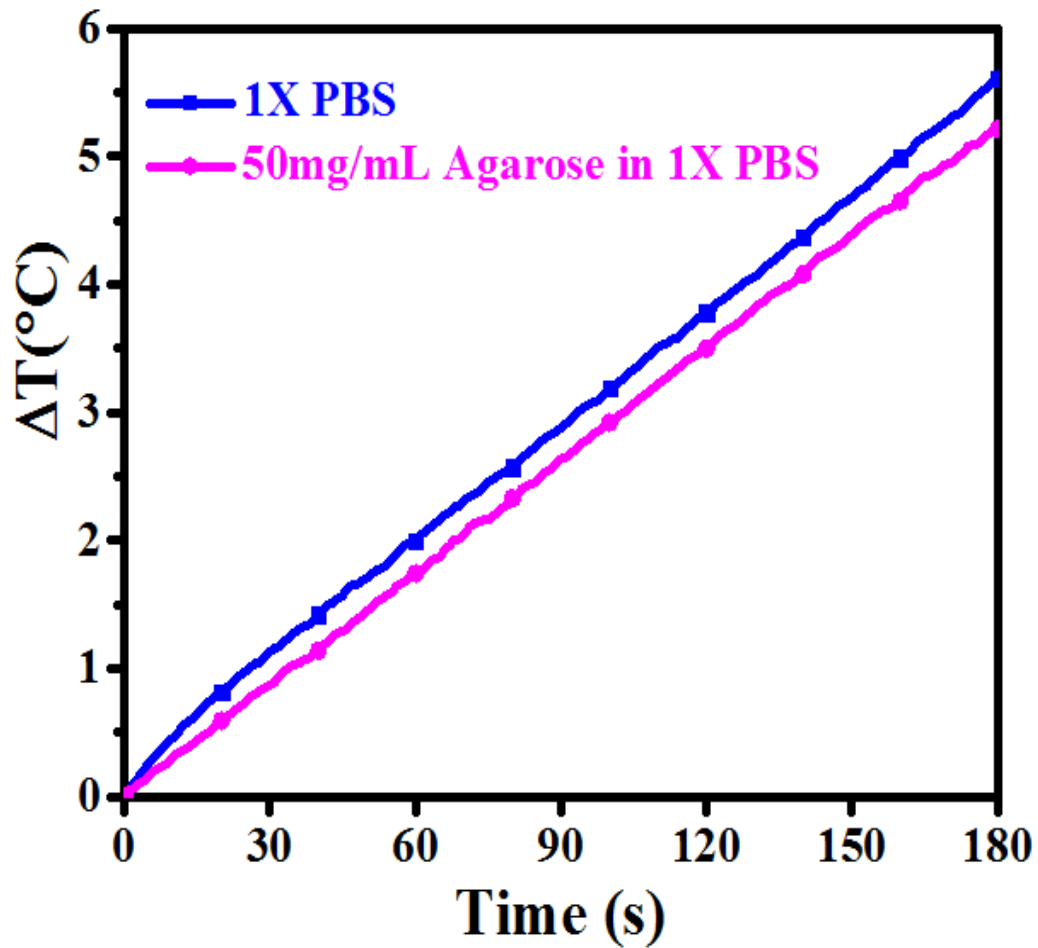


Fig. 4.8: Temperature raise in dependence of time for 1xPBS and 1xPBS with 50 mg/ML agarose under AC magnetic field of 600 Oe at 360 kHz.

Since viscosity doesn't significantly affect the heating characteristics, we then attempted to study the other mechanisms by which the blood components might affect the temperature raise (ΔT). We further studied in the detail the

role of proteins towards retardation of temperature raise (ΔT) since blood is made of physiological electrolytes (of 1xPBS concentration), proteins and cells. Our first study was the hyperthermia effect of plasma (which might be considered as a biofluid with a composition similar to that of protein in 1xPBS). Indeed, the hyperthermia effect has been significantly reduced with or without magnetic nanoparticles compared to its counterpart–1xPBS. Without magnetic nanoparticles, temperature raise (ΔT) was found to be 5.5 °C for 1xPBS under the standard condition (600 Oe at 360 KHz for 3 minutes), while temperature raise (ΔT) was significantly reduced to 2.2 °C for plasma under the same condition.

The further study was hyperthermia effect of 1xPBS with different concentration of protein. We chose the most abundant plasma protein–albumin for our studies. The total albumin concentration in blood plasma is 50mg/mL albumin [193, 194]. The total protein content of plasma is 80mg/mL, including albumin and globulin [195]. From Fig. 4.9(a), it is observed that as the concentration of albumin in 1xPBS increases, the temperature raise (ΔT) decreases. For albumin concentration of 50mg/mL in 1xPBS, temperature raise (ΔT) decreases to 2.4°C. When the concentration increases to 80 mg/mL, temperature raise (ΔT) further retards to 2°C. It should be noted that this value is almost as the same as temperature raise (ΔT) 2.2°C for plasma (which also contents a total protein concentration of 80 mg/mL). The addition of SPIONs in the simulated protein environment (in 1xPBS)

follows the trend. The heating efficiency of SPIONs in 80mg/mL protein environment is 3.4°C, which is comparable to that in plasma (3.2°C). Similarly, SPIONs in 100mg/mL protein environment (in 1xPBS) shows a decreased temperature raise (ΔT) of only 2.8°C, which is the same SPIONs in pure ionized water (2.6°C). As shown in Fig. 4.9(a), even under 100 mg/mL of albumin in 1xPBS, there is still clear temperature of 1.7 °C. But for pure blood, no noticeable temperature raise (ΔT) was measured. The result indicates that cells should have certain reducing effect on hyperthermia. Therefore we studied the contribution of 1xPBS and cells. We used MCF-7 cells for our studies. In our studies, for ease of understanding, we consider cells to be proteins as well, since cells are made of 55% proteins [196]. Fig. 4.9(b) shows that MCF-7 cells suspended in 1xPBS without SPIONs does not cause temperature raise (ΔT) and hence the MCF-7 cells are alive (stained green) under an applied AC magnetic field of 600 Oe and frequency of 360 kHz. But in the presence of 0.1 mg/mL SPIONs, under an applied AC field, the temperature of MCF-7 cells suspended in 1xPBS increases upto a therapeutic window of 45°C and thus causing the death of MCF-7 cells (red nuclei). These studies further confirm that proteins play a role in masking the effect of physiological ions.

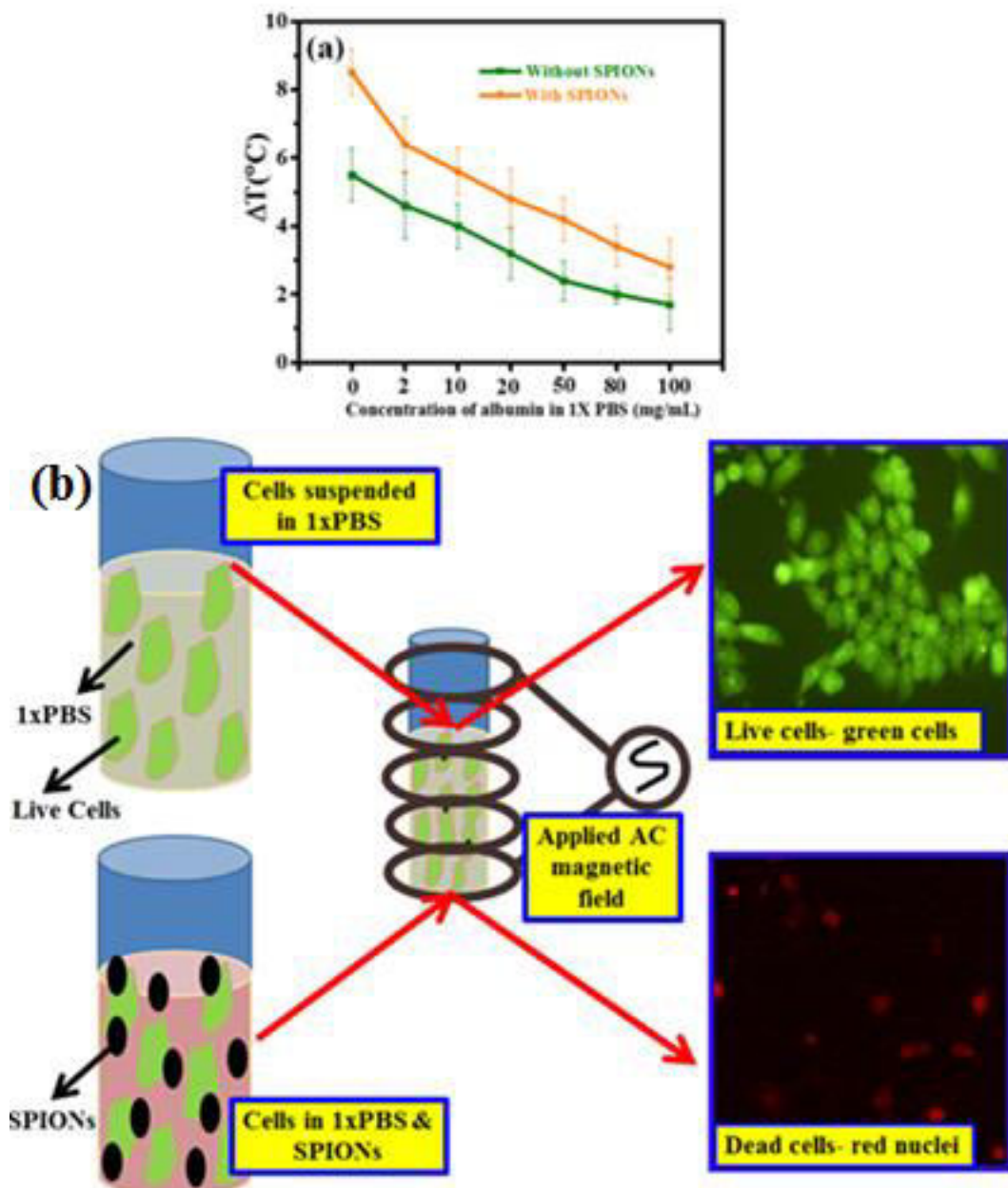


Fig. 4.9: Temperature raise due to physiological protein albumin (a) Temperature raise (ΔT) as a function of albumin concentration in 1xPBS under 600 Oe at 360 kHz for 3 minutes with and without SPIONs (b) Hyperthermia effect on cells suspended in 1xPBS without SPIONs under an applied AC magnetic field–MCF-7 cells are alive as indicated by the green cells in the corresponding confocal image; Hyperthermia effect on cells suspended in 1xPBS with SPION under an applied AC magnetic field- MCF-7 cells are dead as indicated by the red nuclei in the corresponding confocal image.

Mechanism of action of physiological components (ions and proteins) on magnetic hyperthermia

In this work, we have observed that physiological ions can contribute positively to hyperthermia. We have noted that temperature raise (ΔT) depends on several factors, such as concentration, dissociation (or solvation) and atomic mass/size. The results suggest that hyperthermia might be attributed to ionic conduction due to mobility under an applied AC magnetic field. The plausible mechanism by which proteins, especially plasma proteins retard the effect of ions could be by restricting their mobility. The antagonistic behaviour of physiological ions and proteins can be explained through ion mobility and protein surface charge and structure. Ions are trapped in the protein structure and are unavailable to vibrate and generate heat under applied magnetic field. Moreover albumin is a dipolar molecule with excess cations (amino groups) and anions (carboxyl groups) on its surface, which attract the corresponding oppositely charged ions from the physiological electrolytes and further makes them unavailable for heating [197]. This is one reason for decrease in heating efficiency by the plasma proteins. Thus physiological proteins act as biological safety agents that mask the adverse effect of magnetic hyperthermia of SPIONs on the animal/human biosystem. Fig. 4.10 shows the mechanism of ionic mobility in physiological electrolytes and protein environment.

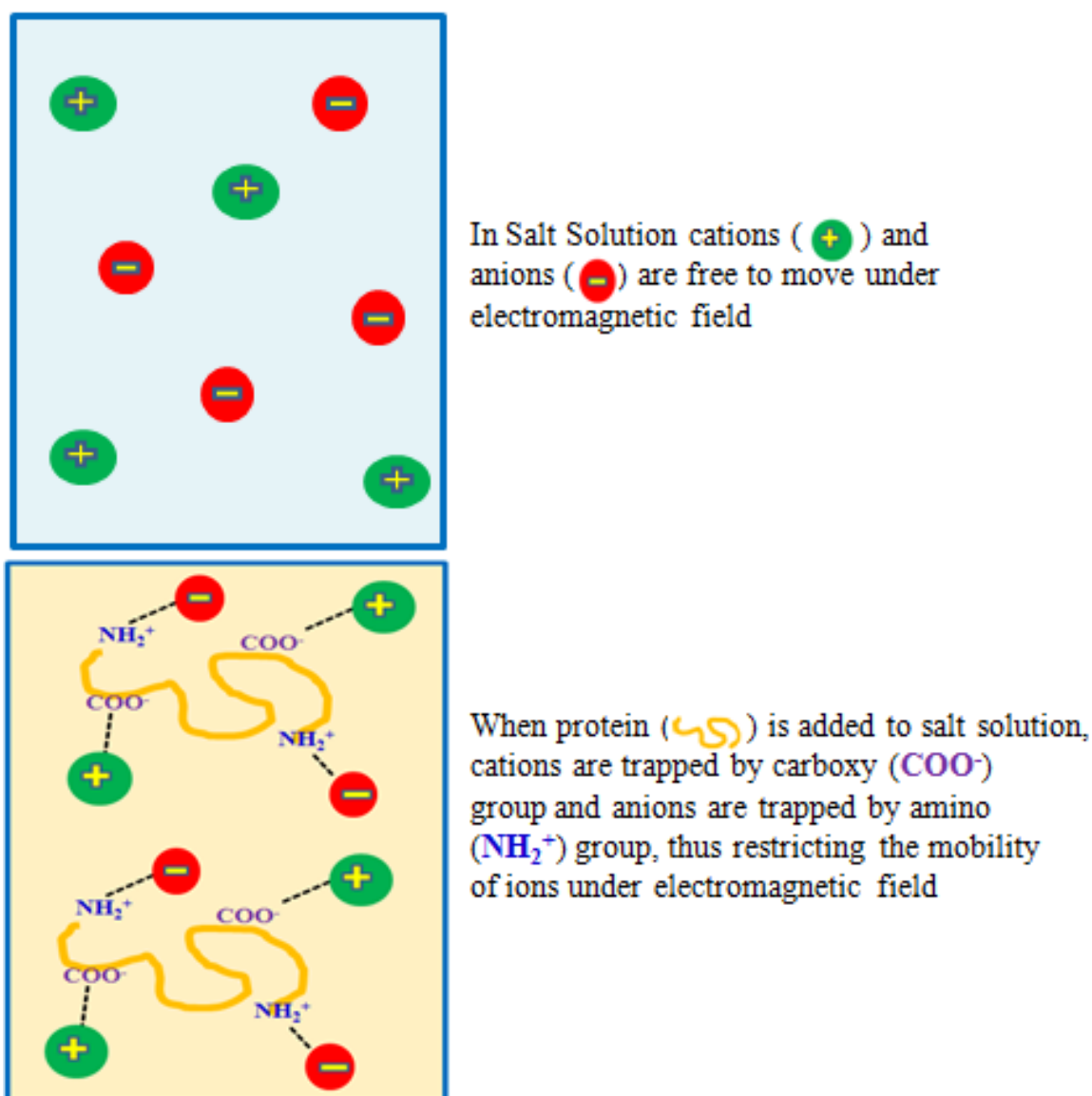


Fig. 4.10: Mechanism of action of physiological components towards magnetic hyperthermia. Salt solution comprising of cations and anions under an applied electric field move towards cathode and anode respectively increasing the temperature raise (ΔT). Whereas the addition of protein with surface charges due to cationic amino (NH_2^+) groups and anionic carboxyl (COO^-) groups trap anions and cations respectively and retard their mobility thus decreasing the temperature raise (ΔT).

Electrochemical studies were conducted to support our proposed mechanism that mobility of ions is a contributing factor for heating efficacy and proteins retard the same. Distilled water, 0.1M sodium chloride solution, 50 mg/mL albumin in distilled water were prepared and impedance was studied over a frequency range of 100 Hz to 1000 kHz. Our experimental frequencies of 150 kHz, 360 kHz and 488 kHz lie within this broad frequency range.

As seen from Fig. 4.11(a) de-ionised water has the highest impedance showing that there is almost no conductance. Fig. 4.11(b), the impedance of 50 mg/mL albumin in distilled water is around 620 Ω in the frequency range used in our magnetic hyperthermia experiments. This shows that proteins are charged biomolecules and hence have reduced impedance. Fig. 4.11(c) shows the comparison between the real parts of impedance of de-ionised water and albumin in water. From Fig. 4.11(d) we observe that 0.1M sodium chloride (NaCl) in de-ionised water has an impedance of only 5 Ω in the frequency range used in our magnetic hyperthermia experiments. Thus substantiating the fact that addition of ions increases the conductivity. From Fig. 4.11(d) we also observe that a solution of 0.1M sodium chloride (NaCl) and 50 mg/mL albumin in de-ionised water has an impedance of only 40 Ω in the frequency range used in our magnetic hyperthermia experiments. While this shows the conductance of ions, it also shows that protein molecules can trap the mobile ions and retard their mobility hindering their contribution towards conductivity. The results of electrochemical studies are in unison with the

magnetic hyperthermia studies. This supports our proposed mechanism of temperature raise (ΔT) contribution of ions and proteins

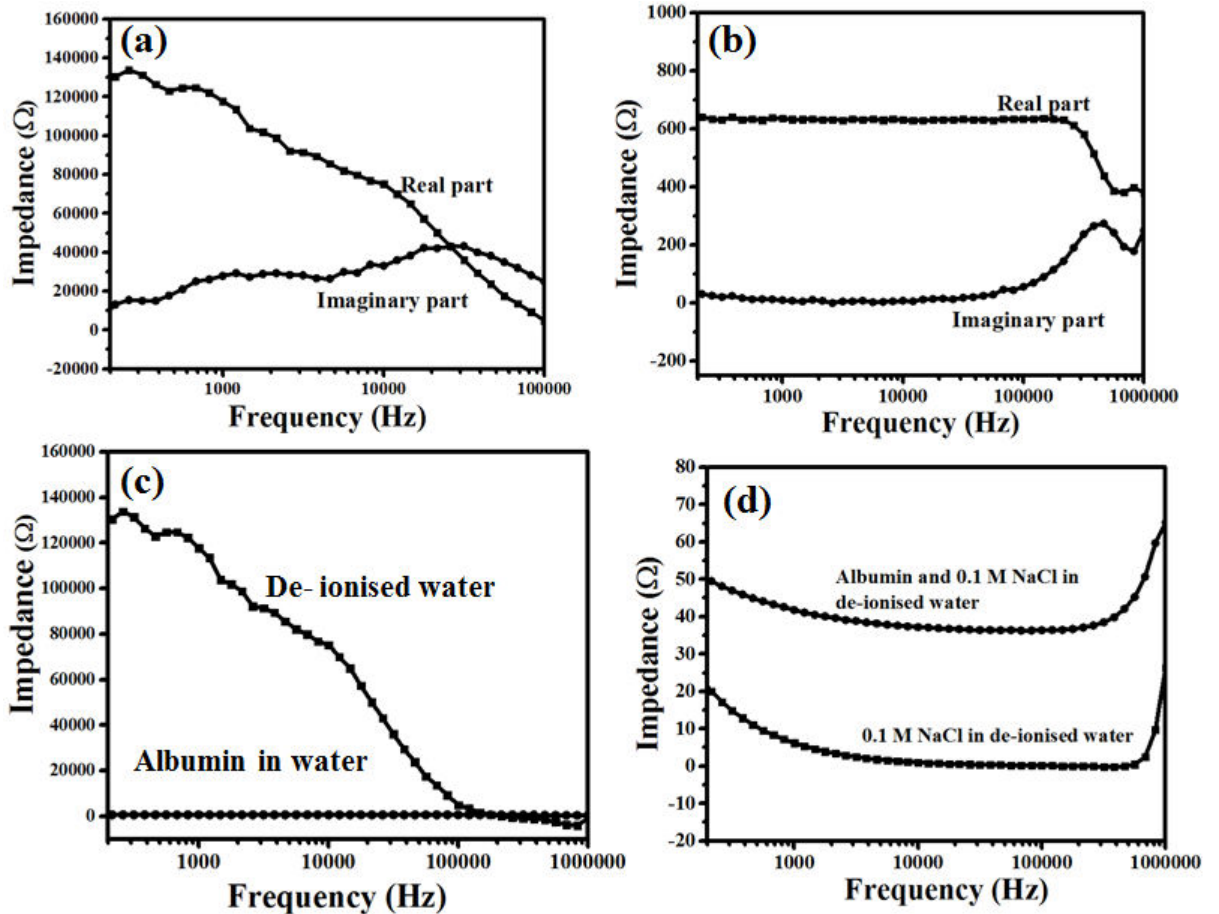


Fig. 4.11: Impedance of (a) de-ionised water (b) 50 mg/mL albumin in de-ionised water (c) comparison between real parts of de-ionised water and 50 mg/mL albumin in de-ionised water (d) comparison between 0.1 M NaCl in de-ionised water and solution of 0.1 M NaCl-50 mg/mL albumin in de-ionised water.

Thus it can be deciphered that proteins and cells are an inherent biological safety mechanism to prevent the adverse effect of heat dissipation under the radiation exposure used for biomedical applications. In order to confirm the same, we studied the effect of applied AC magnetic field on healthy tissue.

Effect of magnetic hyperthermia on healthy tissue

From the above studies, we understand that the use of AC magnetic field is safe for biological system in terms of thermal effect. This is due to the presence of proteins and cells (which are made predominantly of proteins) that can prevent temperature raise (ΔT) caused by physiological ions. The biologically safe standards of maximum field, frequency and/or field frequency have been proposed [198]. In order to verify the biosafety under AC magnetic field, we have studied cells before and after application of AC field in comparison with cell damage after thermal effect. Liver and kidney tissue excised from male Wistar rats were used in this study under the standard condition of 600 Oe and 360 kHz. Magnetic hyperthermia treatment under the combined effect of applied AC magnetic field and 0.1mg/mL SPIONs increases the temperature upto a therapeutic window of 42-45°C leading to severe apoptosis and necrosis, as widely considered. In order to confirm the same, we carried out magnetic hyperthermia experiments on liver and kidney tissue. Fig. 4.12 shows effect of magnetic hyperthermia on healthy liver tissue. Fig. 4.12(a) represents healthy liver tissue as well as tissue after exposure of 600 Oe AC magnetic field for 3 minutes. From the confocal blue nuclei indicating live cells are observed. These qualitative results indicate that AC magnetic field alone without SPIONs does not elicit damage of healthy tissue though physiological ions actually contribute towards heating.

This result supports that cellular proteins act as biosafety agents which prevent damage of healthy tissue. Whereas the combined application of AC magnetic field of 600 Oe and 360 kHz and 0.1 mg/mL SPIONs causes tissue apoptosis (green cells) and necrosis (pink nuclei of dead cells) as seen from Fig. 4.12(b). We repeated the experimental set-up on kidney tissue to further confirm the same. Fig. 4.12(c) represents both the healthy kidney tissue and tissue after application of AC magnetic field of 600 Oe alone for 3 minutes, both which have live cells (blue nuclei). Whereas the addition of 0.1 mg/mL SPIONs under the AC magnetic field raises the temperature upto 42-45°C causing cell necrosis (pink nuclei) as shown in Fig. 4.12(d). This further proves that AC magnetic field alone does not elicit tissue damage and are well within biosafety standards and supports our results with liver tissue. Our results are unison with the widely accepted concept of magnetic hyperthermia, wherein, temperature raise due to magnetic nanoparticles under an applied magnetic field, causes cell necrosis [199].

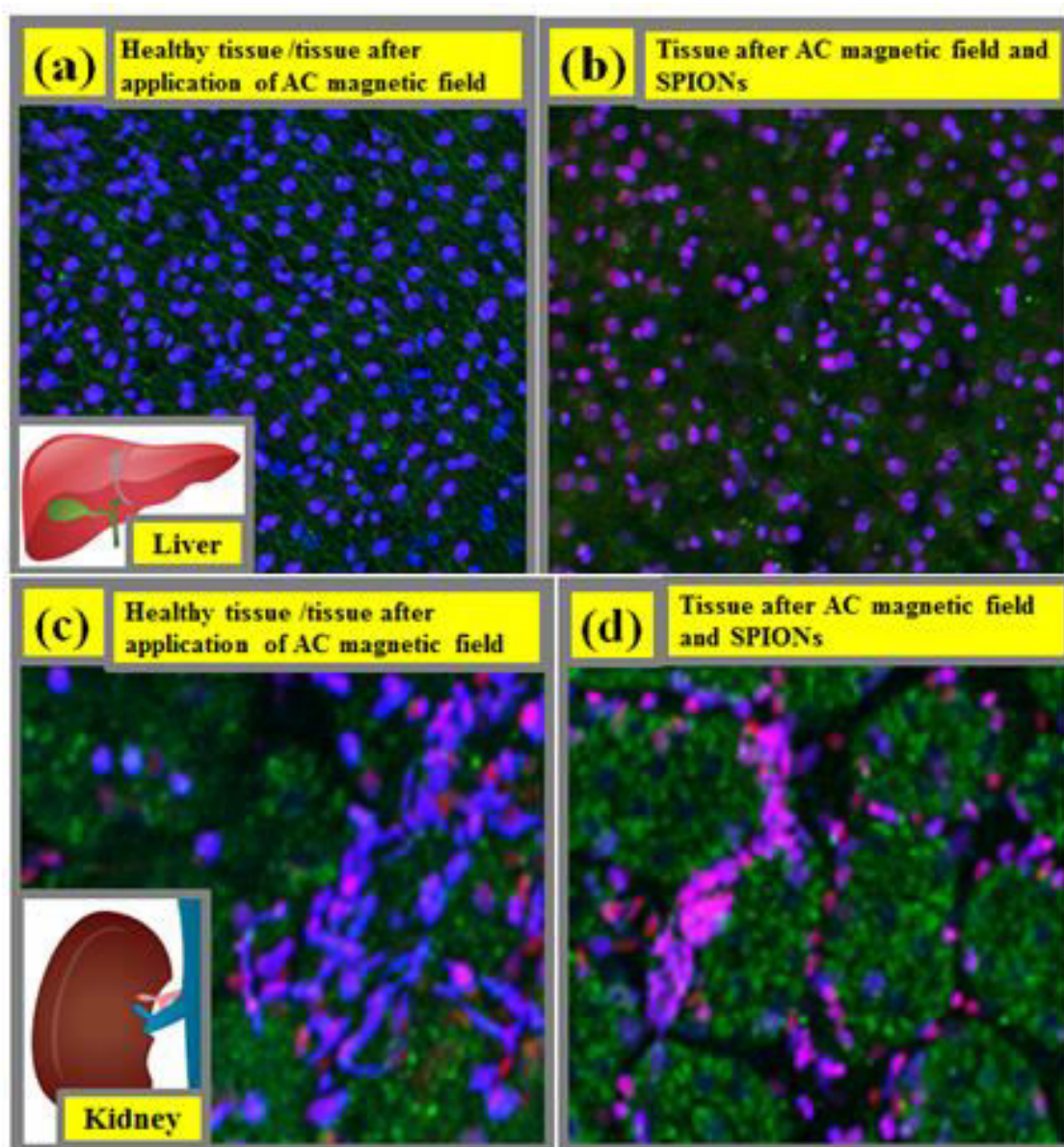


Fig. 4.12: Magnetic hyperthermia effect on liver tissue (a) Healthy liver tissue/tissue after exposure to AC magnetic field of 600 Oe without SPIONs has live cells (b) liver tissue after magnetic hyperthermia treatment under AC magnetic field and 0.1 mg/mL SPIONs causes tissue necrosis and apoptotic cells (c) Healthy kidney tissue/ tissue after application of AC magnetic field alone without SPIONs has live cells (d) liver tissue after magnetic hyperthermia treatment under AC magnetic field and 0.1 mg/mL SPIONs causes tissue necrosis as apoptotic cells.

We further wanted to confirm that the tissue damage was due to hyperthermia induced by SPIONs and not any other physical parameter like applied AC magnetic field. Hence we adjusted the magnetic field and frequency so as to cause a temperature raise (ΔT) of 42°C and 45°C. The results are shown in Fig. 4.13. Fig. 4.13(a) shows healthy liver tissue with live cells (blue nuclei). Fig. 4.13(b) shows that the temperature raise of upto 42°C causes apoptosis (green tissue) and Fig. 4.13(c) shows that 45°C causes complete cell death (pink nuclei).

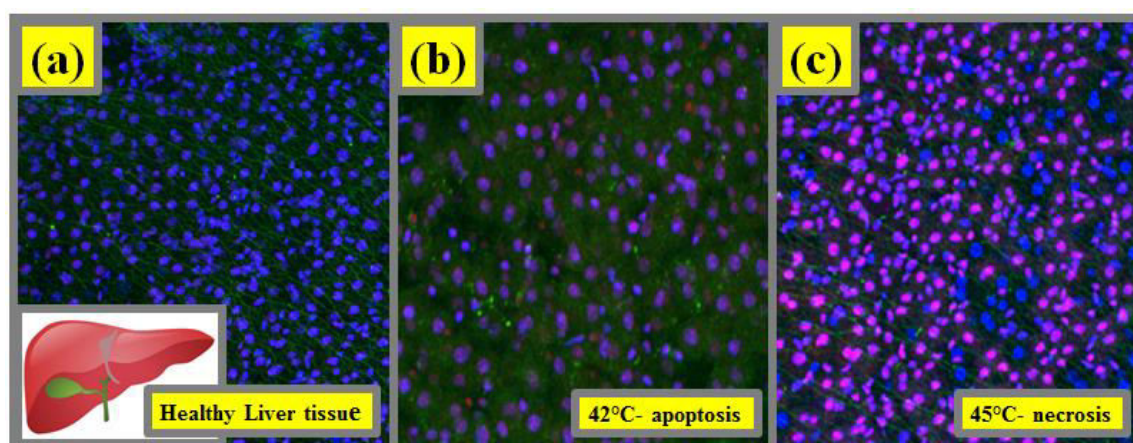


Fig 4.13: Temperature effect on liver tissue (a) healthy liver tissue with live cells (b) temperature raise (ΔT) of upto 42°C causes apoptotic (c) temperature raise (ΔT) of upto 45°C causes complete necrosis

Thus our studies show that AC magnetic field does not render any significant damage to healthy tissue. The biosafety of AC magnetic field is also enhanced by physiological proteins, for reasons discussed in the previous sections.

4.4 Conclusion

We have studied the effect of physiological components (ions and proteins) on the heating efficiency (interms of ΔT and SAR value) of magnetic hyperthermia system. We have systematically studied the individual effect of each component on the heating efficacy of SPIONs under an applied AC magnetic field and also their individual contribution to ΔT . Our results indicate that physiological ions contribute positively towards the heating efficacy of magnetic hyperthermia system due the mobility and diffusivity of the ions. Whereas physiological proteins significantly retard the temperature raise of the SPIONs under an applied AC magnetic field. Therefore the overall contribution heating efficiency is decreased. Thus physiological proteins and cells provide intrinsic biosafety to the biosystem from adverse temperature raise due to exposure to applied AC magnetic field in magnetic hyperthermia. Our studies further confirm that applied AC magnetic field alone does not damage the healthy tissue since physiological proteins and contribute towards biological safety. While extensive research is going on to improve the biocompatibility and heating efficiency of the magnetic nanoparticles, a better understanding of contribution of physiology components towards heating efficacy and biosafety is very important. Our study intends to provide a simple reference to the effect of physiological components on magnetic nanoparticles under an applied AC magnetic field.

Chapter 5: Gd₂O₃ Nanoparticles as MRI contrast agents

5.1 Introduction

This thesis focuses on the synthesis and biomedical application of magnetic metal oxide (Fe₃O₄, Gd₂O₃) nanoparticles. Since our previous chapters have extensively discussed the fabrication and magnetic hyperthermia application of Fe₃O₄ nanoparticles. This chapter focuses on the fabrication and application of Gd₂O₃ nanoparticles in MRI. As discussed earlier, magnetic resonance imaging (MRI) is a promising imaging technique for disease diagnosis at an early stage. It provides high spatial resolution and fine anatomical detailing without exposure to radioisotopes and hence is a complementary modality for molecular imaging [200, 201]. Contrast agents are injected to distinguish the hydrogen nuclei situated at varied environment and highlight the site of interest due to contrast difference resulting from the alternation of the signal intensity [202, 203]. Gadolinium possesses seven unpaired electrons with a spin that perturbs the proton relaxation in water, resulting in an efficient shortening of longitudinal relaxation time (T₁) and increase in the magnetic resonance signal intensity. Hence, gadolinium based image contrast agents provide positive signals, attracting wide research interest [204, 205]. Gadolinium based image contrast agents are the widely used contrast agents in MRI [206]. The unbound gadolinium ions are known to inhibit the calcium channels leading to considerable cardiovascular and neurologic toxicity [207, 208]. The toxicity can be significantly reduced when the gadolinium ions are chelated [209]. However, the concern of the toxicity of gadolinium chelates persists as they release small amount of free gadolinium ions. Inorganic crystalline gadolinium based compound nanoparticles provide a fixed crystal environment effectively

prevents nanoparticles from leaking free gadolinium ions and hence are considered to be new generation of T1 contrast agents [210, 211]. It is a well accepted fact that only surface gadolinium close to the surface contributes to the contrast effect. Therefore, the uniform size and large surface area is very important. Thermal decomposition method gives hydrophobic oleic acid capped Gd₂O₃ nanoparticles. The influence of different surface modifying agents on Gd₂O₃ nanoparticles is investigated in this chapter, based on their T1 relaxation time.

Our previous attempts to find a good biocompatible surface modifying agent shows that albumin conjugation improves the biocompatibility significantly. We expect Gd₂O₃ nanoparticles conjugated with albumin to have better blood circulation time, without compromising on the biosafety. This is an important factor to be considered for clinical MRI imaging. At the same time, since we are aware of the long folded chain structure of Bovine Serum Albumin (BSA), which might make it difficult for the availability of surface gadolinium, we also tried to cap the Gd₂O₃ nanoparticles thioglycolic acid. Since thioglycolic acid (TA) is a very small molecule available to be readily exchanged with oleic acid, it renders hydrophilicity to the Gd₂O₃ nanoparticles, without compromising on the availability of surface gadolinium. This section explores the comparison between BSA conjugated and TA capped Gd₂O₃ nanoparticles.

Later we also tried coating the as-synthesized Gd₂O₃ nanoparticles with a neutral polymer polyvinyl pyrrolidone(PVP) using a ligand exchange strategy. Since PVP offers a neutral surface and inorganic surface, it does not elicit the attraction of unwanted charged molecules. Therefore in this section we tried to cap the Gd₂O₃ nanoparticles with long chain PVP of 40, 000molecular weight. Later we photodegraded the PVP chains *in-situ*. We expected to achieve better relaxivity of short chain PVP chains, due to easy accessibility to water. Due to the high surface energy of the ultra-small Gd₂O₃ nanoparticles, aggregation or dissociation always occurred during the ligand exchange process in harsh chemical synthesis environment [212]. However, the ligand exchange with PVP was very successful in our situation. Excessive PVP was used in the reaction as a driving force for ligand exchange. Dichloromethane assisted the precipitation of PVP coated Gd₂O₃ nanoparticles in ethyl ether while the oleates remained in the supernatant [213].

5.2 Methods

Haemolytic studies

Erythrocytes were collected by centrifuging the blood of 5 weeks old SCID mice at 700 rpm. The pellet was re-suspended in saline at a ratio of 1:4. The test samples- as-synthesized Gd₂O₃ nanoparticles, TA/PVP capped Gd₂O₃ nanoparticles and BSA conjugated Gd₂O₃ nanoparticles, each of Gd³⁺ ion concentration 0.5 mg/mL were added to the erythrocytes and the samples were

incubated at 37°C for 2 hours. Distilled water, which leads to 100% lysis was used as the positive control as it causes complete haemolysis due to osmosis. 0.1M NaCl was used as negative control, as it is isotonic with the intracellular solute concentration. Haemolysis of erythrocytes is due to the oxidative stress caused by the test samples on the erythrocytes. The stress ruptures the cell membrane of the erythrocytes and hence the haemoglobin (Hb) leaks out into the solution. The absorbance of the leaked haemoglobin was measured at 540 nm by UV-Vis spectrophotometer (UV-Vis, ShimadzuUV-1601). % Haemolysis can be calculated using the formula,

$$\%Haemolysis = [A_t - A_n / A_c - A_n] \times 100$$

Where, A_t - absorbance of the test sample at 540 nm; A_n - absorbance of the negative control (0.1M NaCl) at 540 nm; A_c -absorbance of the positive control (distilled water) at 540 nm. The haemolytic index was also calculated according to ASTM F756-00 standards, according to which, 0-2 % is non-haemolytic; 2-5% is mildly haemolytic and >5% is haemolytic.

Cell viability studies

The BHK cells suspended in 1xPBS were co-incubated with 100 µg/mL of TA/PVP capped and BSA conjugated Gd₂O₃ nanoparticles for 24 hours at 37°C. The BHK cells after incubation were run under flow cytometry. Dyes NucBlue (ThermoFischer Scientific) to stain the total nuclei of cells, AlexaFluor (Invitrogen) to stain the apoptotic cells green and Propidium

Iodide (PI-ThermoFischer Scientific) to stain the nucleus of dead cells red were used to qualitatively visualize the cells. Briefly, to 1 mm² of the BHK cells, 2 drops of NucBlue, 2.5 µL of AlexaFluor and 0.5 µL of PI were added along with 100 µL binding buffer and were incubated at room temperature for 15 minutes. The reaction was stopped by adding excess binding buffer and the samples were run in flow cytometry. In the histogram comprises of 4 quadrants. Quadrant 1 (Q1) represents cells that have under gone complete necrosis; Quadrant 2 (Q2) represents cells at late stage apoptosis, wherein the cell membrane has ruptured; Quadrant 3 (Q3) represents cells at early stage apoptosis; Quadrant 4 (Q4) represents live cells.

Relaxivity measurements

Gd₂O₃ nanoparticles were fabricated and made hydrophilic by TA/PVP capping and biocompatible by conjugating with BSA. The samples were well dispersed and stable in water. The highest concentration of Gd³⁺ ions in the samples were 0.3mM each. The samples were diluted to 6 different concentrations (0.3mM, 0.15 mM, 0.075 mM, 0.037 mM 0.018 mM and 0 mM). The longitudinal (r1) and transverse (r2) relaxivities were measured using a 7T Bruker ClinScan with a Siemens interface and 72mm volume coil. T1 measurement was done using an inversion-recovery sequence; TR/TE = 5000/7; Average=3; flipangle = 90° and inversion-times (TIs) =31, 150, 300, 700, 1200, 1800, 2400, 3000, 3600, 4000, 4500 and 4900 ms. T1 was calculated from the inversion-recovery images, by fitting for the decay curve.

T2 measurement was performed using a multiple spin echo sequence TR = 5000 ms; TE = 12.9; NE = 14. The sample was maintained at 36°C using a water bath. T2 maps were obtained along with the inline acquisition sequence program. The r1 and r2 values were obtained from slope of the linear fit between 1/T1 or 1/T2 vs concentration of contrast agent in mM. The relaxivity is represented as mM⁻¹s⁻¹ ± SD (n = 3).

5.3 Results and Discussion

As-synthesized Gd₂O₃ nanoparticles

Ultra-small Gd₂O₃ nanoparticles of size 3 ± 1 nm were synthesized by thermal decomposition method. Fig 5.1(a) shows the TEM image of the as-synthesized oleic acid capped Gd₂O₃ nanoparticles. The particles seem to be aligned in chains. This might be due to the high surface energy of the ultra small Gd₂O₃ nanoparticles. The SAED pattern corresponding to (222), (440) and (664) in Fig. 5.3.1(b) reveals the crystal structure of the Gd₂O₃ nanoparticles.

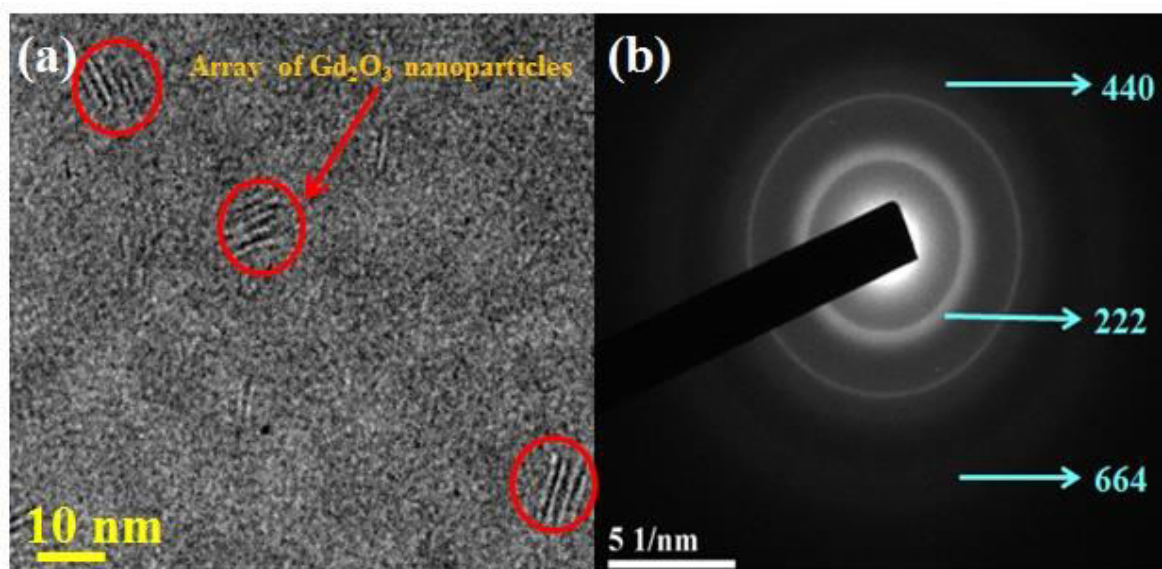


Fig. 5.1: As-synthesized hydrophobic, oleic acid capped Gd_2O_3 nanoparticles
 a) TEM image of Gd_2O_3 nanoparticles b) SAED pattern of Gd_2O_3 nanoparticles.

5.3.1 Comparison between thioglycolic acid and BSA conjugated Gd_2O_3 Nanoparticles

Hydrophilic phase transfer of Gd_2O_3 nanoparticles using TA and BSA

Since the as-synthesized Gd_2O_3 nanoparticles were hydrophobic in nature due to oleic acid coating, they were converted to water phase by ligand exchange with TA. Later the TA capped Gd_2O_3 nanoparticles were converted to biocompatible phase by conjugating with BSA. Fig. 5.2 shows the hydrodynamic radius comparison between TA capped Gd_2O_3 nanoparticles and BSA conjugated Gd_2O_3 nanoparticles. As expected, BSA conjugated Gd_2O_3

nanoparticles have much higher average hydrodynamic radius of 16 ± 2 nm than 7 ± 2 nm of their TA counter part. The inset figure shows the TEM image of BSA conjugated Gd_2O_3 nanoparticles.

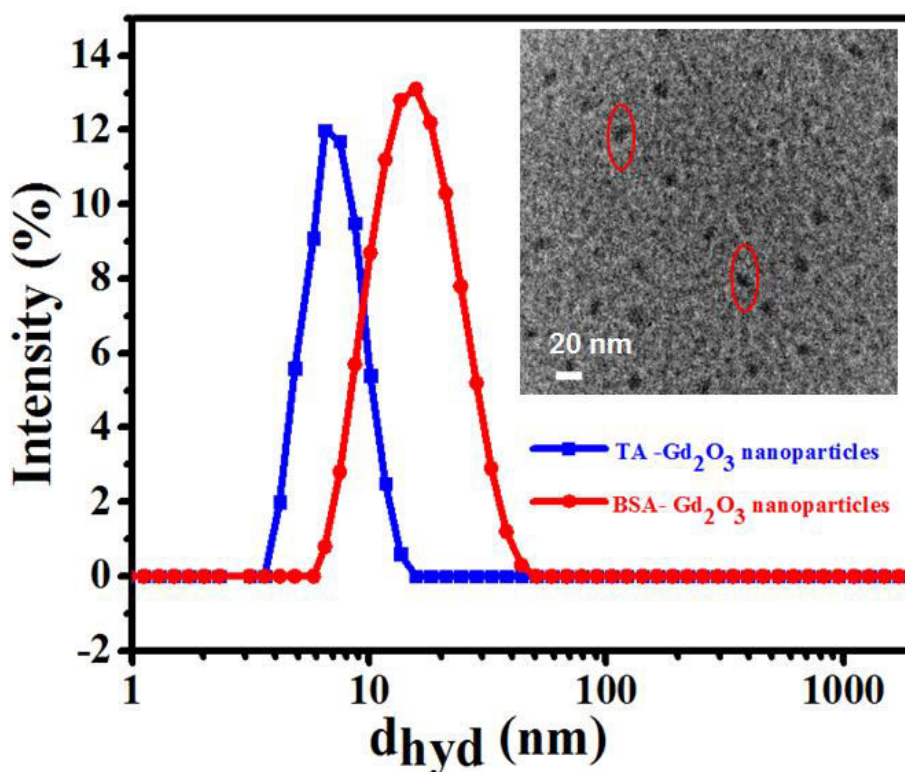


Fig. 5.2: Average hydrodynamic radius of BSA conjugated Gd_2O_3 nanoparticles. Inset image shows the TEM image of BSA conjugated Gd_2O_3 nanoparticles.

Biocompatibility of TA capped and BSA conjugated Gd_2O_3 nanoparticles

The haemolysis studies confirm that blood compatibility of BSA conjugated Gd_2O_3 nanoparticles. Fig. 5.3(a) shows that BSA conjugated Gd_2O_3 nanoparticles have a very low haemolysis of 1.2 % (non-haemolytic) when

compared to 4.8 % of TA capped Gd₂O₃ nanoparticles (mildly haemolytic) and 52.3 % of oleic acid capped Gd₂O₃ nanoparticles (haemolytic). The inset photos show the Oleic acid (OA) capped, Thioglycolic acid (TA) capped and BSA conjugated Gd₂O₃ nanoparticles. We hence performed the cell viability studies on healthy BHK cells. The histogram in Fig. 5.3(b) and Fig. 5.3(c) shows that TA capped Gd₂O₃ nanoparticles (98.4%) are less viable than BSA conjugated Gd₂O₃ nanoparticles (99.6%), as BSA is a better biocompatible agent. It should be noted that there are almost no cells in Q1 and Q2, indicating that there no healthy BHK cells entering necrosis or even late stage apoptosis respectively. TA capping does not completely render biosafety, owing to their small size, exposing the gadolinium to the biosystem. Quadrant Q1 of Fig. 5.3(b) shows cells indicating that some cells have entered into necrosis, while Q2 shows that there are a few cells in late apoptotic stage.

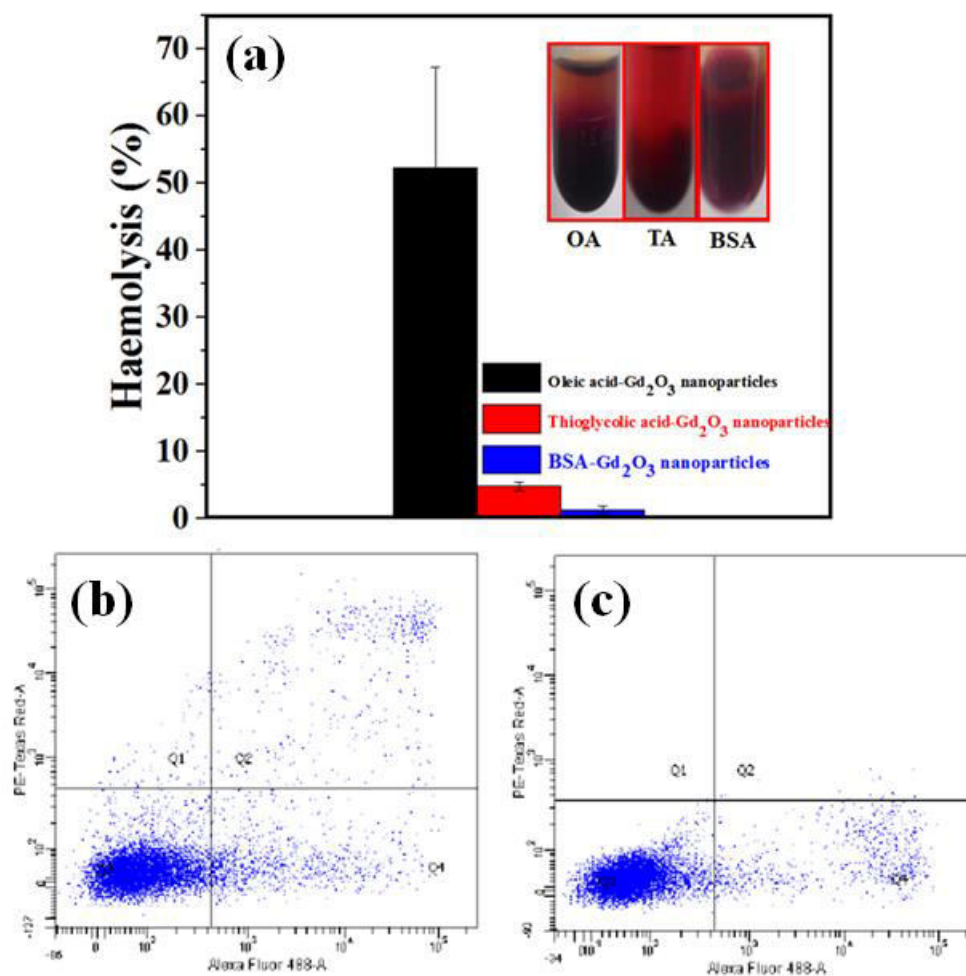


Fig. 5.3: Biocompatibility of BSA conjugated Gd_2O_3 nanoparticles a) Haemolytic study comparison between oleic acid (OA) capped, thioglycolic acid (TA) capped and BSA conjugated Gd_2O_3 nanoparticles. Inset image shows the haemolysed blood sample b) Cell viability of TA capped Gd_2O_3 nanoparticles- 98.4% c) Cell viability of BSA conjugated Gd_2O_3 nanoparticles- 99.6%

Relaxivity measurements of TA capped and BSA conjugated Gd_2O_3 nanoparticles

As shown in Fig. 5. 4(a) TA capped Gd_2O_3 nanoparticles show a high r_1 value of $3.3 \text{ mM}^{-1}\text{s}^{-1}$ when compared to the r_1 value of $2.8 \text{ mM}^{-1}\text{s}^{-1}$ of BSA conjugated Gd_2O_3 nanoparticles as shown in Fig. 5.4(b). It is to be noted that

for a concentration of Gd³⁺ as low as 0.3 mM, a very good relaxivity is achieved. This is due to the easy access of surface gadolinium to water molecules. The inset T1 phantom images of TA capped Gd₂O₃ nanoparticles and BSA conjugated Gd₂O₃ nanoparticles at different concentrations clearly demonstrated their contrast difference as T1 contrastagents.

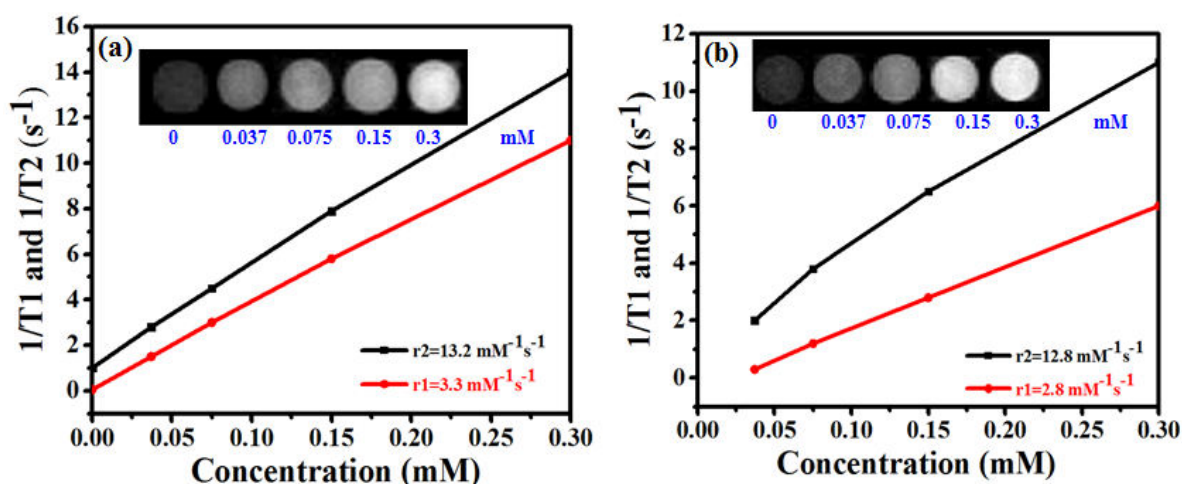


Fig. 5.4: Relaxivity measurements a) TA capped Gd₂O₃ nanoparticles b) BSA conjugated Gd₂O₃ nanoparticles.

5.3.2 *In-situ* Photodegraded Poly Vinyl Pyrrolidone coated Gd₂O₃ nanoparticles

Hydrophilic phase transfer of Gd₂O₃ nanoparticles by *in-situ* photodegraded PVP coating

Ultra-small Gd₂O₃ nanoparticles of size 3 ± 1 nm as discussed in the previous section was used for *in-situ* photodegradation of PVP coated Gd₂O₃

nanoparticles. The as-synthesized particles were hydrophobic in nature, and were converted to water phase by ligand exchange of oleic acid moiety with 40,000 MW PVP. Fig. 5.5(a) shows the FTIR plot for PVP capped Gd₂O₃ nanoparticles. The resonance peaks in the plot at 1643 1/cm corresponding to C=O and 1415 1/cm corresponding to C-N indicate the presence of PVP and the disappear of two characteristic bands at 1557 and 1443 1/cm corresponding to the antisymmetric (COO⁻), and the symmetric, (COO⁻), stretches confirms the complete removal of oleic acid. The samples were then photodegraded using UV lamp of 300 Watt. Fig. 5.5(b) shows the average hydrodynamic radius PVP capped of Gd₂O₃ nanoparticles, at 0th hour, 1 hour, 2 hours, 3 hours and 4 hours. There is a clear decrease in the average hydrodynamic radius, thus confirming that photodegradation has happened.

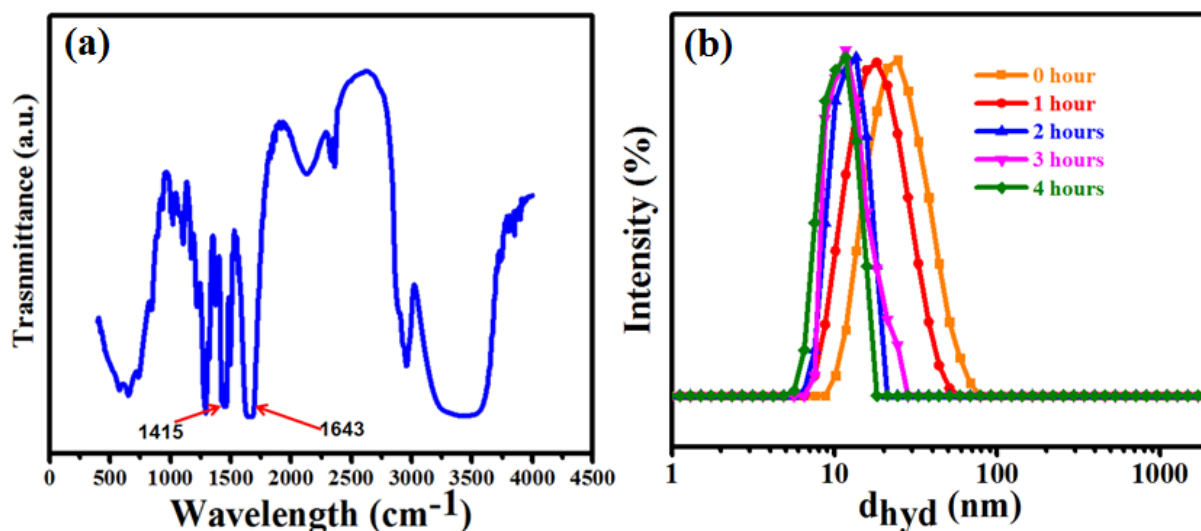


Fig. 5.5: Hydrophilic phase transfer of photodegraded PVP coated Gd₂O₃ nanoparticles a) FTIR plot of photodegraded PVP coated Gd₂O₃ nanoparticles b) average hydrodynamic radius of photodegraded PVP coated Gd₂O₃ nanoparticles.

Biocompatibility studies of photodegraded PVP coated Gd_2O_3 nanoparticles

Fig. 5.6 shows the cell viability histogram of photodegraded PVP coated Gd_2O_3 nanoparticles on healthy BHK cells. The cell viability is upto 99%, without much cells in quadrants Q1. This indicates that the cells did not enter into necrosis stage, even after incubation for 24 hours. This shows that the photodegraded PVP coated Gd_2O_3 nanoparticles show better biocompatibility and are as good as organic, BSA conjugated Gd_2O_3 nanoparticles. The inset image shows that there is the sample non-haemolytic, upto 1.2 %.

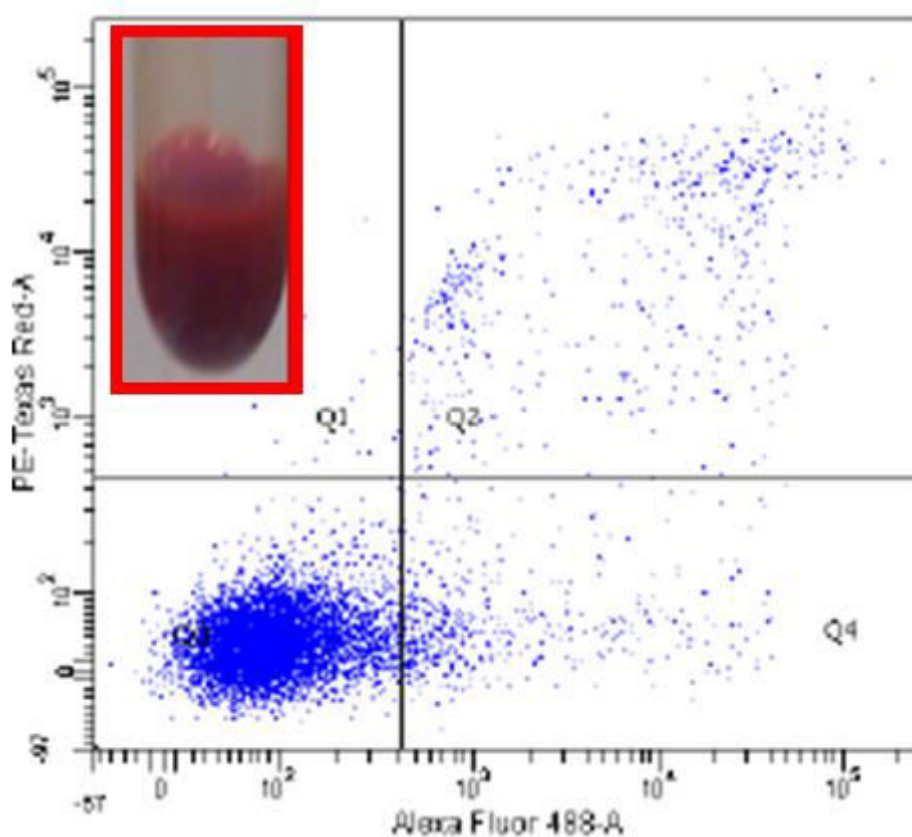


Fig. 5.6: Biocompatibility of photodegraded PVP coated Gd_2O_3 nanoparticles, showing cell viability of 99% and haemolysis of 1.2%.

Relaxivity measurements photodegraded PVP coated Gd₂O₃ nanoparticles

Fig. 5.7 shows that the r_1 (12.3 mM⁻¹s⁻¹) and r_2 (17.6 mM⁻¹s⁻¹) values for photodegraded PVP capped Gd₂O₃ nanoparticles were much higher than that discussed in our previous section. The inset image gives the T1 phantom images corresponding to various concentrations. The polar C=O group in each monomer of PVP also allows the water molecules to pass through the coating layer and hence facilitates the interaction with Gd₂O₃ nanoparticles which further reduces the T1 relaxation time. *In-situ* photodegradation is better than using short chain PVP of 5000 MW. This is because, *in-situ* photodegradation gives the convenience of manipulating the length of the PVP chain, as per our requirements. Chain lengths as low as 3 nm capping the gadolinium nanoparticles individually, without compromising on the biocompatibility can be achieved. This is not possible with commercially available long chain PVP. *In-situ* photodegradation is better than pre-photodegradation before capping, because, it makes use of the strong ligand exchange capabilities of long chain PVP. Thus ensuring better surface modification. The excess oleates and broken chains were thoroughly washed by microfiltration and dialysis.

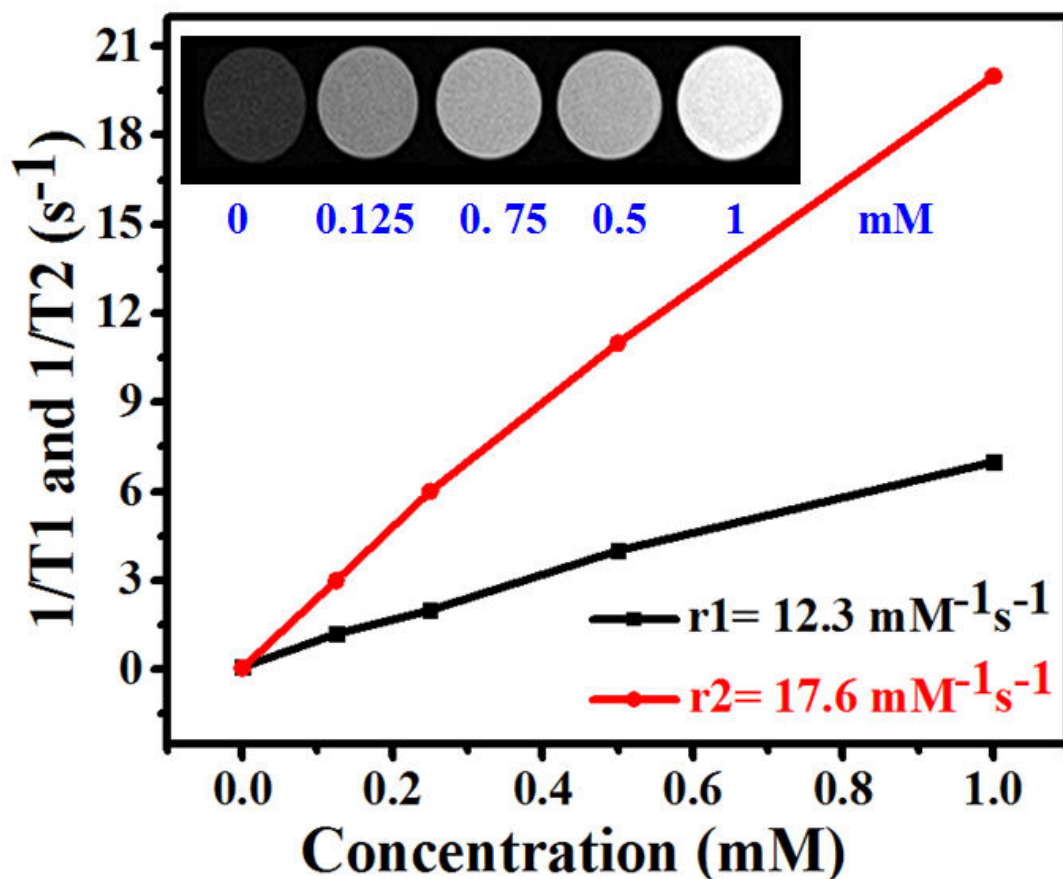


Fig. 5.7: Relaxivity measurements of *in-situ* photodegraded PVP coated Gd₂O₃ nanoparticles.

5.4 Conclusion

We have fabricated surface modified Gd₂O₃ nanoparticles. Our results show that while long chain BSA conjugated Gd₂O₃ nanoparticles render better biocompatibility of upto 99.6% cell viability and 1.2% haemolysis, TA capped Gd₂O₃ nanoparticles give better MR contrast of $r1$ value $3.3 \text{ mM}^{-1}\text{s}^{-1}$ due to the easy availability of surface gadolinium. The values are almost as good as commercially available MRI contrast agents. BSA conjugated Gd₂O₃

nanoparticles can be further manipulated to enhance the relaxivity so as to serve as a good organic image contrast agent.

In later part of our studies, we coated the as-synthesized Gd₂O₃ nanoparticles with *in-situ* photodegraded PVP. This gave better r₁ relaxivity of 12.3 mM⁻¹s⁻¹. Since PVP coating has shown good biocompatibility in our previous studies, breaking the polymer chain *in-situ* gives a better edge to it, as it reduces the T₁ relaxation time. The photodegraded PVP coated Gd₂O₃ nanoparticles have a cell viability upto 99%.

CHAPTER 6: $\text{Fe}_3\text{O}_4\text{-Gd}_2\text{O}_3$ Nanoclusters for Magnetic Hyperthermia and MRI Applications

6.1 Introduction

Our previous chapters have discussed the potential application of iron oxide (Fe₃O₄) nanoparticles in magnetic hyperthermia based cancer therapy and gadolinium oxide (Gd₂O₃) nanoparticles for MR imaging. In this chapter we tried to combine the advantages of both the metal oxide nanoparticles to get a combinatorial edge of the same for a theranostic approach. Therefore we have synthesized iron oxide- gadolinium oxide (Fe₃O₄-Gd₂O₃) nanoclusters in order to enhance the T1 and T2 relaxivity for better MR imaging and also explore the magnetic hyperthermia properties of the same.

As discussed extensively in previous chapters, iron oxide (Fe₃O₄) nanoparticles have been used as useful platform material for multitude of biomedical applications like magnetic drug targeting, biomolecule separation, and hyperthermal cancer therapy [214, 215]. Also gadolinium oxide (Gd₂O₃) nanoparticles have been used as a potential MRI contrast agent [216, 217]. Magnetic resonance imaging (MRI) is a powerful non-invasive diagnostic technique to visualize the fine features of human body in a high spatial resolution [218]. MR contrast agents facilitate the achievement of clear images for accurate diagnosis, by exerting an influence on the longitudinal (T1) or transverse (T2) relaxation time of the surrounding tissue. Paramagnetic complexes containing gadolinium (Gd³⁺) or manganese (Mn²⁺) ions induce local relaxation change of the adjacent water protons and reduce T1, providing positive contrast (bright signal) on T1- weighted MR image.

Similarly superparamagnetic magnetite nanoparticles, due to their strong T_2 shortening effect [219, 220], have been widely used as an ultrasensitive negative contrast agents for stem cell tracking and early stage cancer detection. Still, their clinical applications are limited due to the negative contrast effect and magnetic susceptibility artifacts. This is because, the dark areas of their negative contrast is often confused with a low-level MR signal arising from the nearby adjacent tissues [221, 222]. Adding to it, susceptibility artifacts can also occur as a result of the steep variation of local magnetic field around superparamagnetic magnetite nanoparticles, leading to the locally distorted anatomy of surrounding tissue in MR image [223]. In order to utilize the best of both the worlds, in this chapter we have discussed the synthesis of iron oxide- gadolinium oxide (Io-Go) nanoclusters to demonstrate their utility as dual contrast agents for T_1 - and T_2 -weighted MRI. Magnetic hyperthermia is a potential cancer treatment strategy to cure cancer by increasing the temperature of the tumor site upto 42°C. The increase in temperature raise causes cell death due to apoptosis and necrosis. Iron oxide (Fe₃O₄) nanoparticles are FDA approved nanomaterials which have been widely used in magnetic hyperthermia.

We have fabricated hydrophilic Io-Go nanoclusters by coating the same with polydopamine. Since our previous studies showed that thioglycolic acid capped Gd₂O₃ nanoparticles showed improved T_1 relaxivity, we have used the same as an anchoring material for dopamine polymerization.

Dopamine (DA), is the most important neurotransmitters. It can self-polymerize to polydopamine (PDA) at alkaline pH and can spontaneously deposit on any surface to form a conformal layer [224]. Also, PDA is stable and biocompatible in vivo [225], Making it viable for biomedical applications. Additionally, the existence of functional groups like catechol and amine on the surface of PDA promotes the binding of various biomolecules [226]. In the recent advances, PDA has been used as a photothermal therapeutic agent for in vivo cancer therapy due to its strong near-infrared (NIR) absorption and high photothermal conversion efficiency of upto 40% [227].

The Fe₃O₄-Gd₂O₃ nanoclusters are expected to induce a simultaneous positive and negative contrast enhancement making them useful as dual-functional MRI contrast agents [228]. Depending on the tissue site of interest, Fe₃O₄-Gd₂O₃ nanoclusters can be selectively visualized by *T1*- or *T2*-weighted MRI in order to achieve complementary information that cannot be obtained by the use of just one type of contrast agent, thereby giving a more precise diagnosis. Our nanoclusters also serve as potential magnetic hyperthermia agents due to the presence of Fe₃O₄ nanoparticles. A schematic overview of the multifunctional Io-Go nanoclusters is shown in Fig. 6.1.

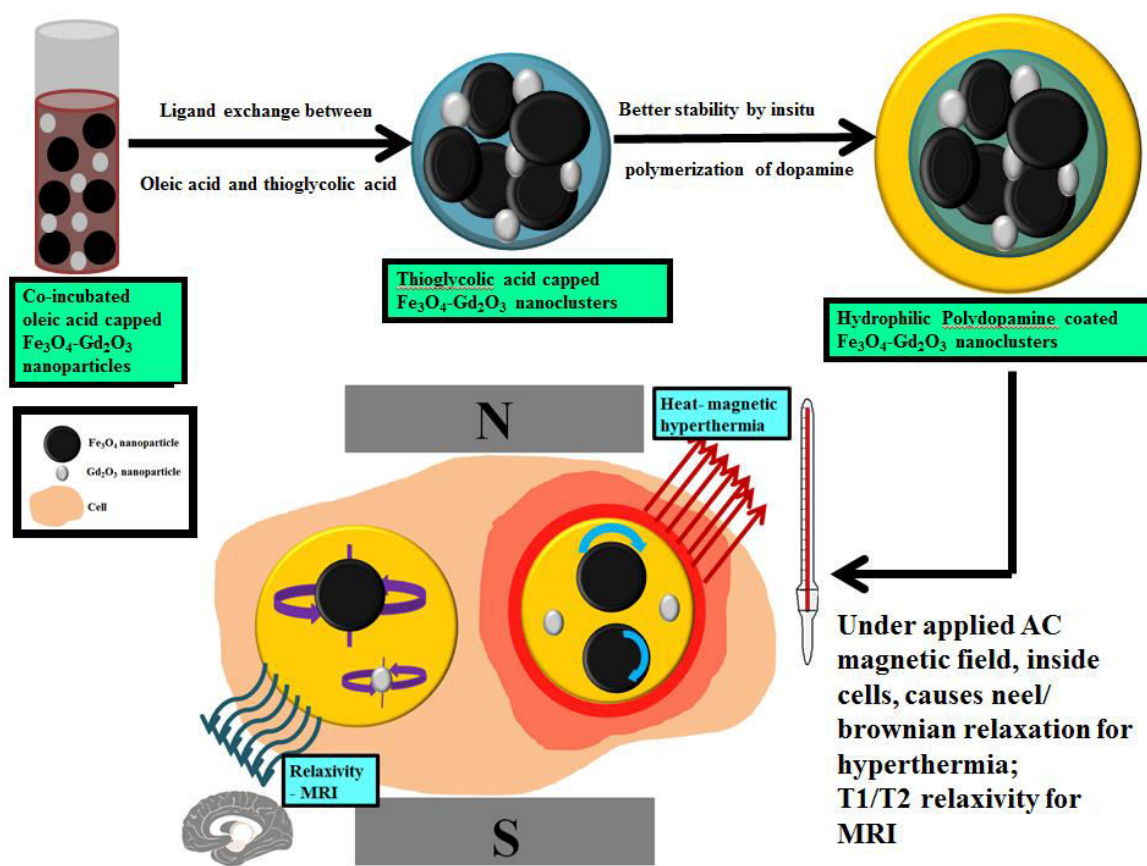


Fig. 6.1: Schematic overview of the PDA coated $\text{Fe}_3\text{O}_4\text{-Gd}_2\text{O}_3$ nanoclusters as multifunctional platform for magnetic hyperthermia and MRI applications.

6.2 Methods

Cell viability of PDA coated $\text{Fe}_3\text{O}_4\text{-Gd}_2\text{O}_3$ nanoclusters

The BHK cells suspended in 1xPBS were co-incubated with 100 $\mu\text{g/mL}$ of $\text{Fe}_3\text{O}_4\text{-Gd}_2\text{O}_3$ nanoclusters and PDA coated $\text{Fe}_3\text{O}_4\text{-Gd}_2\text{O}_3$ nanoclusters for 24 hours at 37°C. The BHK cells after incubation were run under flow cyclometry. Dyes NucBlue (ThermoFischer Scientific) to stain the total nuclei of cells, AlexaFluor (Invitrogen) to stain the apoptotic cells green and

Propidium Iodide (PI-ThermoFischer Scientific) to stain the nucleus of dead cells red were used to qualitatively visualize the cells.

Briefly, to 1 mm² of the BHK cells, 2 drops of NucBlue, 2.5 µL of AlexaFluor and 0.5 µL of PI were added along with 100 µL binding buffer and were incubated at room temperature for 15 minutes. The reaction was stopped by adding excess binding buffer and the samples were run in flow cytometry. In the histogram comprises of 4 quadrants. Quadrant 1 (Q1) represents cells that have under gone complete necrosis; Quadrant 2 (Q2) represents cells at late stage apoptosis, wherein the cell membrane has ruptured; Quadrant 3 (Q3) represents cells at early stage apoptosis; Quadrant 4 (Q4) represents live cells. Later the BHK cells after incubation were observed under confocal microscope (Olympus-FluoView, FV1000). The images were processed using IMARIS 8.0 software.

Magnetic Hyperthermia of PDA coated Fe₃O₄-Gd₂O₃ nanoclusters

The magnetic hyperthermia studies, to calculate the Specific Absorption Rate (SAR) were carried out by placing the 0.1mg/mL (Fe³⁺ concentration) Fe₃O₄-Gd₂O₃ nanoclusters inside a copper coil generating an external AC magnetic field. The temperature raise of the sample with respect to the time of exposure of the sample to an AC magnetic field at an amplitude of 32.4 kAm⁻¹, frequency of 360 kHz and a magnetic field of 600 Oe was investigated. SAR is expressed as the heat released by the magnetic iron

oxide nanoparticles under a magnetic field. The SAR value is calculated from the formula,

$$SAR = C_{wat} \frac{\Delta T}{\Delta t} * \frac{1}{C_{Fe}} (Wg^{-1})$$

Where, C_{wat}- specific heat of the medium (distilled water), 4.18 J /g/ °C; ΔT/Δt- The initial slope of the time-dependent temperature curve; C_{Fe}- concentration of ferric ions in the medium, 0.1mg/mL. The concentration of ferric ions in the samples was determined using ICP-OES analysis (Perkin-Elmer Dual view Optima 5300 DV ICPOES system).

Magnetic hyperthermia treatment on SEM leukemia cell lines

SEM leukemia cell lines which cause Acute Lymphoblastic Leukemia (ALL). SEM leukemia cell lines of concentration 10000 cells were used to study the efficiency of the Io-Go nanoclusters against leukemia cell lines. The SEM cells were co-incubated with 0.1 mg/mL (Fe³⁺ concentration) Fe₃O₄-Gd₂O₃ nanoclusters for 3 hours at 37°C. SEM leukemia cell lines suspended in 1xPBS was maintained as control. After the incubation period, the sample and the control were subjected to an applied AC magnetic field of 600 Oe (frequency 360 kHz), to bring a ΔT of upto 42°C-45°C. At the end of the magnetic hyperthermia treatment, the sample and the control were run in a flow cyclometry set-up. Dyes NucBlue (ThermoFischer Scientific) to stain the total nuclei of cells, AlexaFluor (Invitrogen) to stain the apoptotic cells green and Propidium Iodide (PI-ThermoFischer Scientific) to stain the nucleus of dead cells red were used to qualitatively visualize the cells.

Briefly, to 1 mm² of the BHK cells, 2 drops of NucBlue, 2.5 µL of AlexaFluor and 0.5 µL of PI were added along with 100 µL binding buffer and were incubated at room temperature for 15 minutes. The reaction was stopped by adding excess binding buffer and the samples were run in flow cytometry. In the histogram comprises of 4 quadrants. Quadrant 1 (Q1) represents cells that have under gone complete necrosis; Quadrant 2 (Q2) represents cells at late stage apoptosis, wherein the cell membrane has ruptured; Quadrant 3 (Q3) represents cells at early stage apoptosis; Quadrant 4 (Q4) represents live cells.

Relaxivity measurements of PDA coated Fe₃O₄-Gd₂O₃ nanoclusters

Iron oxide- gadolinium oxide (Fe₃O₄-Gd₂O₃) nanoclusters were fabricated and made hydrophilic by the *in-situ* polymerization of dopamine. The samples were well dispersed and stable in water. The concentration of Gd³⁺ and Fe³⁺ ions in the sample were 3mM each. The samples were diluted to 5 different concentrations (3 mM, 1.5 mM, 0.75 mM, 0.37 mM and 0 mM). The longitudinal (r1) and transverse (r2) relaxivities were measured using a 7T Bruker ClinScan with a Siemens interface and 72 mm volume coil. T1 measurement was done using an inversion-recovery sequence; TR/TE = 5000/7; Average=3; flip angle = 90° and inversion-times (TIs) =31, 150, 300, 700, 1200, 1800, 2400, 3000, 3600, 4000, 4500 and 4900 ms. T1 was calculated from the inversion-recovery images, by fitting for the decay curve. T2 measurement was performed using a multiple spin echo sequence TR =

5000 ms; TE = 12.9; NE = 14. The sample was maintained at 36°C using a water bath. T2 maps were obtained along with the inline acquisition sequence program. The r1 and r2 values were obtained from slope of the linear fit between 1/T1 or 1/T2 vs concentration of contrast agent in mM. The relaxivity is represented as mM⁻¹s⁻¹ ± SD (n = 3).

6.3 Results and Discussion

Synthesis and hydrophilic phase transfer of Fe₃O₄-Gd₂O₃ nanoclusters

Fig. 6.2(a-i) and 6.2(a-ii) shows the TEM image and SAED pattern of as-synthesized Fe₃O₄ nanoparticles and Gd₂O₃ nanoparticles respectively. As seen from TEM images, the Fe₃O₄ nanoparticles are of 20 ± 2 nm in size and the Gd₂O₃ nanoparticles are ultra-small of average size 3 ± 1 nm. The inset SAED image of Fig. 6.2(a-i) shows spinel Fe₃O₄ corresponding to (111), (220), (311), (400), (422), (511), (440) and (533). The inset SAED image of Fig. 6.2(a-ii) shows Gd₂O₃ corresponding to (222), (440) and (664). Fig 2(a-iii) shows the physical mixture of iron oxide- gadolinium oxide (Io-Go) nanoclusters before converting to hydrophilic phase. The SAED pattern corresponding to (220), (311), (400), (440) and (664) also confirms the same. Fig. 6.2(b) shows that the magnetization (Ms) of Iron oxide- gadolinium oxide (Fe₃O₄-Gd₂O₃) nanoclusters, decreases to 62 emu/g when compared to 75 emu/g of

Fe_3O_4 nanoparticles. This is due to the addition of Gd_2O_3 nanoparticles. Inset figure shows the mild coercivity exhibited by Fe_3O_4 , which makes it a good magnetic hyperthermia agent.

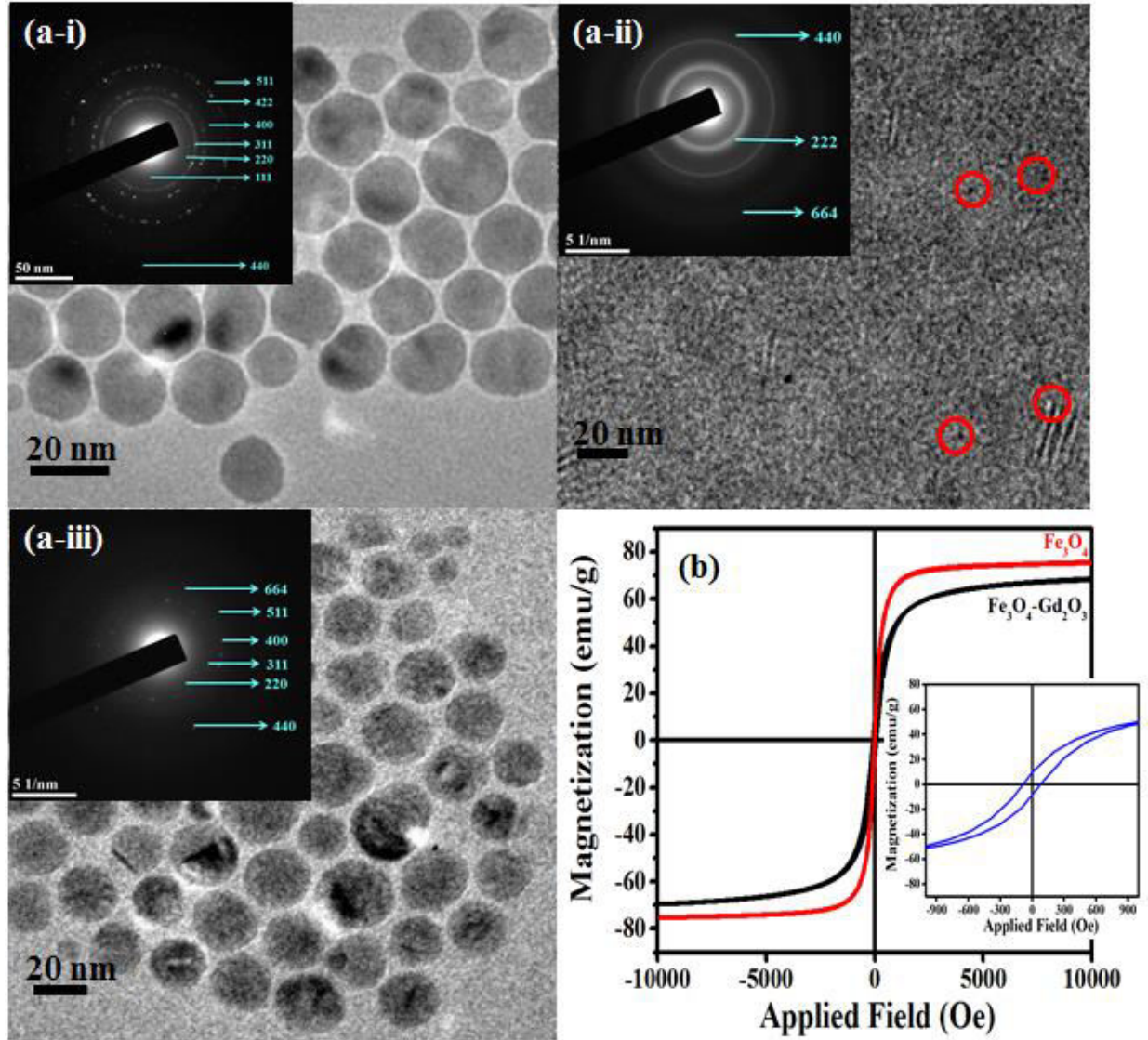


Fig. 6.2: Characterization of as-synthesized Io-Go nanoclusters (a-i) TEM image of 20 nm Fe_3O_4 nanoparticles. Inset image is the SAED pattern (a-ii) TEM image of 3 nm Gd_2O_3 nanoparticles. Inset image is the SAED pattern (a-iii) TEM image of Io-Go nanoclusters. Inset image is the SAED pattern (b) saturation magnetization (M_s) of Io-Go nanoclusters. Inset image shows the coercivity of 20 nm Fe_3O_4 nanoparticles.

The as-synthesized nanoclusters were made hydrophilic by ligand exchange using thioglycolic acid. The carboxy group of thioglycolic acid capped Fe₃O₄-Gd₂O₃ nanoclusters were later incubated in dopamine for *insitu* polymerization. Fig. 6.3(a) shows that the Gd₂O₃ nanoparticles and Fe₃O₄ nanoparticles were clustered together within PDA. Gd₂O₃ nanoparticles are well decorated over the Fe₃O₄ nanoparticles as seen from the figure. Fig. 6.3(b) shows the SAED pattern corresponding to (220), (311), (400), (440) and (664) of the PDA coated Fe₃O₄-Gd₂O₃ nanoclusters. Fig. 6.3(c) shows the EDAX spectrum of Io-Go nanoclusters. It shows the weight % of Fe-Gd is almost 1:1 (53%: 47%). Inset table gives the quantitative measurement of the same. The PDA coated Fe₃O₄-Gd₂O₃ nanoclusters were well-dispersed and were stable in water. This is evident from Fig. 6.3(d). The average hydrodynamic radius of the PDA coated Fe₃O₄-Gd₂O₃ nanoclusters is 40±2 nm. Fig. 6.4(e) confirms the dopamine polymerization on Fe₃O₄-Gd₂O₃ nanoclusters. Dopamine has no absorbance peak between 300-900 nm. Whereas polydopamine coated Fe₃O₄-Gd₂O₃ nanoclusters show a characteristic peak around 400-500 nm, confirming the in-situ polymerization of dopamine on the Io-Go nanoclusters.

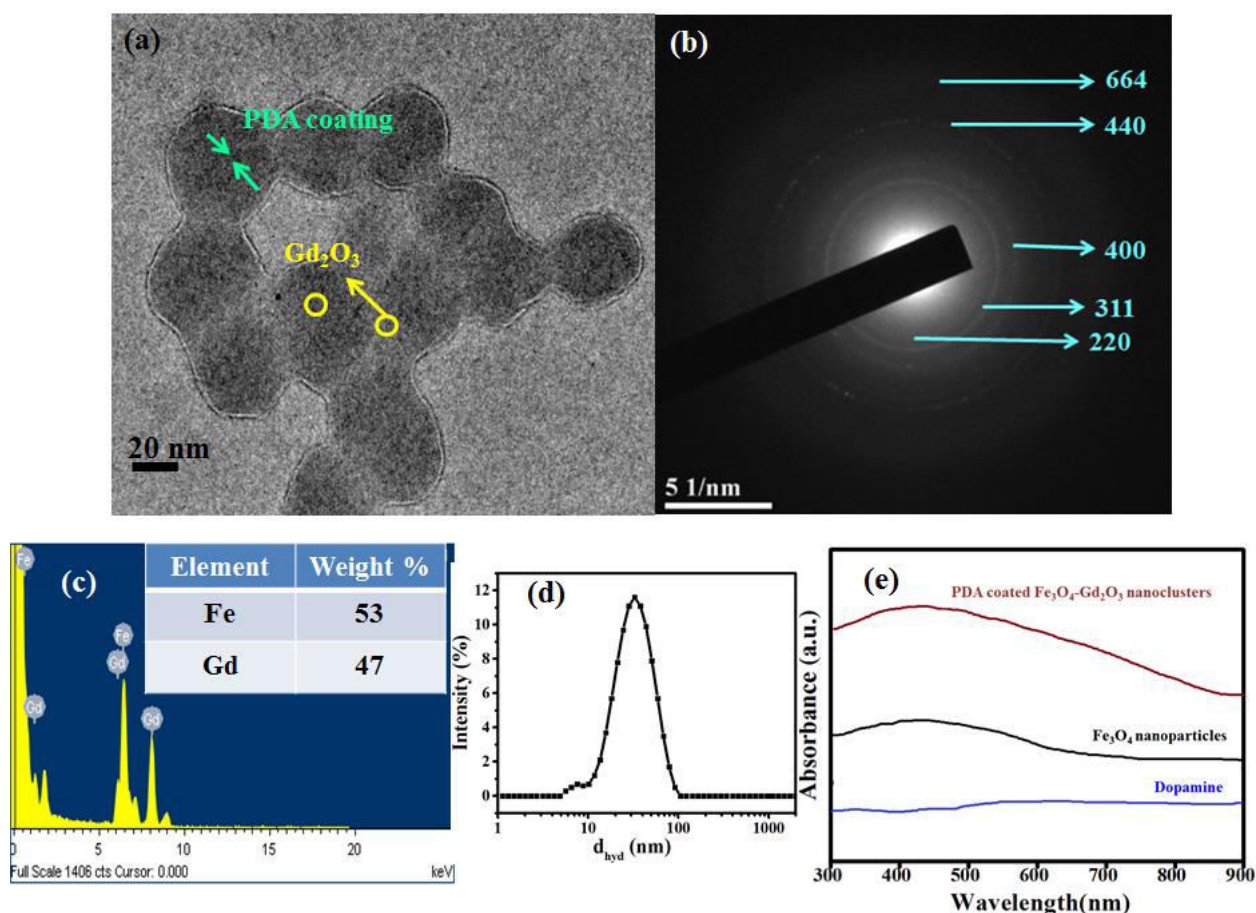


Fig. 6.3: Hydrophilic phase transfer of Fe_3O_4 nanoparticle (a) TEM image of PDA coated $\text{Fe}_3\text{O}_4\text{-Gd}_2\text{O}_3$ nanoclusters shows that the Gd_2O_3 nanoparticles are decorated over Fe_3O_4 nanoparticles and coated with PDA (b) SAED pattern of $\text{Fe}_3\text{O}_4\text{-Gd}_2\text{O}_3$ nanoclusters (c) EDAX spectrum of $\text{Fe}_3\text{O}_4\text{-Gd}_2\text{O}_3$ nanoclusters (d) Average hydrodynamic radius of PDA coated $\text{Fe}_3\text{O}_4\text{-Gd}_2\text{O}_3$ nanoclusters (e) UV-Vis spectrum of PDA coated $\text{Fe}_3\text{O}_4\text{-Gd}_2\text{O}_3$ nanoclusters.

Cell viability of PDA coated Io-Go nanoclusters

The cell viability of $\text{Fe}_3\text{O}_4\text{-Gd}_2\text{O}_3$ nanoclusters is 97% when compared to 98% of PDA coated $\text{Fe}_3\text{O}_4\text{-Gd}_2\text{O}_3$ nanoclusters as seen from the Fig. 6.4(a) and 6.4(b) respectively. From Fig. 6.4(b) it is evident that there is fewer cells in early stage apoptosis (Q3) when compared to that of Fig. 6.4(a). This shows

that PDA coated Fe₃O₄-Gd₂O₃ nanoclusters exhibit less or no cytotoxicity to healthy BHK cells. Therefore PDA coating render biocompatibility to the Io-Go nanoclusters and hence make them a promising candidates for magnetic hyperthermia and MRI applications.

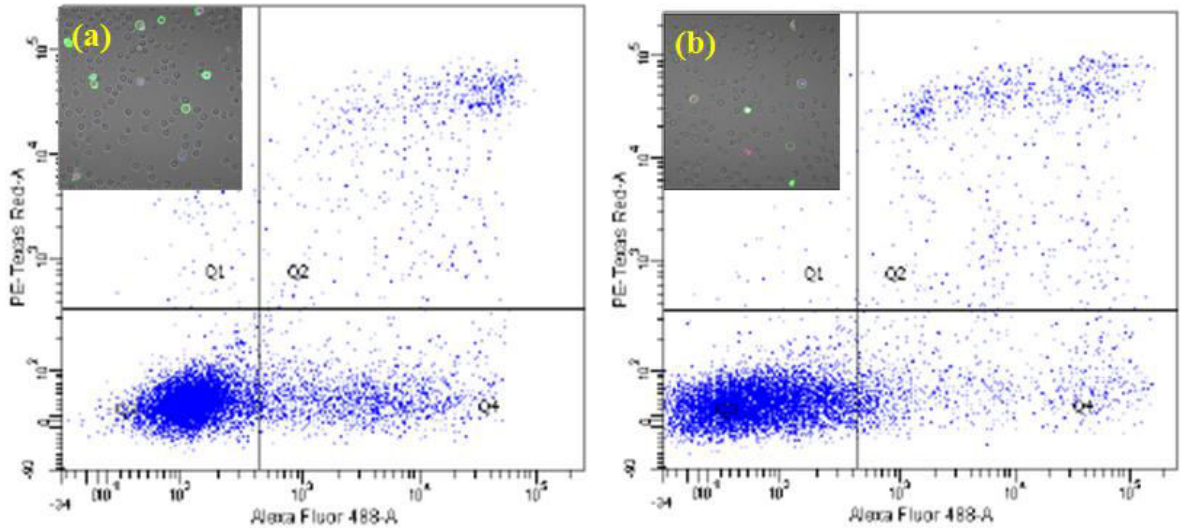


Fig. 6.4: Cell viability studies of (a) Io-Go nanoclusters-97 % (b) PDA coated Fe₃O₄-Gd₂O₃ nanoclusters- 98 %.

Magnetic hyperthermia of PDA coated Fe₃O₄-Gd₂O₃ nanoclusters

Fig. 6.5 shows the comparison of temperature raise (ΔT) curves due to the PDA coated Fe₃O₄ nanoparticles and PDA coated Fe₃O₄-Gd₂O₃ nanoclusters. The decoration with Gd₂O₃ nanoparticles decreases the temperature raise (ΔT) to 4.2°C, when compared to 7°C of PDA coated Fe₃O₄ nanoparticles. As seen from the inset figure, the SAR value of Fe₃O₄-Gd₂O₃ nanoclusters is 785 W/g also slightly lower than that of PDA coated Fe₃O₄ nanoparticles, which is 920 W/g. This is decrease in SAR value is expected and is well within the statistical

error range. Therefore it does not much affect the heating efficiency of PDA coated $\text{Fe}_3\text{O}_4\text{-Gd}_2\text{O}_3$ nanoclusters. The SAR value of PDA coated $\text{Fe}_3\text{O}_4\text{-Gd}_2\text{O}_3$ nanoclusters is comparable with our previous results for good magnetic hyperthermia agent.

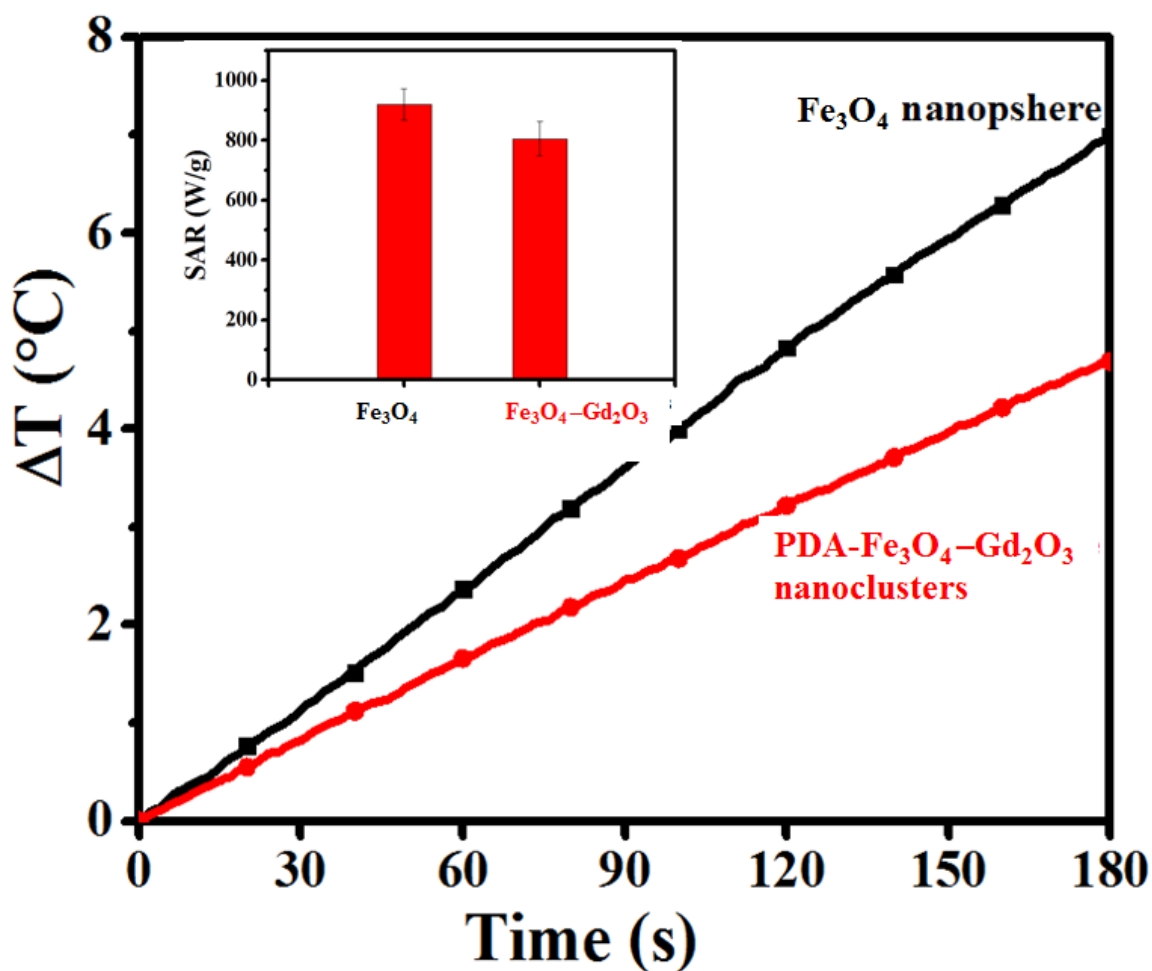


Fig. 6.5: Temperature raise comparison between PDA coated Fe_3O_4 nanoparticles and PDA coated $\text{Fe}_3\text{O}_4\text{-Gd}_2\text{O}_3$ nanoclusters. Inset figure is the SAR value comparison of the same.

Fig. 6.6(a) shows the histogram of untreated SEM leukemia cell lines. It is obvious from the histograms that the application of AC magnetic field alone

without $\text{Fe}_3\text{O}_4\text{-Gd}_2\text{O}_3$ nanoclusters, causes almost no damage (97.8 %) to the tumor cell line. Whereas the application of 600 Oe magnetic field along with 0.1 mg/mL (Fe^{3+} concentration) of Io-Go nanoclusters raises the temperature upto 45°C causing tumor cell death leading to 74 % as shown in Fig. 6.6(b). It is very clear from Fig. 6.6(b) that there are more cells entering late stage apoptosis (Q2) and complete necrosis (Q1). Thus the fabricated $\text{Fe}_3\text{O}_4\text{-Gd}_2\text{O}_3$ nanoclusters are very good magnetic hyperthermia agents.

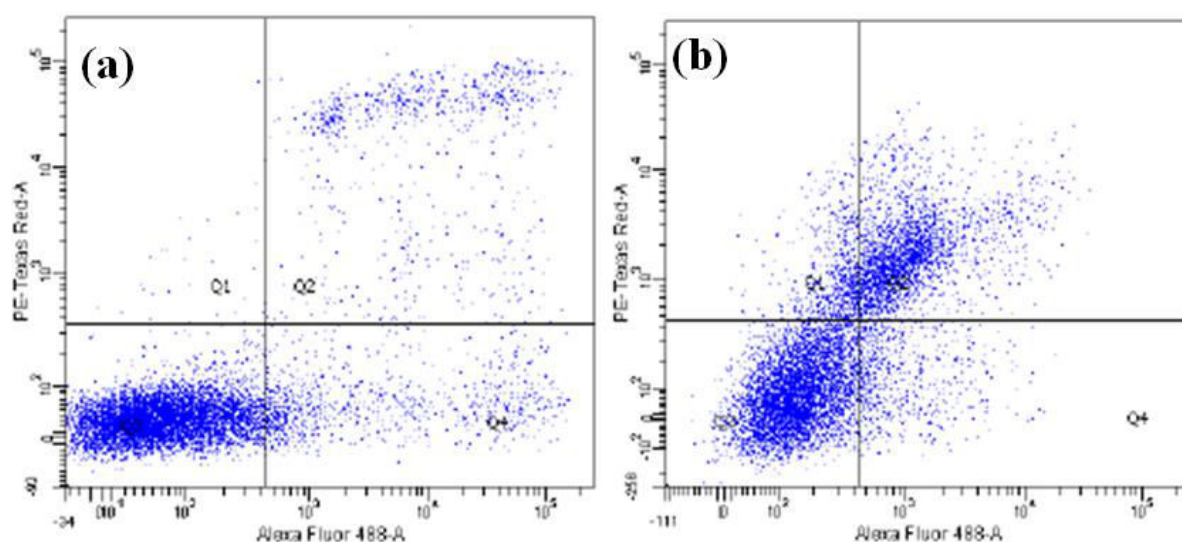


Fig. 6.6: Magnetic hyperthermia treatment on SEM leukemia cell line using PDA coated $\text{Fe}_3\text{O}_4\text{-Gd}_2\text{O}_3$ nanoclusters a) Cell line before treatment- 97.8% viability b) Cell line after treatment- 74% viability.

Relaxivity studies of PDA coated $\text{Fe}_3\text{O}_4\text{-Gd}_2\text{O}_3$ nanoclusters

To be an effective T1 contrast agent, the nanoparticles are expected to have hydrophilic coating surface, to ensure that a large quantity of Gd_2O_3 nanoparticles directly interact with the surrounding protons. Our PDA coated

Fe₃O₄-Gd₂O₃ nanoclusters have Gd₂O₃ nanoparticles decorated over the Fe₃O₄ nanoparticles and hence are readily available for proton interaction. As expected, Fig. 6.7 PDA Fe₃O₄-Gd₂O₃ nanoclusters show a r1 value of 5.8 mM⁻¹s⁻¹ and r2 value of 6.7 mM⁻¹s⁻¹. Moreover the polar groups in each nanocluster allows the water molecules to pass through the coating layer and interact with Gd₂O₃ nanoparticles and Fe₃O₄ nanoparticles which could the reduced T1 and T2 relaxation time. The inset phantom images of PDA coated Fe₃O₄-Gd₂O₃ nanoclusters at different concentrations clearly demonstrated their contrast difference as dual contrast agents.

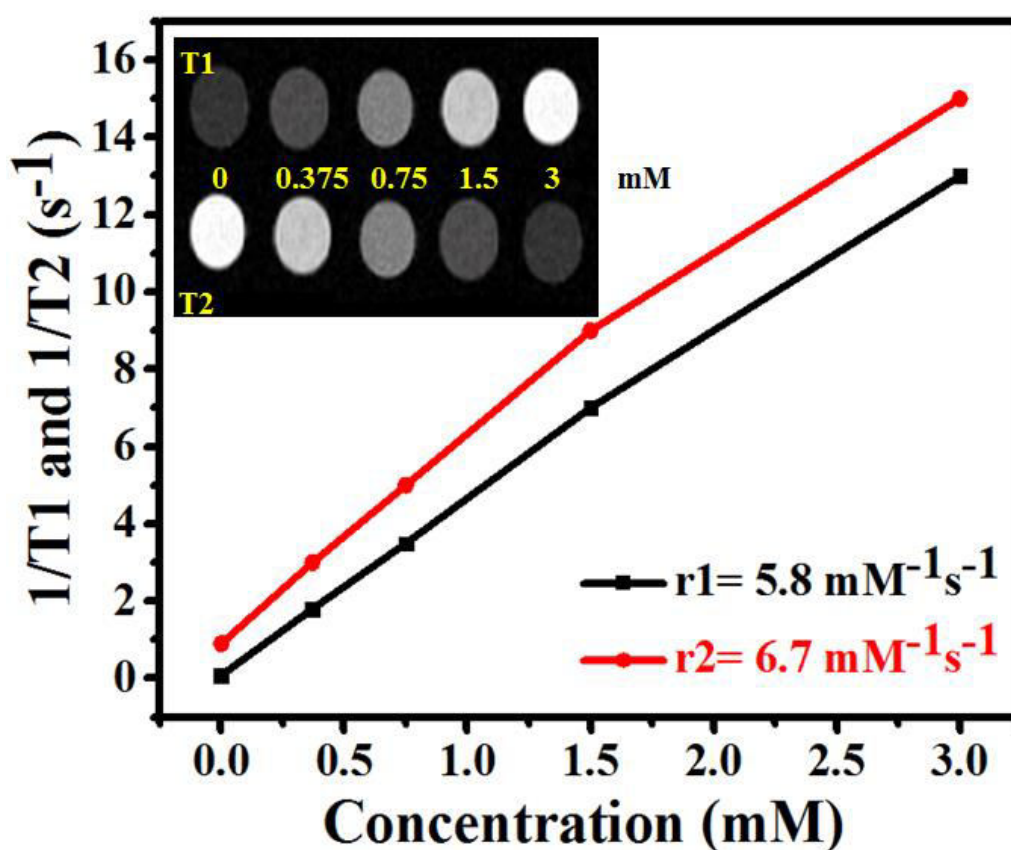


Fig. 6.7: Plots of 1/T1 and 1/T2 as a function of Gd and Fe concentration. Inset images shows the corresponding phantom images of Fe₃O₄-Gd₂O₃ nanoclusters corresponding to Gd+Fe concentration in mM.

6.4 Conclusion

We have successfully fabricated PDA coated iron oxide- gadolinium oxide (Fe₃O₄-Gd₂O₃) nanoclusters which can be used as a multifunctional platform for magnetic hyperthermia and dual mode MRI imaging. This gives the nanoclusters a theranostic value. The PDA coated Fe₃O₄-Gd₂O₃ nanoclusters show effective magnetic hyperthermia properties (of SAR value 920 W/g) without compromising on the tissue viability. It also shows significant tumor necrosis of upto 74%, making it a very good magnetic hyperthermia agent. Since the tissue viability of PDA coated Fe₃O₄-Gd₂O₃ nanoclusters is significant, it also is a safe biocompatible agent under the field used for MRI. The T1 and T2 relaxivity measurements of give r1 and r2 values of 5.8 mM⁻¹s⁻¹ and 6.7 mM⁻¹s⁻¹ respectively making our PDA coated Fe₃O₄-Gd₂O₃ nanoclusters, a potential dual contrast agent for MRI applications. Though the scope of PDA coated Fe₃O₄-Gd₂O₃ nanoclusters as photothermal agents, is beyond the scope of this chapter, exploration of the same is a potential future application of the same.

Chapter 7: Conclusions and Future works

7.1 Conclusions

This thesis discusses about the fabrication of magnetic metal oxide (Fe_3O_4 , Gd_2O_3) nanoparticles and their application in cancer theranostics, viz, magnetic hyperthermia and magnetic resonance imaging. We have also discussed the influence of physiology on magnetic hyperthermia.

- 1) In chapter 2 we have discussed the synthesis of various magnetic metal oxides nanoparticles by thermal decomposition method. Thermal decomposition method yields uniform and monodisperse particles. The as-synthesized, oleic acid capped, hydrophobic nanoparticles were converted to hydrophilic and biocompatible phase by various methods- surface modification (CTAB, PEI), ligand exchange (APTMS, TA, PVP) in-situ polymerization (dopamine) and bioconjugation (BSA). This chapter also explores the characterization techniques used to characterize the particles at various stages of experiments.
- 2) In chapter 3 we have discussed the fabrication of hydrophilic Fe_3O_4 nanoparticles of different size, shape, composition and surface modification. Among the 10 nm superparamagnetic iron oxide nanoparticles (SPIONs) and 30 nm ferrimagnetic iron oxide nanoparticles (FIONs), FIONs have higher magnetic saturation of 87 emu/g and hence show higher SAR value of 1700 W/g, irrespective of the surface modifying agent used. APTMS capping showed better stability when compared to

CTAB or PEI coating. Hence APTMS was further used in our hydrophilic phase transfer experiments. Also 30 nm Fe_3O_4 nanoparticles also have optimum size for biological applications. Both 10 nm and 30 nm Fe_3O_4 nanoparticles show very high cell viability of upto 99%. We had fabricated hydrophilic nanospheres, nanohexagons and nanotetragons of 20 nm size. Nanotetragons were found to show polydispersity and also exhibited high magnetic hyperthermia efficiency of 1800 W/g. Composition of the Fe_3O_4 nanoparticles were modified by doping with divalent ions like cobalt and nickel. CoFe_2O_4 nanoparticles of size 15 nm show higher coercivity and hence higher SAR value of 885 W/g when compared to 15 nm Fe_3O_4 nanoparticles and 150 nm NiFe_2O_4 nanoparticles. This chapter gives the preliminary insights into fabrication of different types of Fe_3O_4 nanoparticles for magnetic hyperthermia applications. Hydrophilic phase transfer improves the colloidal stability of nanoparticles. But improving the biocompatibility enhances the potential chance of the nanoparticles for biomedical applications. Therefore in the later section of chapter 3, we have discussed the fabrication of albumin conjugated 30 nm Fe_3O_4 nanoparticles. Bovine Serum Albumin (BSA) conjugation has found to enhance both the biocompatibility and the heating efficiency of the Fe_3O_4 nanoparticles. We have conjugated BSA over surface modified Fe_3O_4 nanoparticles by physical adsorption method using CTAB and covalent amide bond formation by APTMS. Albumin is the most abundant protein present in blood plasma and hence it offers better stealth characteristics. This is proved by haemolytic studies and cell viability studies using BHK cell lines. The cell viability is upto 99.5% after BSA conjugation. BSA

conjugation also renders better stability and prevents aggregation of Fe_3O_4 nanoparticles in water, thus enhancing the heating efficiency upto 2300 W/g. Magnetic hyperthermia treatment of BSA conjugated FIONs show better efficiency on liver tissue excised from 5 weeks old male Witstar rats when compared to the non-conjugated Fe_3O_4 nanoparticle. Thus we propose a single combinatorial approach for improved biocompatibility and enhanced magnetic hyperthermia performance.

- 3) Various physical and chemical parameters like size, shape, anisotropy, composition, applied magnetic field etc., influence the magnetic hyperthermia efficiency of magnetic nanoparticles. In chapter 4 we have attempted to explore the basic properties of Fe_3O_4 nanoparticles once inside a biosystem. While physiological ions enhance the heating efficiency of 10 nm SPIONs due to their motility, the physiological proteins and cells present in blood plasma, restrict the mobility of the ions, thereby retarding the heating efficiency of the SPIONs. Thus acting as biosafety agents. Therefore the adverse effects of magnetic nanoparticles on a biosystem is under check. We have also found that AC magnetic field at therapeutic range does not cause damage to the tissue, thus confirming that magnetic hyperthermia effect is brought about by SPIONs under the influence AC magnetic field. This study throws basic insights into the fundamentals of magnetic hyperthermia inside physiology. This study throws light into the basic scientific explanation behind the tissue viability under the AC magnetic field, despite the increase in temperature. Thus it gives future

directions for the fabrication of better magnetic nanoparticles for effective magnetic hyperthermia.

- 4) Chapter 5 explores the application of Gd_2O_3 nanoparticles as potential T1 contrast agents for MRI diagnostic applications. We have compared the relaxivity values between TA capped Gd_2O_3 nanoparticles and BSA conjugated Gd_2O_3 nanoparticles. While BSA conjugated Gd_2O_3 nanoparticles show a r_1 of $2.8 \text{ mM}^{-1}\text{s}^{-1}$ when compared to $3.3 \text{ mM}^{-1}\text{s}^{-1}$ they show a very good cell viability of upto 99.6% and 1.2% haemolysis. The later section of this chapter discusses the coating of inorganic, *in-situ* photodegraded PVP coating over Gd_2O_3 nanoparticles. This technique gave better contrast of relaxivity value $12.3 \text{ mM}^{-1}\text{s}^{-1}$ owing to the availability of gadolinium ions for relaxation. The cell viability is also extremely good, as much as 99 %.

- 5) Chapter 6 discusses the fabrication of iron oxide-gadolinium oxide (Io-Go) nanoclusters which can be used as a multifunctional platform for magnetic hyperthermia and dual mode MRI imaging. The PDA coated Io-Go nanoclusters show effective magnetic hyperthermia of upto 920 W/g without compromising on the cell viability (98%). It also shows significant tumor necrosis of SEM leukemia cell lines upto 74%, making it a very good magnetic hyperthermia agent. PDA coated Io-Go nanoclusters are also found to act as good T1 and T2 dual contrast agents showing a good r_1 value of $5.8 \text{ mM}^{-1}\text{s}^{-1}$ and r_2 value of $6.7 \text{ mM}^{-1}\text{s}^{-1}$ for MRI applications.

7.2 Future works

- 1) In chapter 3, we have synthesized monodisperse 10 nm and 30 nm Fe_3O_4 nanoparticles. In future Fe_3O_4 nanoparticles of more size ranges can be fabricated to study the trend of the effect of size on SAR value of Fe_3O_4 nanoparticles. Also more shapes with uniform size can be fabricated. The physics behind the magnetic properties can be further explored. Simulation studies to support the experimental results can be done. Also the results in the last section of chapter 3 prove that conjugation of physiological proteins improve the stealth and heating properties of Fe_3O_4 nanoparticles. Though we have studied the cell viability and magnetic hyperthermia of the performance of the BSA conjugated Fe_3O_4 nanoparticles *in vitro*, exploring the blood circulation time of the particles and magnetic hyperthermia performance of the particles *in vivo* can be a next big step in confirming the efficacy of the single combinatorial approach.
- 2) Exploring the *in vivo* magnetic hyperthermia performance of BSA conjugated Gd_2O_3 nanoparticles discussed in chapter 5, which have proven to show good biocompatibility and relaxivity values is a future work. Since *in-situ* PVP coating has shown very good relaxivity values, the *in vivo* MRI properties have to be better understood.

- 3) In chapter 6 we have discussed the fabrication of PDA coated Io-Go nanoclusters. The nanoclusters have proven to have good magnetic hyperthermia and dual contrast properties, *in vitro*. But exploring the MRI application of the Io-Go nanoclusters *in vivo* is a much needed extension of the work. The *in vivo* magnetic hyperthermia performance for tumor retardation can also be studied in the future, to develop the same as a complete multifunctional platform for cancer therapy, as in magnetic hyperthermia and diagnostics a sin MR imaging, thus making Io-Go nanoclusters as potential theranostics agents. Though the photothermal therapy of due to Polydopamine is beyond the scope of this thesis, the same can be further explored in future.

References

1. Berry C.C , et al. *J Phys D: Appl. Phys*, **2003**, 36, 198–206.
2. Chen Q et al. *Appl. Phys. Lett.*, **1998**, 73, 3156.
3. Callister WD. *Materials Science and Engineering*, Wiley: New York, **2003**.
4. Vijayalakshimi A et al. *J. Appl. Phys.*, **1998**, 83, 400.
5. Shafi K. V. P. M. et al. *Nanostruct. Mater.*, **1999**, 12, 29.
6. Chikazumi S et al. *Physics of Ferromagnetism*, Oxford University Press, Oxford, U.K., **1997**.
7. O’Handley R. C. *Modern Magnetic Materials: Principles and Applications*, Wiley, New York, NY, **2000**.
8. Coey J. M. D. *Magnetism and Magnetic Materials*, Cambridge University Press, New York, NY, **2010**.
9. Fang Q et al. *J. Magn. Magn. Mater.*, **2001**, 234-366
10. Narasimhan K. S. et al. *Advanced Performance Materials*, Kluwer Academic Publishers, Netherlands, **1996**, 3, 7-27.
11. Swihart M. A., Inductor Cores – Material and Shape Choices
12. Bashar I et al. *Int J Mol Sci*. **2013**, 11, 21266–21305.
13. Carl S et al. Magnetoresistive detection of flowing and immobilized assay labels.
14. Chen F. Y Quality Electronic Design (ASQED), 2010 2nd Asia Symposium, **2010**, 230-234.
15. Li S et al. *J. Appl. Phys*. **1999**, 85, 5178.
16. Ji G et al. *Chem. Phys. Lett.*, **2003**, 379 -484.
17. Pham-Huu C et al. *Phys. Chem*. **2003**, 5, 3716.
18. Michele K et al. *International Journal of Pharmaceutics*, **2015**, 493, 313–327.
19. Nahla S Barakat, *Nanomedicine*. **2009**, 4, 799-812.
20. Safarikova M, et al. *Monatshefte für Chemie*, **2002**, 133, 737–759.
21. Koneracka M, et al. *J. Magn. Magn. Mater.* **1999**, 201, 427–430.
22. Koneracka M, et al. *J. Mol. Catal. B*. **2002**, 18, 13–18.
23. Senyei A et al. *J. Appl. Phys*. **1978**, 49, 3578–3583.
24. Mosbach K, et al. *FEBS Lett*. **1979**, 102, 112–116.

25. Tartaj P, et al. *J Phys D: Appl Phys*, **2003**, 36, 182–197.
26. O’Handley R.C, et al. *Wiley*: New York, **2000**.
27. Koch C.C, ed. *Nanostructured Materials*, *Noyes Publications*: New York, **2002**.
28. Yigit M. V. et al. *Pharm Res*. 2012, 29.
29. Tempany C.M. et al. *Cancer*. **2015**, 121, 817-827.
30. Sasikala A. R. K. et al. *Nanoscale*, **2015**, 7, 18119-18128
31. Latorre A et al. *European Journal of Medicinal Chemistry*, 2014, 82, 355-362
32. Pankhurst, Q.A et al. *J. Phys. D*, **2003**, 36, 167–181.
33. Fortin, J.P. et al. *Eur. Biophys*. **2008**, 37, 223–228.
34. Wust, P. et al. *Int. J. Hyperth*. **2006**, 22, 673–685
35. Maier-Hauff, K. et al. *J. Neurooncol*. **2007**, 81, 53–60.
36. Johannsen, M. et al. *Int. J. Hyperth*. **2005**, 21, 637–647.
37. Johannsen, M. et al. *Eur. Urol*. **2007**, 52, 1653–1662.
38. Basel, M.T. et al. *Int. J. Nanomed*. 7, 297–306
39. Huang et al. *Int. J. Nanomed*. 8, 2521–2532.
40. Tsiapa, I. et al. *J. Colloid Interface Sci*. 433, 163–175.
41. June, W. L. et al. *J Phys D: ApplPhys.*, **2011**, 44, 303001.
42. Liu, K. et al. *Phys. Rev. B*, **2001**, 63, 060403.
43. Gubin S.P., et al, *Russ. Chem. Rev*. **2005**, 74, 489–520.
44. Alberto P, et al, *Principles of Nanomagnetism*. Springer; Berlin/Heidelberg, Germany, **2009**.
45. Zhang, L. Y., et al. *J. Magn. Magn. Mater*. **2007**, 311, 228.
46. Carroll, K. J., et al. *J. Appl. Phys*. **2010**, 107, 09B304.
47. Pankhurst Q. A., et al. *J. Phys. D: Appl. Phys.*, **2003**, 36, 167–181.
48. Vladimir Sepelak, et al. *J. Phys. Chem. C*, **2007**, 13, 5026.
49. Cullity, B. D., et al. *Introduction to Magnetic Materials*; Wiley, **2011**.
50. Batlle, X. et al. *J. Phys. D*, **2002**, 35, 15–42.
51. Fertman V. E., et al. *Magnetic fluids guidebook: properties and applications*; Hemisphere Pub. Corp., **1990**.
52. Lu, A. H. et al. *Angew. Chem. Int. Ed*. **2007**, 46, 1222.

53. Gupta, A. K. et al. *Biomaterials*, **2005**, 26, 3995.
54. Martinez, B. et al. *Phys. Rev. Lett.* **1998**, 80, 181
55. Kodama, R. H. et al. *Phys. Rev. Lett.* **1996**, 77, 394.
56. Bødker, F. et al. *Phys. Rev. Lett.* 1994, 72, 282.
57. Kodama, R.H. et al. *J. Appl. Phys.* **1997**, 81, 5552–5558.
58. Kodama, R. et al. *Phys. Rev. B*, **1999**, 59, 6321–6336.
59. Mørup, S. et al. Spin Structures in Magnetic Nanoparticles. **2013**, 720629:1–720629:8.
60. Billas, I.M.L. et al. *J. Magn. Magn. Mater.* **1997**, 168, 64–84
61. Billas, I.M.L. et al. *J. Magn. Magn. Mater.* **1997**, 168, 64–84.
62. Jeyadevan B, et al. *J. Ceram. Soc. Jpn.*, **2010**, 118, 391
63. Carrey J, et al. *J. Appl. Phys.* **2011**, 109, 083921.
64. Mehdaoui B, et al. *Adv. Funct. Mater.*, **2011**, 21, 4573.
65. Mehdaoui B, et al. *Phys. Rev.*, **2013**, 87, 174419.
66. Rudolf H, et al. *J. Phys.: Condens. Matter*, **2008**, 20, 385214.
67. Fernandez G, et al. *Appl. Phys. Lett.*, **2013**, 103.
68. Ma, M. et al. *Nanoscale Res. Lett.* 2013, 8, 16.
69. Fernandez M.A., et al. *J. Solid State Chem.*, **2009**, 182, 2779.
70. Wu, M. et al. *Appl. Phys. Lett.* 2002, 80, 4404
71. Li N, et al. *Phys. Chem. Chem. Phys.*, **2013**, 15, 7685.
72. Wu W et al. *Nanoscale Res Lett.*, **2008**, 3, 397–415.
73. Sperling R. A., et al. *Trans. R. Soc. A*, **2010**, 368.
74. Yokoyama M, et al, *Journal of Japanese Cancer*, **1998**, 23, 2040.
75. Viveka K, et al. *MRS Advances*, 2016, 1, 247-254.
76. Viveka K, et al. *Nano-Micro Letters*, 2016, 8, 80-93.
77. Berg V, et al. *Eur. J. Cancer Clin. Oncol.*, **1982**, 18, 457-462.
78. Calderwood S.K., et al. *Adv. Radiact. Biol.* **1983**, 135-190.
79. Johnson J.H., et al. *Biochemistry*, **1980**, 19, 3836-3840.
80. Johnson J.H., et al. *Biochemistry*, **1982**, 21, 2984-2989.
81. Ganong F. W. Et al. *Review of medical physiology* (21 ed.) **2003**, New York: Lange Medical Books/McGraw-Hill, 518.

82. Green P, et al. *JACC Cardiovascular Interventions*, **2012**, 5, 974–981.
83. Caravan P, et al. *Chemical Society reviews*, **2006**, 35, 512-23.
84. Caravan P, et al. *Chemical reviews*, **1999**, 99, 2293-352.
85. Merbach A.S., et al. *Hoboken: Wiley*, **2013**, 514.
86. Bushberg J.T. et al. *The essential physics of medical imaging*. 3rd ed. Philadelphia: *Wolters Kluwer Health/Lippincott Williams & Wilkins*, **2012**.
87. Lentschig M.G., et al. *Radiology*, **2008**, 353-357.
88. Na H.B., et al. *J Mater Chem.*, **2009**, 19, 6267-6273.
89. Shao Y, et al. *Biomaterials*, **2012**, 33, 6438-6446.
90. Xiaoxia W et al. *Bioconjugate Chem.* **2004**, 15, 1408–1415.
91. Bridot J.L., et al. *J Am Chem Soc.*, **2007**, 129, 5076-5084.
92. Petoral R.M., et al. *J Phys Chem C*, **2009**, 113, 6913-6920.
93. Krebs H.U., et al. *Springer Berlin Heidelberg*, **2003**, 43.
94. Johnson M. D., et al. *Phys. Rev. Lett.* **1994**, 72, 116.
95. Wang, Y. et al. *ACS Nano*, **2011**, 5, 9927.
96. Eastoe, J. et al. *Adv. Colloid Interfac.*, **2006**, 128–130, 5.
97. Sun, et al. *J. of Thermal Analysis and Calorimetry*, 2013, 113, 1169-1176.
98. Hyeon, et al. *J. Am. Chem. Soc.*, **2001**, 123, 12798.
99. Miyawaki J, et al. *J Phys Chem B*, **2006**, 110, 5179-5181.
100. Kim D, et al. *J Am Chem. Soc.*, **2008**, 131, 454-455.
101. Wang F, et al. *Nature*, **2010**, 463, 1061-1065.
102. Das G.K., et al. *Langmuir*, **2010**, 26, 8959-8965
103. Xu C. J., et al. *Polym. Int.* **2007**, 56, 821
104. Samanta B, et al. *J Mater Chem.*, **2008**, 18, 1204–1208.
105. Lee J. H. et al. *Nature Nanotechnology*, **2011**, 6, 418–422.
106. Dennis C. L., et al. *Nanotechnology*, **2009**, 20, 395103.
107. Verde E.L., et al. *AIP Advances*, **2012**, 2, 032120–032142.
108. Carrey J, et al. *J. Appl. Phys.*, **2011**, 109, 083921–083937
109. Luis C, et al, *Scientific Reports*, **2013**, 3, 1-8.
110. Boubeta C.M., et al. **2013**, 3, 1-10.
111. Baaziz W, et al. *B.P. J. Phys. Chem. C*, **2014**, 118, 3795–3810.

112. Williams D. B., et al. Transmission Electron Microscopy: A Textbook for Materials Science; *Springer*, **2009**.
113. Yong Ding, Fundamental Theory of Transmission Electronic Microscopy.
114. Elton L. R. B., et al. *Am. J. Phys.*, **1966**, 34, 1036.
- 115 Connolly, J. Introduction to X-ray Powder Diffraction, **2007**.
116. Sadiku M. N. O. Elements of Electromagnetics; *Oxford University Press*, Incorporated, **2010**.
117. Ruediger H, et al. Improving a Vibrating Sample Magnetometer, Stetson University, Senior Research Project, **1993**.
118. Ryhänen T, et al. *J. Low. Temp. Phys.*, **1989**, 76, 287.
119. Bland J, et al. *Thesis M. Phys (Hons)*, Dept. Physics, University of Liverpool.
120. *Thermo Nicolet corporation* , Introduction to Fourier Transform Infrared Spectrometry
121. Raymond P. W. S., Analytical Spectroscopy.
122. Berne B. J., et al. Dynamic Light Scattering: With Applications to Chemistry, Biology, and Physics; *Dover Publications*, **2000**.
123. Jorg Langowski, Biophysics of macromolecules.
124. William Reusch, *Visible and Ultraviolet Spectroscopy*, **2013**.
125. Miramar College, UV Visible Absorption Spectroscopy.
126. Pawley J.B., *Handbook of Biological Confocal Microscopy* (3rd ed.). Berlin: Springer, **2006**.
127. Fellers T.J. et al. *Olympus Fluoview Resource Center*. National High Magnetic Field Laboratory. Retrieved, **2007**, 07-25.
128. Fulwyler M.J. *Science*, **1965**, **150**, 910–911.
129. Anis L, Flow Cytometry Platform.
130. Maity D, et al. *Nanomedicine*, **2010**, 5, 1571.
131. Hergt R, et al. *J. Magn. Magn. Mater.*, **2007**, 311, 187.
132. Hollingworth W, et al. *ClinRadiol*. **55**, 825–31.
133. Perry S, Nuclear Magnetic Resonance, Sprawls Education Foundation .
134. Silva A. C., et al. *Int. J. Nanomed.*, **2011**, 6, 591.

135. Rosensweig, R. E., *J. Magn. Magn. Mater.*, **2002**, 252, 370
136. Park J.W., et al. *Clin. Cancer Res*, **2002**, 8, 1172–1181.
137. Herranz F, et al. *Contrast Media Mol.Imaging*, **2008**, 3,215–222.
138. Herranz F, et al. *Contrast Media Mol.Imaging*, **2012**, 7, 435–439.
139. Salinas B, et al. *Bioinspired Biomim. Nanobiomater.*, **2012**, 1, 166–172.
140. Dennis C.L.,et al. *Nanotechnology*, **2009**, 20, 395103.
141. Verde E.L., et al. *AIPAdvances*, **2012**, 2, 032120–032142.
142. Guardia P, et al. *ACS Nano*, 2012, 6, 3080–3091.
143. Patra S, et al. *ACS Appl. Mater. Interfaces*, **2015**, 7, 9235–9246.
144. Lartigue L, et al. *J. Am. Chem. Soc.*, **2011**, 133, 10459–10472.
145. Seemann K.M. ,et al. *Biomedical Optics Express*, **2014**, 5, 2446-2457.
146. Seemann K.M., et al. *Journal of Controlled Release*, **2015**, 197, 131-137.
147. Liu Y, et al. *Bioconjug.Chem.*, **2012**, 23,671–682.
148. Deng Y.H., et al. *Colloids Surf.Physico chem. Eng. Asp.*, **2005**, 262, 87–93.
149. Hankins J, *Journal of Infusion Nursing*, **2009**, 29, 260-265.
150. Hirayama K, et al. *Biochemical and Biophysical Research Communications*, **1990**, 173 , 639–46.
151. Green P, et al. *JACC Cardiovascular Interventions*, **2012**, 5, 974–981.
152. Ge S, et al. *Journal of Biomaterials Science. Polymer Edition* 9, **1998**, 2, 131–150.
153. Keshavarz M, et al. *Journal of Physical and Theoretical Chemistry*, **2011**, 8, 85-95.
154. Samanta B, et al. *J Mater Chem.*, **2008**, 18, 1204–1208.
155. Csach K, et al. *Acta Physica Polonica A*, **2012**, 121, 1293-1295.
156. Baaziz W, et al. *J. Phys. Chem. C*, **2014**, 118, 3795–3810.
157. Guardia P, et al. *J. Phys. Chem. C*, **2010**, 115, 390.
158. Hufschmid R, et al. *Nanoscale*, **2015**, 7, 11142-11154.
159. Priya C.L., et al. *Journal of Agricultural Technology*, **2012**, 8, 143-156.
160. Mitra A, et al. *J. Phys. Chem. C*, **2014**, 118, 19356–19362.
161. Šliužienė K, et al. *Journal of Physics*, 2008, 100.
162. Tun S.H., et al. *Nano Res.* **2015**.

163. Khoshnevisan K, et al., **2011**, 42, 644-648.
164. Kouassi G.K., et al. *Anal. Chem.*, 2006, 78, 3234-3241.
165. Blanco A, et al. *Nanoscale*, **2015**, 7, 1768-1775.
166. Richard C. W., et al. *Int. J. Mol. Sci.*, **2013**, 14, 15977-16009.
167. Larumbe S, et al. *J. Nanosci. Nanotech.*, **2012**, 12, 2652–2660.
168. Park B. J., et al. *J NanosciNanotechnol.*, **2015**, 10, 7900-7906.
169. Sun J.F., et al. *Int.J.Mol. Sci.*, **2013**, 14, 5775-5783.
170. Etheridge M.L., et al. *Technology (SingapWorldSci)*, 2014, 2, 214–228.
171. Carlos M-B., et al. *Scientific Reports*, **2013**, 3.
172. Dennis C.L., et al. *Nanotechnology*, **2009**, 20, 395103.
173. Verde E.L., et al. *AIP Advances*, **2012**, 2, 032120–032142.
174. Cervadoro A, et al. **2013**
175. Nikiforov V, et al. *Russian Physics Journal*, **2007**, 50, 913-924.
176. Fuss, F.K., et al. *Proc. First Intl. Bioengg. Conf.*, (eds.) **2004**, 69.
177. Brink W. M., et al. *J Cardio vasc.MagnReson.*, **2015**, 17, 822015.
178. Davis P.L., et al. *IEEE Trans Biomed Eng.*, **1993**, 40, 1324–1327.
179. Keltner J.R., et al. *J. Magn.Reson. Med.*, **1991**, 22, 467–480.
180. Reis A, et al. *Klinische Wochenschrift* **1953**, 1, 39–42.
- 181Yokoyama M, et al. *Journal of Japanese Cancer*, **1998**, 23, 2040.
182. Viveka K, et al. *MRS Advances*, **2016**, 1, 247-254.
183. Viveka K, et al. *Nano-Micro Letters*, **2016**, 8, 80-93.
- 184 . Johnson J.H., et al. *Biochemistry*, **1980**, 19, 3836-3840.
185. Johnson J.H., et al. *Biochemistry*, **1982**, 21, 2984-2989.
186. Ganong, F. W. , *Review of medical physiology* (21 ed.), **2003**, New York: Lange Medical Books/McGraw-Hill, 518.
187. Green P, et al. *JACC Cardiovascular Interventions* **2012**, 5, 974–981.
188. Gu W.Y., et al. *Spine*, **2002**, 27, 2390 – 2395.
189. Pluen P.A., et al. *Biophysical Journal*, **1999**, 77, 542-552.
190. Yang Y, et al. *Adv. Func. Mat.*, **2015**, 25, 812-820.
191. Hankins J, *Journal of Infusion Nursing*, **2009**, 29, 260-265.
192. Hirayama K, et al. *Biochemical and Biophysical Research Communications*

- 1990**, 173, 639–46.
193. Alberghina D, et al. *J Vet Diagn Invest.*, **2011**, 23, 111-114.
 194. Bionumbers <http://bionumbers.hms.harvard.edu/KeyNumbers.aspx>.
 195. Haurowitz F, *Academic Press Inc.* First Ed., **1950**.
 196. Valentina H, et al. *Int J Environ Res Public Health*, 2009, 6, 1778–1798.
 197. Sophie L, et al. *Advances in Colloid and Interface Science*, 2011, 166, 8–23.
 198. Boubeta C. M., et al. **2013**, 3, 1-10.
 199. Sophie L, et al. *Advances in Colloid and Interface Science*, **2011**, 166, 8–23.
 200. Yang M, et al. *Biomaterials*, **2013**, 34, 2796-2806.
 201. Sun Y, et al. *Biomaterials*, **2013**, 34, 2289-2295.
 202. Hu F, et al. *Nanoscale*, **2012**, 4, 6235-6243.
 203. Zabow G, et al. *Nature*, **2008**, 453, 1058-1063.
 204. Na H.B., et al. *Adv Mater.*, **2009**, 2133-2148.
 205. Na H.B., et al. *J Mater Chem.* **2009**, 19, 6267-6273.
 206. Lentschig M.G., et al. *Radiology*, **1998**, 208, 353-357.
 207. Caillé J.M, et al. *Am J Neuroradio.*, 1983, 4, 1041-1042.
 208. Penfield J.G., et al. *Nat Clin Pract Neph*, **2007**, 3, 654-668.
 209. Bousquet J.C., et al. *Radiology*, **1988**, 166, 693-698.
 210. Chen F, et al. *AdvFunct Mater*, **2011**, 21, 4285-4294.
 211. Hifumi H, et al. *J Am ChemSoc*, **2006**, 128, 15090-15091.
 212. Yang D, et al. *RSC Adv.*, **2013**, 3, 9681-9686.
 213. Johnson N.J.J., et al. *Nanoscale*, **2010**, 2, 771-777.
 214. Rosi, N. L., et al. *Chem. ReV.*, **2005**, 105, 1547–1562.
 215. Sonvico F, et al. *Bioconjugate Chem.*, **2005**, 16, 1181–1188.
 216. Faucher L, et al. *ACS Appl Mater Interfaces*, **2012**, 4, 4506-4515.
 217. Jennifer A. N., et al. *J. Am. Chem. Soc.*, **2002**, 124, 2979–2983.
 218. Rudin M, et al. *Nat. ReV.* **2003**, 2, 123–131.
 219. Bulte J. W. M., et al. *Proc. Natl. Acad. Sci. U.S.A.* **1996**, 15256–15261.
 220. Josephson L, et al. *Bioconjugate Chem.* , **2010**, 186–191.
 221. Bulte, J. W. M., et al. *NMR Biomed.* , 17, 484–499.
 222. Kim Y. B., et al. *Magn. Reson. Imaging*, 27, 601–610.

- 223. Zhuo J, et al. *Radio Graphics* 26, 275–297.
- 224. Lee H, et al. *Science*, **2007**, 318, 426–430.
- 225. Liu X, et al. *ACS Nano*, **2013**, 7, 9384– 9395.
- 226. . Lee H, et al. *Adv. Mater.*, **2009**, 21, 431–434.
- 227. Liu Y, et al. *Adv. Mater.*, **2013**, 25, 1353–1359.
- 228. Choi D, et al. *Small*, **5**, 571–573.

